IRON NITRIDE BASED MAGNETORESISTANCE DEVICES FOR SPINTRONIC APPLICATIONS

A DISSERTATION
SUBMITTED TO THE FACULTY OF
UNIVERSITY OF MINNESOTA
BY

Xuan Li

IN PARTIAL FULFILLMENT OF THE REQUIREMENTS
FOR THE DEGREE OF
DOCTOR OF PHILOSOPHY

PROFESSOR JIAN-PING WANG, ADVISOR

MARCH 2018

© XUAN LI 2018

Acknowledgements

First of all, I would like to express my gratitude to my Ph.D adviser Professor Jian-Ping Wang for his continuous support, guidance, and patience during my graduate study. I appreciate the opportunities that he granted me to work on the exciting projects. I have substantially benefited from his knowledge, experience, and scientific vision over the years.

I am thankful to my thesis committee members Prof. Stephen Campbell, Prof. Bethanie Stadler, and Prof. Xiaojia Wang for their valuable discussions, time, and efforts of serving in my committee.

I would also like to acknowledge the support and advice from Prof. Randall Victora and Prof. Jack Judy during my study and stay in the Center for Micromagnetic and Information Technologies (MINT). The excellent courses and academic activities that they organized help me build a solid foundation in the fields of magnetics and spintronics.

Many of my collaborators provided enormous help to my research. Special acknowledgement to Dr. Michael Osofsky (Naval Research Laboratory), Prof. Oleg Myrasov (University of Alabama), Prof. Paul Voyles (University of Wisconsin). I would also like to thank all staff members at the UMN Nanofabrication Center (NFC).

It has been an enjoyable experience with all the researchers and students who worked with me in Prof. Wang's group. Special thanks to Dr. Yiming Wu and Dr. Meiyin Yang for setting up the sputtering system with me for our researches. Thanks to Dr. Yanfeng Jiang, Prof. Bin Ma, Dr. Junyang Chen, Dr. Mahdi Jamali, Hongshi Li, Haibao Zhao,

Yisong Zhang, Hao Wang, Hui Zhao, Shihai He, Yuanpeng Li, Nian Ji, Ying Jing, Liang Tu, Andrew Lyle, Shaoqian Yin, Jonathan Harms, Todd Klein, Yi Wang, Xiaohui Chao, Xiaowei Zhang, Yinglong Feng, Angeline Klemm, Yang Lv, Jinming Liu, Zhengyang Zhao, Patrick Quarterman, Mahendra DC for their friendship and help.

Dedication

I dedicate this thesis to my wife and our parents for their unconditional love and support.

Abstract

The iron nitrides have been attracting a wide interest in spintronics researches due to their unique magnetic properties. In this thesis, I describe the experimental studies of the spintronic devices based on two important iron nitride materials, i.e. $Fe_{16}N_2$ and Fe_4N.

In the $Fe_{16}N_2$ based magnetoresistance device development, a heavy-metal free, low damping, and non-interface perpendicular current-perpendicular-to-plane (CPP) giant magnetoresistance (GMR) device with $Fe_{16}N_2$ magnetic layers has been demonstrated. The crystalline based perpendicular anisotropy of the $Fe_{16}N_2$ in the CPP GMR device is measured to be about 1.9×10^7 erg/cm^3, which is sufficient to maintain the thermal stability of the sub-10nm devices. The damping constant of the $Fe_{16}N_2$ thin film is determined to be 0.01 by a ferromagnetic resonance measurement, which is much lower than most existing materials with crystalline perpendicular magnetic anisotropy. The non-interface perpendicular anisotropy and low damping properties of make $Fe_{16}N_2$ a promising material for future spintronic applications.

In the Fe_4N material and device studies, both the (111) oriented and (001) oriented Fe_4N thin films are prepared by optimizing the buffer layers, substrate temperatures and N:Fe composition. The most attractive properties of Fe_4N in spintronics are the large spin asymmetric conductance and the negative spin polarization. The spin polarization of the (111) oriented Fe_4N is investigated. The thickness dependence of the spin polarization of the (111) oriented Fe_4N is also explored. Moreover, I have studied the Gilbert damping constant of the Fe_4N (001) thin film by ferromagnetic resonance. The α_{Fe4N} is determined

to be 0.021±0.02. Last but not least, the current-perpendicular-to-plane (CPP) giant magnetoresistance (GMR) device with Fe_4N/Ag/Fe sandwich have also been fabricated and characterized. Giant inverse magnetoresistance is observed in the Fe_4N based CPP GMR device, which confirms that the spin polarization of Fe_4N and Fe_4N/Ag interface is negative.

Table of Contents

Acknowledgements i

Dedication iii

Abstract iv

List of Tables ix

List of Figures x

Chapter 1 Introduction 1

1.1 Crystal structure and magnetic properties of $Fe_{16}N_2$ and Fe_4N 1

1.2 Current-perpendicular-to-plane (CPP) giant magnetoresistance (GMR) devices ... 7

1.3 Spin transfer torque (STT) effect and Spin transfer torque random access memory (STT-RAM) 14

1.4 Magnetoresistance device with perpendicular magnetic anisotropy for STT-RAM application 18

1.5 Inverse magnetoresistance device 21

1.6 Overview of my thesis 22

Chapter 2 Fe-N based CPP GMR stacks deposition and nanopillar devices fabrication. 25

2.1 Conventional magnetron sputtering and Facing-target-sputtering 25

2.2 Fe-N CPP GMR stack development 30

2.3 Sub-100nm CPP GMR devices fabrication 32

2.4 CPP GMR measurement 37

2.5 Spin polarization measurement by point contact Andreev refection method 39

Chapter 3 Heavy-metal free, low damping, and non-interface perpendicular CPP GMR devices based on $Fe_{16}N_2$ magnetic layers 41

3.1 Limits of state-of-the-art perpendicular magnetic anisotropy material systems 41

3.2 $Fe_{16}N_2$: a low damping and crystalline based perpendicular material system 44

3.3 Magnetoresistance of $Fe_{16}N_2$ based perpendicular CPP GMR devices 52

3.4 The scaling limit of $Fe_{16}N_2$ perpendicular material system 56

3.5 Improving the magnetoresistance signal 60

3.6 Damping constant of $Fe_{16}N_2$ 62

3.7 The limitations of $Fe_{16}N_2$ perpendicular material system 66

3.8 Summary 67

Chapter 4 Deposition and spin polarization study of Fe_4N thin films with (111) orientation 69

4.1 Introduction 69

4.2 Deposition of polycrystalline Fe_4N (111) thin films 70

4.3 Spin polarization measurement of Fe_4N (111) 75

4.4 Summary 80

Chapter 5 Fe_4N based CPP GMR devices with giant inverse magnetoresistance 82

5.1 Introduction 82

5.2 Fe_4N (001) thin films deposited on Ag under layers 84

5.3 Damping constant measurement of Fe_4N (001) thin films 89

5.4 Giant inverse magnetoresistance in Fe_4N/Ag/Fe 90

5.5 Summary 93

Chapter 6 Conclusions and Outlook 95

Appendix A: Perpendicular multi-bit magnetic tunnel junctions 97

1. Developing $[Co/Pd]_n$ multilayer for perpendicular multi-bit MTJs 97

2. Developing MgO/CoFeB/Ta/CoFeB/MgO composite layers for multi-bit MTJs 99

3. Multi-bit Perpendicular MTJ stacks 101

4. Multi-bit Perpendicular MTJs fabrication and TMR testing 103

Appendix B: Sub-100nm CPP GMR fabrication Run Sheet 105

Bibliography 110

Publication List 121

List of Tables

Table 1.1 Properties of materials with perpendicular magnetic anisotropy..................... 20

List of Figures

Figure 1.1 The Fe-N phase diagram 2

Figure 1.2 The crystal structure of $Fe_{16}N_2$ unit cell 3

Figure 1.3 The crystal structure of Fe_4N unit cell... 5

Figure 1.4 Schematic drawing of partial density of state of γ'-Fe_4N by first principles calculation. 5

Figure 1.5 Schematic drawing of Mott two current model for (a) parallel magnetic layers and (b) anti-parallel magnetic layers.. 9

Figure 1.6 Schematic of Valet and Fert's two current channel model for CPP-GMR FM/NM/FM sandwich 11

Figure 1.7 Schematic drawing of the spin dependent tunneling in MTJ with the magnetic layers in (a) parallel and (b) anti-parallel states. 13

Figure 1.8 Illustration of the in-plane spin transfer torque with the electrons transport (a) from pinned layer to free layer (b) from free layer to pinned layer. 15

Figure 1.9 Schematic drawing and TEM image of 1-transistor 1-MTJ STT-RAM 17

Figure 1.10 Electronic circuit of a NOR gate with inverse and normal MTJs 22

Figure 2.1 Schematic drawing of conventional magnetron sputtering. 25

Figure 2.2 Schematic drawing of facing-target-sputtering 27

Figure 2.3 Multi sources facing-target-sputtering system 28

Figure 2.4 Top-down view of the multi sources facing-target-sputtering system 28

Figure 2.5 Cathode of home built multi sources facing-target-sputtering system........... 29

Figure 2.6 AFM image of MgO substrate / Fe 5nm / Ag 50nm (left); X-ray diffraction pattern of MgO substrate / Fe 5nm / Ag 50nm (right)... 31

Figure 2.7 Fe-N CPP GMR stack 31

Figure 2.8 Nanometer scale CPP GMR device fabrication flow 35

Figure 2.9 SEM images of bottom electrode (left) and Nano pillar (right) 36

Figure 2.10 Microscope images of finished CPP GMR devices (a) and (b).................... 36

Figure 2.11 CPP GMR device measured by 4-point probe (left); GSG probe (right)..... 37

Figure 2.12 CPP GMR measurement setup 38

Figure 2.13 Quantum Design PPMS.. 38

Figure 2.14 Schematic drawing of Andreev refection at metal/superconductor interface 39

Figure 2.15 Schematic drawing of PCAR measurement circuit...................................... 40

Figure 3.1 Resistance vs. device diameter for MTJs and CPP GMRs............................ 43

Figure 3.2 A sketch of ordered bct phase $Fe_{16}N_2$ lattices 46

Figure 3.3 Schematic of the Fe-N based CPP GMR device. 46

Figure 3.4 The out-of-plane X-ray diffraction patterns of as-deposited and annealed samples with the same layer structure [MgO/Fe(5)/Ag(33)/Fe-N(36)/Ru(6) (thickness in nanometers)]. 47

Figure 3.5 The in-plane hysteresis loops of the as-deposited and annealed Fe-N samples. 48

Figure 3.6 (a) High-resolution scanning transmission electron microscopy (HRSTEM) image of the $Fe_{16}N_2$/Ag/$Fe_{16}N_2$ GMR sandwich with a [Fe-N 110 || Ag 100] zone axis. (b) STEM electron energy loss spectroscopy (EELS) of the Fe-N layer. 49

Figure 3.7 (a) The cross-sectional HRSTEM images of upper and lower interfaces of Fe-N/Ag/Fe-N GMR sandwich layers. The zone axis is along [Fe-N 110 || Ag 100] direction. (b) The power spectrum of the Fe-N/Ag/Fe-N HRSTEM image. The superlattice reflection from ordered $Fe_{16}N_2$ (002) crystal planes is highlighted. 50

Figure 3.8 Auger electron spectroscopy (AES) depth profile result of the Fe-N CPP GMR thin film stack. 51

Figure 3.9 The X-ray photoelectron spectroscopy (XPS) Fe $2p^{3/2}$ binding energy of the top and bottom Fe-N layers in the CPP GMR stack. The upper surface, middle and lower surface in the caption indicate the position where the XPS surveys are taken. 51

Figure 3.10 GMR signal of perpendicular Fe16N2 based CPP GMR device. (a) Giant magnetoresistance signal of a partially ordered Fe16N2 CPP GMR (post-annealed) as a function of out-of-plane magnetic field (black and blue circles) and in-plane magnetic field (red squares). The black and blue circles represent positive and negative field sweeping direction respectively. (b) Giant magnetoresistance minor loop of the partially ordered Fe16N2 CPP GMR device. 53

Figure 3.11 Giant magnetoresistance signal of a Fe-N CPP GMR (as-fabricated) as a function of out-of-plane (a) and in-plane (b) magnetic field. The black and blue circles (a) represent positive and negative field sweeping in out-of-plane direction. The red and purple circles (b) represent positive and negative field sweeping in in-plane direction... 54

Figure 3.12 Calculated crystalline anisotropy of $Fe_{16}N_2$ as a function of a,c 58

Figure 3.13 Thermal stability factor vs. device diameter with 1.0, 1.5 and 5.0 nm magnetic thin films 59

Figure 3.14 The Out-of-plane and In-plane R-H loop of CPP GMR with $Fe_{16}N_2$/Fe composite magnetic layers 61

Figure 3.15 FMR spectra of partially ordered $Fe_{16}N_2$. (a) FMR characterization setup including vector network analyzer (VNA), microwave cavity, and electromagnet where all control from computer. (b) FMR characterizations of the Fe16N2 film at the excitation frequency of 10, 12, 14, and 16 GHz. (c) The FMR magnetic fields as a function of excitation frequency overlaid with the Kittel formula curve fitting. (d) FMR linewidth measured at the excitation frequency of 15 GHz. 64

Figure 3.16 (a) Angle measurement of the FMR characterization (b) The experimental results of the angle measurement of the FMR on $F_{16}N_2$ for the excitation frequency of 14 GHz with the curve fitting data. 65

Figure 4.1 Out-of-plane X-ray diffraction patterns of 40nm Fe4N thin films deposited with (a) different N2 partial pressures; (b) different substrate temperatures. 72

Figure 4.2 Hysteresis loop of 40nm polycrystalline (111) Fe_4N thin film 74

Figure 4.3 Out-of-plane X-ray diffraction patterns of 40nm Fe_4N thin films deposited on thermally oxidized Si substrates with Ru, Pd and Pt buffer layers. 74

Figure 4.4 Out-of-plane X-ray diffraction patterns of 40nm Fe_4N thin films deposited on thermally oxidized Si substrates with Ru, Pd and Pt buffer layers. 75

Figure 4.5 Point contact Andreev reflection results: Normalized conductance as a function of applied voltage (V) divided by superconducting gap (V_Δ) (a) For (111) oriented Fe_4N and Fe (001); (b) For (111) Fe_4N with different film thicknesses. Experiment data are shown in dots, and fittings are shown in continuous curves........... 77

Figure 4.6 AFM image of Si wafer with (a) 100nm thermal oxide / Fe_4N (111) 10nm, and (b) 100nm thermal oxide / Ta 2nm / Ru 18nm / Fe_4N (111) 10nm 79

Figure 4.7 X-ray photoelectron spectroscopy spectra on (111) Fe_4N sample. (a) Fine scan on N 1s peak; (b) Fe $2p_{3/2}$ and Fe $2p_{1/2}$ peaks. 80

Figure 5.1 XRD θ-2θ scans of the 17nm Fe-N thin films deposited with different N2 partial pressures. The Fe(002) diffraction signals are from the Fe buffer layer. 85

Figure 5.2 The rocking curve measured on Fe_4N (002) peak of the sample with 0.4 mTorr N_2 partial pressure.. 87

Figure 5.3 The XPS spectrum of the Fe_4N sample with 0.4 mTorr N_2 partial pressure. 88

Figure 5.4 The resonant magnetic fields for different excitation frequencies which are overlaid with the Kittle formula curve fitting. The inset shows the FMR line width of Fe4N (001) thin film measured at 16GHz. 90

Figure 5.5 Schematic drawing of Fe_4N/Ag/Fe GMR stack 91

Figure 5.6 Giant magnetoresistance signal of (a)Fe4N/Ag/Fe CPP GMR; (b)Fe/Ag/Fe CPP GMR as a function of in-plane magnetic field 93

Figure 7.1 Perpendicular hysteresis loops of $[Co/Pd]_n$ multilayer (a) for bottom fixed layer; (b) for top free layer. 99

Figure 7.2 Hysteresis loops of MgO/CoFeB/Ta/CoFeB/MgO composite structure for middle free layer. 100

Figure 7.3 Schematics of a designed multi-bit perpendicular MTJ stack 101

Figure 7.4 M-H loops of Multi-bit MTJ stacks measured by VSM 102

Figure 7.5 TMR signal of multi-bit MTJ device with stack structure Ta 5/Pd 10/(Co 0.35/Pd 0.7)$_5$/CFB 0.8/MgO 2/CFB 1.6/Ta 0.8/CFB 1.2/MgO 2/CFB 0.8/Ta 0.5/Pd 0.5/(Co 0.4/Pd 0.7)$_4$/Co 0.4/Pd 5 104

Chapter 1 Introduction

1.1 Crystal structure and magnetic properties of $Fe_{16}N_2$ and Fe_4N

Spintronics, also known as spin electronics, is an emerging field of research aiming to utilize electron spins for information storage and logic operation purposes. It is a research area that highly relies on material developments. To improve the existing spintronic devices and to exploit the new devices for special functions, people have been trying to incorporate novel magnetic materials with desirable properties into the devices. Iron nitrides (Fe-N), for their unique magnetic behaviors, have attracted substantial attentions in spintronic applications. For example, magnetic tunnel junction (MTJ) with inverse tunneling magentoresistance (TMR), which can potentially be an important component of spin-based logic circuit, has been realized based on Fe_4N with negative spin polarization[1,2]. Another attractive property of Fe_4N is its theoretically predicted high spin polarization ratio, where nitrogen atoms plays a curial role in localizing the electron cloud of the fcc Fe lattice[3]. $Fe_{16}N_2$, on the other hand, is an intriguing material because of its controversial high saturation magnetization[4-6]. In recent years, due to the progress of material preparation and metrology methods, the high saturation magnetization of $Fe_{16}N_2$ is confirmed[7]. It is also a promising material for magnetic layers of spin-transfer-torque random access memory (STT-RAM) due to its non-interface perpendicular anisotropy, heavy-metal free characteristic and relatively large spin polarization[8,9].

Figure 1.1 shows the Fe-N phase diagram[10], where the α''-$Fe_{16}N_2$ phase and γ'-Fe_4N phase are pointed out at N atomic ratio equals 11.1% and 20% respectively. The

metastable α''-$Fe_{16}N_2$ phase was discovered by Jack in 1951. The bulk α''-$Fe_{16}N_2$ samples were prepared by rapid quenching from γ'-N-austenite. In the phase diagram, at above 590°C, the γ phase (face-center-cubic, fcc) Fe dominates. The doped N atoms randomly occupy the octahedral interstices when N atomic ratio is ~11.1%. By quenching the Fe-N from high temperature, the system undergoes a fcc to body-center-cubic (bcc) phase transformation with N atoms "frozen" at the interstitial sites. As a result, a tetragonally distorted body-centered (bct) structure, namely α'-FeN martensite (Fe_8N), is formed[11].

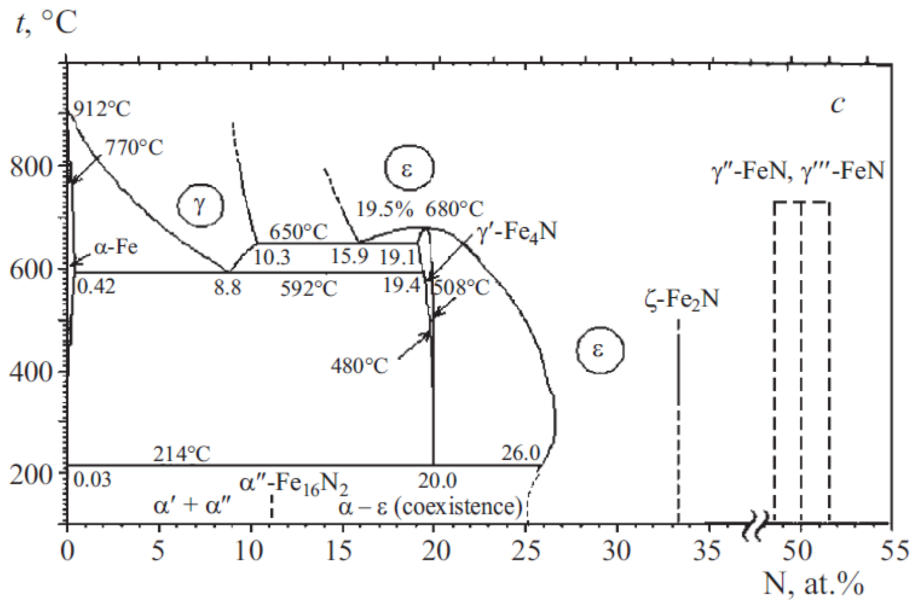

Figure 1.1 The Fe-N phase diagram[10]

In α'-FeN martensite (Fe_8N), N atoms randomly occupy the interstitial sites of a preferred lattice direction. Upon an anneal process at 150-180 ^{o}C, the N atoms become self-ordered and the Fe-N transforms from α'-Fe_8N phase to chemically ordered α''-$Fe_{16}N_2$ phase[4], as shown in Figure 1.2. It is worthwhile to mention that the metastable α''-

$Fe_{16}N_2$ phase decompose to Fe and Fe_4N at above 250 °C. An attractive property of the α"-$Fe_{16}N_2$ is the high saturation magnetization. The reported large saturation magnetization of the α"-$Fe_{16}N_2$ is around 2.6-2.9T[5,6,12-15], which is well above the Slater-Pauling curve[16-18]. Since the high saturation magnetization of $Fe_{16}N_2$ is not the main topic of this thesis, it will not be discussed in detail.

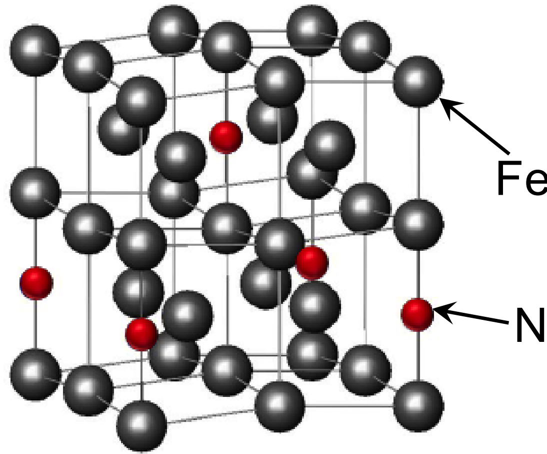

Figure 1.2 The crystal structure of $Fe_{16}N_2$ unit cell

Besides the high magnetic moment, another intriguing magnetic property of α"-$Fe_{16}N_2$ is the large anisotropy constant. When $Fe_{16}N_2$ thin film is prepared, its in-plane lattice parameter a is usually constrained by a buffer layer or a substrate with similar lattice constant. As the N atoms are introduced into the lattice, the c lattice parameter of $Fe_{16}N_2$ can be larger than a. The typical lattice parameters of α"-$Fe_{16}N_2$ are a = 5.72 Å and c = 6.28 Å. Therefore the crystal anisotropy of α"-$Fe_{16}N_2$ is built up along the out-of -plane direction. The perpendicular anisotropy of $Fe_{16}N_2$ thin film originates from the crystal asymmetry. It is significantly larger than the perpendicular material system that based on

magnetic/non-magnetic interface coupling. Back in the year 1999, H. Takahashi and Y. Sugita et al. prepared single crystal α"-$Fe_{16}N_2$ thin film on $In_{0.2}Ga_{0.8}As$ (001) substrates by molecular beam epitaxy (MBE), and the perpendicular anisotropy of the samples were measured to be $K_1 = 1.55 \times 10^7$ erg/cm^3 and $K_2 = 0.4 \times 10^7$ erg/cm^3 through magnetic torque curves[8]. S. Uchida et al. calculated the magnetic anisotropy of $Fe_{16}N_2$, and the result $K = 0.8 \times 10^7$ erg/cm^3 is on the same order of the experiment results[19].

Recently, N. Ji et al. measured the perpendicular anisotropy of Fe (22nm) / $Fe_{16}N_2$ (48nm) samples. It was found that depending on the degree of N site ordering, the perpendicular anisotropy of Fe/$Fe_{16}N_2$ composite layers can be as large as 1.0×10^7 erg/cm^3.[9] Considering there is a strong ferromagnetic coupling between the perpendicular $Fe_{16}N_2$ and the in-plane anisotropic Fe layers, the anisotropy constant of the $Fe_{16}N_2$ can be larger than the reported value. N. Ji et al. also measured the spin polarization of $Fe_{16}N_2$ by point contact Andreev reflection (PCAR) technique. The spin polarization ratio is fitted to be P = 52%, which is larger than the existing crystalline based perpendicular magnetic materials, for example $L1_0$ FePt[20].

As for γ'-Fe_4N, it has been attracting a wide interest due to the high spin polarization ratio and the negative spin scattering asymmetry at the Fermi level[3]. The γ'-Fe_4N crystal lattice cell contains fcc-Fe and a N atom located at the body center position of fcc-Fe, as shown in Figure 1.3. The lattice constant of γ'-Fe_4N is 3.795 Å. Since the out-of-plane lattice parameter c is the same as the in-plane lattice parameter a, γ'-Fe_4N has cubic anisotropy. The Curie temperature of γ'-Fe_4N is 761 K[11]. To promote the γ'-Fe_4N phase, the process or anneal temperature normally needs to be higher than ~220°C according to

the Fe-N phase diagram. The process temperature to form the γ'-Fe_4N phase is significantly lower than that of the other high spin polarization materials. For example, the process temperature of Heusler compounds is as high as 450-550 °C[21,22]. This advantage makes Fe_4N compatible with the read head processes of hard drive industry.

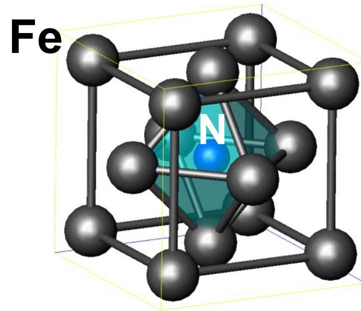

Figure 1.3 The crystal structure of Fe_4N unit cell

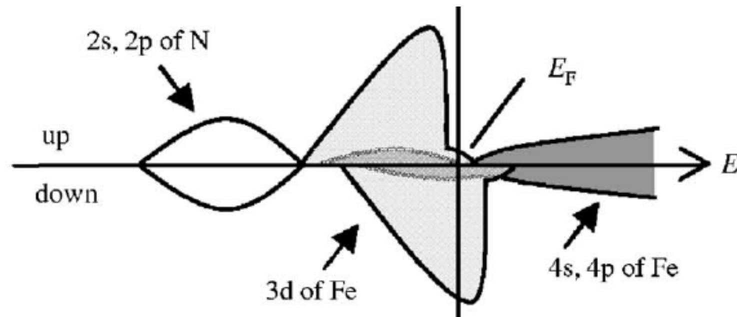

Figure 1.4 Schematic drawing of partial density of state of γ'-Fe_4N by first principles calculation[3].

Figure 1.4 shows a schematic drawing of the partial density of state of γ'-Fe_4N by first principles calculation. The 3*d* orbitals are dominant at the Fermi level, and the 4*s* and 4*p* orbitals are positioned at the energy level higher than E_F. Thus the electrical conductance of γ'-Fe_4N is mainly contributed by the 3*d* electrodes at zero temperature. It has been

theoretically predicted that Fe_4N has a large spin polarization due to the interactions between the 3d electrons of Fe and the 2s, 2p electrons of N [3]. The $P_{\mathrm{DOS}}(E_{\mathrm{F}})$ calculated by density of state at the Fermi level equals to -0.6, and the spin polarization defined by electron conductance as this formula:

$$P(E) = \frac{\sigma_{\uparrow}(E) - \sigma_{\downarrow}(E)}{\sigma_{\uparrow}(E) + \sigma_{\downarrow}(E)}$$

Eq. 1-1

is as large as about -1 at zero temperature.

The spin polarization of γ'-Fe_4N thin film sample with (001) out-of-plane orientation was measured by point contact Andreev reflection (PCAR) technique[23]. The spin polarization ratio was deduced to be approximately 0.59, which is much larger than the value of α-Fe (P = 0.49) measured by the same method. The spin polarization measured by PCAR is known to be close to the polarization ratio defined by electron conductance[24]. By this measurement, only the absolute value of spin polarization can be obtained, but the positive or negative polarity cannot be distinguished.

Spin-resolved photoelectron spectroscopy was utilized to determine the valance band structure of γ'-Fe_4N. The negative spin polarization of γ'-Fe_4N was deduced by this measurement[25]. In anisotropic magnetoresistance (AMR) measurements[26-30], γ'-Fe_4N also shows opposite sign compared to those material with positive spin polarization. These results also confirm the negative spin polarization of γ'-Fe_4N. The negative spin polarization is the characteristic that the majority spin electrons are scattered more strongly than the minority spin electrons in the material. Such a property makes γ'-Fe_4N

so unique since the main stream magnetic materials in spintronics have the positive spin polarization.

1.2 Current-perpendicular-to-plane (CPP) giant magnetoresistance (GMR) devices

Giant magnetoresistance (GMR) was discovered by Albert Fert's and Peter Grünberg's research groups in late 1980s. The effect was first observed in $[Fe(001)/Cr(001)]_n$ multilayer superlattices[31] and Fe/Cr/Fe sandwich layers[32]. In both cases, without any external magnetic field, the magnetization direction of the Fe layer is opposite to that of the adjacent Fe layer, due to the antiferromagnetic interlayer exchange coupling through the Cr spacer in between. When an external magnetic field is applied to the multilayers, the magnetization of the Fe layers are aligned to the same direction. Associated with the magnetization configuration transition from antiparallel to parallel, a large change in-plane resistance of the multilayer was observed. The GMR ratio is defined as:

$$GMR\ (\%) = \frac{R_{AP} - R_P}{R_P} \times 100\%$$

Eq. 1-2

in which R_{AP} is the resistance of antiparallel configuration and R_P is the resistance in parallel configuration. The GMR ratio reaches 45% at 4.2 K and 17% at RT for the $[Fe(001)/Cr(001)]_n$ multilayer superlattices[31], and 1.5% for the Fe/Cr/Fe sandwich structure at low temperature[32].

The giant magnetoresistance effect is closely related to spin dependence scattering[33], which points out that the majority and minority spin electrons have different resistivity

relative to the magnetization direction of the magnetic layers. Normally, when the electron spin direction aligns to the same direction as the magnetization, the electrons have smaller probability to be scattered thus result in lower resistivity, vice versa. The spin dependent scattering can happen both in the magnetic layer or at the magnetic/nonmagnetic interface.

Giant magnetoresistance can be qualitatively explained by Mott two current model[34]. In Figure 1.5, a sandwich structure with two magnetic layers separated by a non-magnetic metallic spacer layer is considered. In this model, it is assumed that electrons do not change the spin directions when they travel through a distance of several tens of nanometers, which has been experimentally demonstrated. Thus the electric current can be treated as two spin channels, namely up spin channel and down spin channel, connected in parallel. The total resistance is equivalent to two parallel connected resistors for the two spin channels.

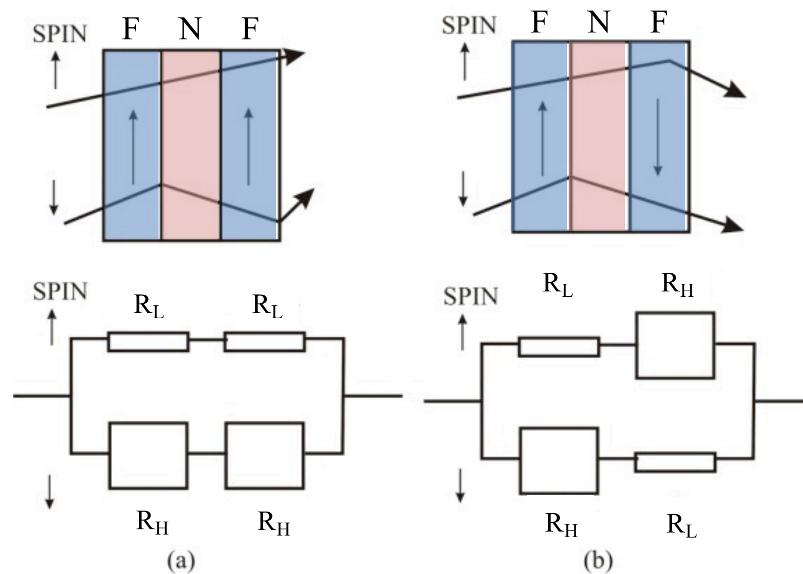

Figure 1.5 Schematic drawing of Mott two current model for (a) parallel magnetic layers and (b) anti-parallel magnetic layers.

To apply this model to a Ferromagnetic/Nonmagnetic/ Ferromagnetic sandwich structure, we define two resistances, R_L when the spin is aligned with the magnetization, and R_H when the electron's spin is opposite to the magnetization. The resistances in the parallel and anti-parallel state can be written as:

$$R_P = \frac{2\times(R_L \times R_H)}{R_L + R_H}$$

Eq. 1-3

and

$$R_{AP} = \frac{R_L + R_H}{2}$$

Eq. 1-4

thus the magnetoresistance is:

$$GMR(\%) = \frac{\Delta R}{R_p} = \frac{R_{AP} - R_P}{R_P} = \frac{(R_H - R_L)^2}{4\times(R_L \times R_H)}$$

Eq. 1-5

The Mott two current model can be used to describe both current-in-plane (CIP) GMR and current-perpendicular-to-plane (CPP) GMR. In the CPP GMR mode, the spin up and spin down electrons are forced to travel perpendicular to the magnetic layers. That is normally realized by defining sandwich layers into nanopillar structures. The detailed fabrication processes of the CPP devices will be discussed in next chapter.

In 1992, Valet and Fert developed a quantitative model to explain the current-perpendicular-to-plane (CPP) GMR effect in magnetic/non-magnetic multilayers[35]. Their

model includes the spin-dependent resistivity in both bulks and interfaces. In addition, spin diffusion and spin accumulation are taken into account in the model. The ferromagnetic layers resistivity in which electron spin and local magnetization are parallel: $\rho_F^{\uparrow}$ (or antiparallel, $\rho_F^{\downarrow}$) is written as:

$$\rho_F^{\uparrow(\downarrow)} = 2\rho_F^{*}\times(1-(+)\beta) = \frac{2\rho_F}{1+(-)\beta}$$

Eq. 1-6

where $\rho_F^{*} = \frac{\rho_F^{\uparrow}+\rho_F^{\downarrow}}{4} = \frac{\rho_F}{1-\beta^2}$

Similarly, for the ferromagnet/normal metal interface, the spin-dependent resistance is defined as:

$$r_b^{\uparrow(\downarrow)} = 2r_b^{*}\times(1-(+)\gamma) = \frac{2r_b}{1+(-)\gamma}$$

Eq. 1-7

where $r_b^{*} = \frac{r_b^{\uparrow}+r_b^{\downarrow}}{4} = \frac{r_b}{1-\gamma^2}$

In above equations, $\beta = \frac{\rho_{\downarrow}-\rho_{\uparrow}}{\rho_{\downarrow}+\rho_{\uparrow}}$ and $\gamma = \frac{r_{b\downarrow}-r_{b\uparrow}}{r_{b\downarrow}+r_{b\uparrow}}$ are the spin scattering asymmetry of the bulk layer and the interface respectively.

The schematic of the two current channel model for CPP-GMR FM/NM/FM sandwich structure is given by Figure 1.6. The resistance in parallel and antiparallel states are:

$$AR^{(AP)} = \rho_F^{*}t_F + \rho_N^{*}t_N + 2r_b^{*}$$

Eq. 1-8

$$\frac{1}{AR^{(P)}} = \frac{1}{2\rho_F^{*}(1-\beta)t_F + 2\rho_N^{*}t_N + 4r_b^{*}(1-\gamma)} + \frac{1}{2\rho_F^{*}(1+\beta)t_F + 2\rho_N^{*}t_N + 4r_b^{*}(1+\gamma)}$$

Eq. 1-9

We obtain:

$$\Delta RA \sim 2\times\frac{\beta^2}{1-\beta^2}\times\rho_F t_F + 2\times\frac{\gamma^2}{1-\gamma^2}r_b$$

Eq. 1-10

From this equation, we can conclude that larger β and γ result in higher CPP-GMR.

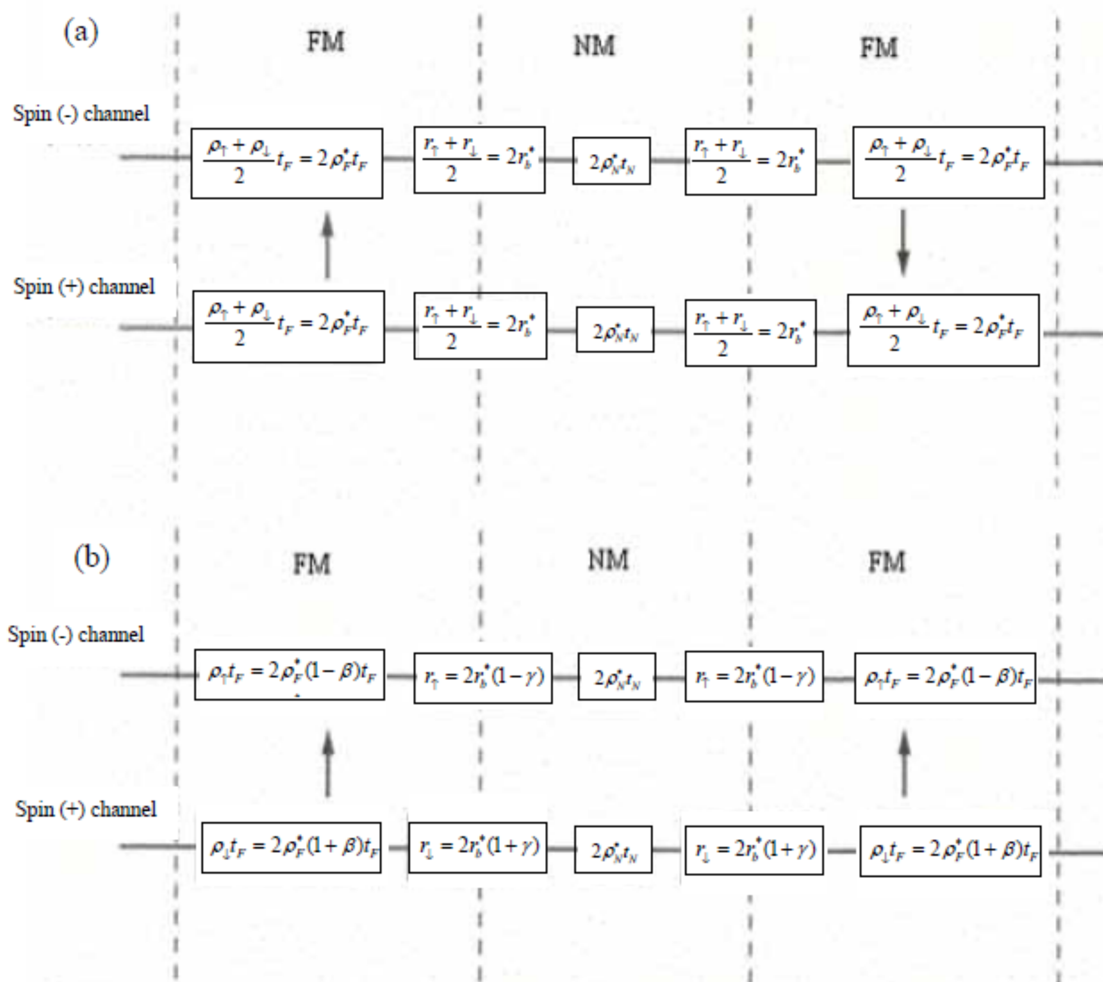

Figure 1.6 Schematic of Valet and Fert's two current channel model for CPP-GMR FM/NM/FM sandwich[35]

In order to achieve high GMR ratio, the lattice constants and electron band structures of the magnetic layer and spacer materials need to match well. Lattice mismatch may create dislocation defects at the interface thus increases the chance of spin independent scattering. The electron band matching allows the electrons of one spin polarity passing through the FM/NM interface easily, while the electrons of the other spin polarity experiences more scattering at the FM/NM interface. Therefore a large spin scattering asymmetry can be obtained. For example, Co/Cu[36] and Fe/Cr[37] FM/NM pairings are reported to have large GMR ratio at low temperature. The GMR ratio of the other materials, such as Co/Ag[38], Ni/Ag[39], and NiFe/Au[40] are not very high.

Tunneling magnetoresistance (TMR) is very similar to CPP GMR in term of their device structures. If the non-magnetic spacer layer of CPP GMR is substituted by a thin oxide layer, the device becomes magnetic tunnel junction (MTJ). The thickness of the oxide layer is typically as thin as 0.8-2.0 nanometer in MTJs. As what we observed in CPP GMR, the resistance of MTJ also depends on the relative angle between the magnetizations of its two magnetic layers. Normally the state where magnetic layers are anti-parallell aligned shows high resistance while the state where magnetic layers are parallel to each other shows low resistance, namely tunneling magnetoresistance (TMR) effect. The tunneling resistance between two ferromagnetic films was first reported by Julliere in 1975[41]. Although TMR have similar device structures as GMR, the underlying physics of TMR is quite different from CPP GMR. The TMR effect relies on spin dependent tunneling, as shown in Figure 1.7. Julliere also proposed a model to explain

spin dependent tunneling and TMR effect. In this model, the electron tunneling is assumed to be spin conservative. The TMR ratio can be written as:

$$TMR = \frac{R_{AP} - R_P}{R_P} = \frac{G_P - G_{AP}}{G_{AP}} = \frac{2 \times P_L \times P_R}{1 - P_L \times P_R} \times 100\%$$

Eq. 1-11

where

$G_p = \frac{1+P_L}{2} \times \frac{1+P_R}{2} + \frac{1-P_L}{2} \times \frac{1-P_R}{2}$, $G_p = \frac{1+P_L}{2} \times \frac{1-P_R}{2} + \frac{1-P_L}{2} \times \frac{1+P_R}{2}$

and $P = \frac{DOS_{majority} - DOS_{minority}}{DOS_{majority} + DOS_{minority}}$

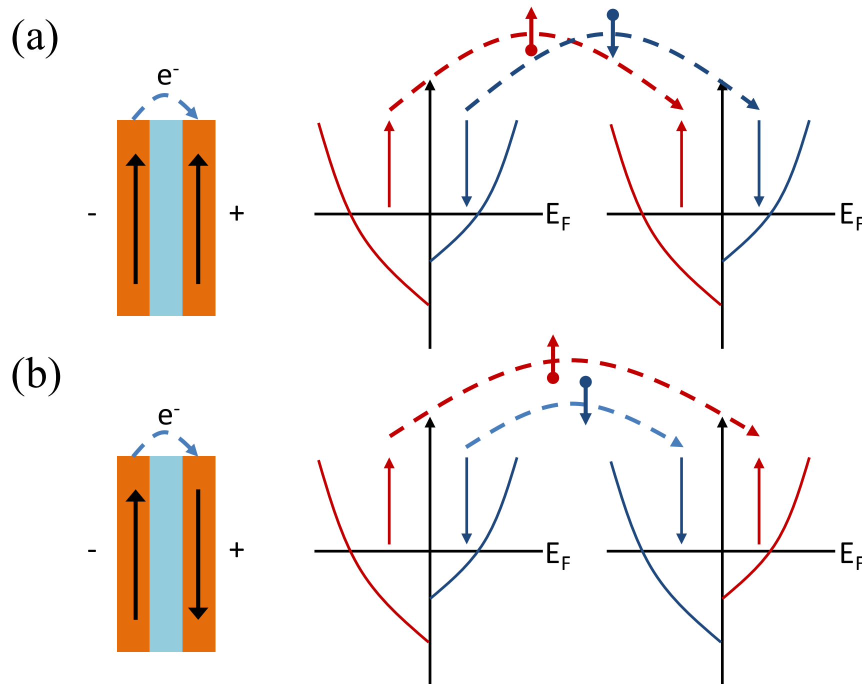

Figure 1.7 Schematic drawing of the spin dependent tunneling in MTJ with the magnetic layers in (a) parallel and (b) anti-parallel states.

The tunneling magnetoresistance did not attract much attention until the MTJ with amorphous Al-O_x barrier was reported. The Al-O_x barrier based MTJs demonstrate relatively large TMR ratio at room temperature[42,43]. The TMR ratio of the Al-O_x MTJ can be as high as 70%[44]. Another milestone in this research field is the demonstration of MTJ with MgO barrier[45,46], which shows ultra high TMR ratio due to the coherent spin dependent tunneling[47]. To date, the highest record of the TMR ratio of MgO MTJ is over 600%[48].

1.3 Spin transfer torque (STT) effect and Spin transfer torque random access memory (STT-RAM)

Spin transfer torque (STT) effect is considered to be the reverse effect of giant magnetoresistance (GMR) and tunneling magnetoresistance (TMR). The STT effect in ferromagnetic/nonmagnetic/ferromagnetic multilayer structure was first proposed and theoretically studied by Slonczewski[49] and Berger[50] in 1996. It was predicted that the magnetization of ferromagnetic free layer can be switched by spin polarized current due to the spin angular momentum transfer between the polarized electrons and the magnetization of the free layer. Later on, Slonczewski also pointed out that the magnetization of ferromagnetic free layer can be in steady procession if the STT cancels out magnetic damping[51]. The STT theory has been proved by the experiment results in Co/Cu superlattices[52] and Co/Cu/Co sandwich structure[53] in the year 1998 and 1999. It soon attracted considerable attentions in CPP GMR and MgO based MTJ devices due to its potential applications[54], such as STT-RAM[55,56] and spin torque oscillator[57]. Today,

STT effect has already become one of the most attractive topic in condensed matter physics.

Figure 1.8 describes the STT induced switching in CPP GMR or MgO based MTJ devices. We assume that the magnetization of one magnetic layer (pinned layer, M_p) is stiffer than the other (free layer, M_f) and initially there is an angle θ between the two layers. If electrons travel from the pinned layer to the free layer, they are spin polarized by the pinned layer. When the polarized electrons arrive the free layer, they tend to align with the magnetic moment of the free layer and give a torque to the free layer magnetization, until the M_f is parallel to the M_p. If electrons flow from the free layer to the pinned layer, the electrons reflected into free layer has a polarization direction opposite to the pinned layer magnetization. In this case, the STT tends to align M_f antiparallel to M_p.

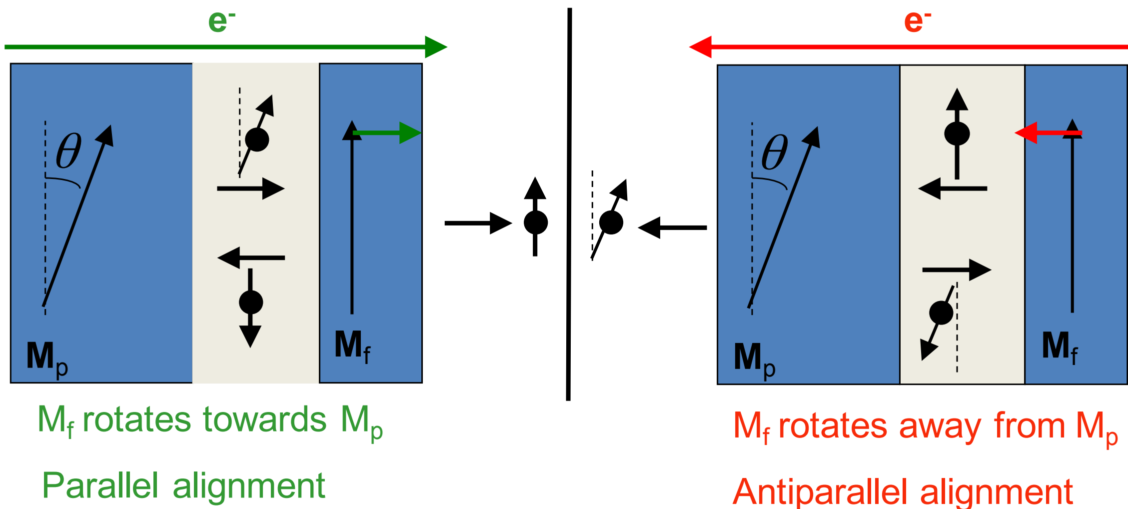

Figure 1.8 Illustration of the in-plane spin transfer torque with the electrons transport (a) from pinned layer to free layer (b) from free layer to pinned layer.

According to Slonczewski's spin-transfer-torque model, the dynamics of the free layer magnetization is governed by the following modified Landau-Lifshitz-Gilbert (LLG) equation[49,58-60]:

$$\frac{dM}{dt} = -\gamma M \times H_{eff} + \frac{\alpha}{M_s} M \times \frac{dM}{dt} + \frac{\gamma a_J}{M_s} M \times (M \times M_p) + b_J (M \times M_p)$$

Eq. 1-12

where H_{eff} is the effective magnetic field which includes the anisotropy field and demagnetizing field. M and M_p are the magnetization vectors of free layer and pinned layer respectively. γ is the gyromagnetic ratio and α is the damping constant. a_J is the in-plane spin torque factor that can be written as:

$$a_J = -\frac{h}{2e} \frac{\eta}{M_s t} J \qquad \text{Eq. 1-13}$$

in which η is a term related to the spin polarization and the efficiency of the spin current. $b_J = \xi a_J$ is the field like torque (or perpendicular torque)[59,61], which is normally a small portion of in-plane torque and can be ignored when we estimate the critical switching current in metallic multilayer[62]. By solving the LLG equation, we obtain the critical switching current density of the MR devices:

$$J_{c0} = -\frac{2eM_s t\alpha}{h\eta} H_{eff} \qquad \text{Eq. 1-14}$$

One may notice that the critical switching current density J_c is proportional to the damping constant α. Thus a low damping constant α is always preferred to achieve low power consumption in current induced magnetization switching.

The most important application of the STT effect is the spin transfer torque random access memory (STT-RAM), which is considered to be a promising candidate for the near future memory technology[63-67]. The advantages of STT-RAM include high writing speed, non-volatility, and scalability with contemporary CMOS integrated circuit. STT-RAM is the second generation magnetic random access memory (MRAM). Compared to its predecessor toggle MRAM[68], which relies on Oersted magnetic field to switch the free layer of MTJ or GMR, STT-RAM utilizes the STT induced free layer magnetization switching to fulfill the writing process. Since the STT current is much more efficient than the conventional current generated Oersted field for magnetization switching, STT-RAM has great improvement over the traditional MRAM in term of energy consumption.

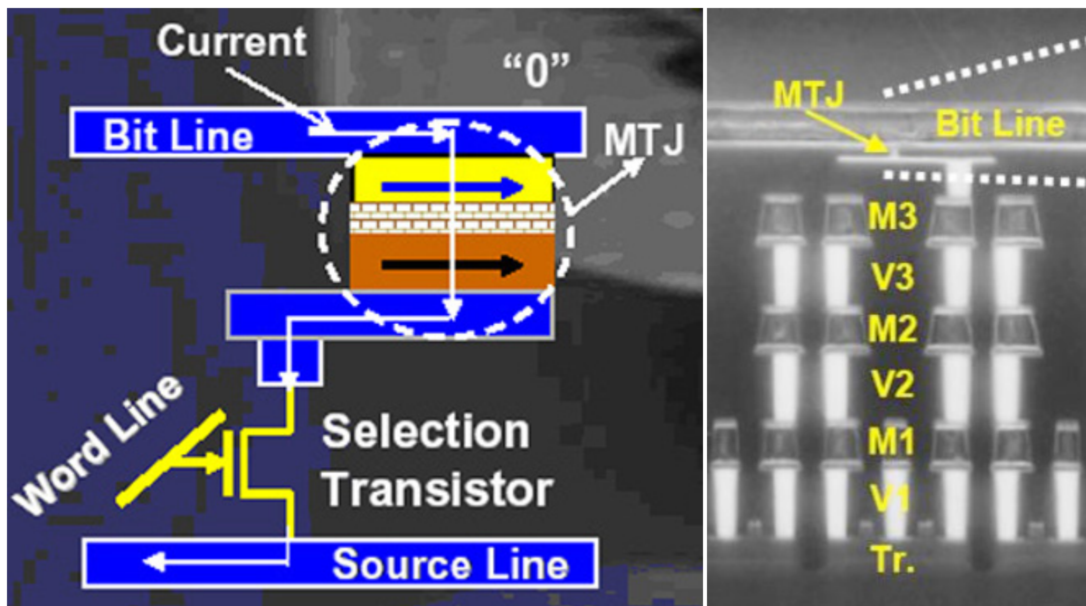

Figure 1.9 Schematic drawing and TEM image of 1-transistor 1-MTJ STT-RAM[67]

As given in the schematic drawing in Figure 1.9, a STT-RAM unit cell consists of a core of MTJ, in connection with one or more transistors, word line, bit line, and source line. The MTJ is the storage element for "0" and "1" state, and the transistor serves as the "on" and "off" switch of the writing current. Although most of the current STT-RAM device in application are based on MTJ, CPP GMR are still playing important role in STT study as it can demonstrate the capability of the novel magnetic material for the free/pinned layer.

1.4 Magnetoresistance device with perpendicular magnetic anisotropy for STT-RAM application

In recent years, magnetic materials with perpendicular magnetic anisotropy (PMA) has been attracting lots of attentions and has been utilized in STT devices to increase the areal density of STT-RAM[69-71]. In comparison with the devices utilizing in-plane magnetic materials, PMA based magnetic devices have large thermal stability in low dimensions as well as no constraint on the cell aspect ratio. Furthermore, recent studies demonstrate that perpendicularly magnetized GMR/TMR devices have lower critical current and faster switching speed than the in-plane magnetized devices[72,73]. These characteristics facilitate low power consumption in memory or logic circuit operation.

Derived from Eq1-14., the critical switching current density J_{c0} can be written for the magnetoresistance devices with in-plane $J_{c0(\mathrm{P})}$ and perpendicular $J_{c0(\perp)}$ magnetic anisotropy as:

$$J_{c0(\mathrm{P})} = -\frac{2eM_s t\alpha}{\hbar\eta}\left(H_{\mathrm{P}k} + 2\pi M_s\right) \qquad \text{Eq. 1-15}$$

$$J_{c0(\perp)} = -\frac{2eM_s t\alpha}{\hbar\eta}\left(H_{\perp k} - 4\pi M_s\right) \qquad \text{Eq. 1-16}$$

In order to switch the free layer magnetization, the STT current needs to overcome the demagnetization field ($2\pi M_s$) in addition to the anisotropic field for the in-plane magnetized STT devices. The effective field (H_{eff}) of the CoFeB based in-plane MTJ is on the order of 1×10^4 Oe. Whereas for the perpendicular STT devices, their demagnetization field can partially compensate the anisotropic field and decrease the overall H_{eff}. By properly choosing the perpendicular material, the $J_{c0(\perp)}$ can be lower than the $J_{c0(\mathrm{P})}$.

In Eq. 1-15, $H_{\mathrm{P}k}$ originates from the in-plane shape anisotropy of the STT devices, which is defined by the photo/e-beam lithography. Typically the STT devices are patterned into elliptical shape, and the anisotropic field is determined by the the aspect ratio (long axis : short axis). It is quite challenge to control the aspect ratio in less than 100nm dimensions by state of the art lithography process. The inhomogeneity of the cell aspect ratios can cause a wide distribution of the switching current. Whereas the $J_{c0(\perp)}$ of the perpendicular STT device is dominated by the material anisotropy, which is easier to control than the in-plane device shape. Therefore, the perpendicular STT devices can significantly reduce the variation of critical switching current.

Table 1.1 Properties of materials with perpendicular magnetic anisotropy

Category	Material	K (10^7erg/cm^3)	Damping constant	Spin polarization	M_s (emu/cm^3)
Bct	$Fe_{16}N_2$[9]	1.9	0.01	0.52	2000
Interface	Ta/CoFeB/MgO [74,75]	1.0	0.03	0.6	1200
$L1_0$	FePd[76]	1.8	0.013	---	1000
	FePt[76]	7.0	0.26	0.2-0.3	1140
	FePdPt[77]	1.0-4.0	0.02-0.2	---	---
Hcp	Co[76]	0.45	0.012	---	1400
Multilayer	$[Co/Ni]_n$[70]	K_1=0.15, K_2=.008	.034	---	747
	$[CoFe/Pt]_n$[69]	Early results, not presented.			

Moreover, the uniaxial anisotropy energy of in-plane STT devices (smaller than 1×10^6 Oe) is not sufficient to keep the thermal stability ($K_u V / k_B T \geq 60$) for sub-100nm devices. Whereas the uniaxial anisotropy energy of perpendicular STT devices is normally 1-2 orders higher, which is able to maintain the thermal stability for sub-10nm devices. Details of this part will be discussed in Chapter 3.

Perpendicular magnetic anisotropic STT devices have been realized by using $[CoFe/Pt]_n$[69], $[Co/Ni]_n$ multilayers[70] and $L1_0$ FePt alloy[71], as shown in Table 1.1.

However, these perpendicular materials cannot satisfy low switching current as well as high thermal stability simultaneously. The recently developed Ta/CoFeB/MgO perpendicularly magnetized structure with ultra thin magnetic layers[74] maintain the thermal stability in ~20nm scale but it is not capable for further device scaling. Therefore, a perpendicular magnetic material that enables low switching current as well larger thermal stability is a key piece for the next generation STT MTJ/GMR devices.

1.5 Inverse magnetoresistance device

Most of the GMR and TMR devices have the same magnetic electrodes on both sides of non-magnetic spacers/barriers. According to the Valet and Fert's model and the spin dependent tunneling theory, if the spin polarization of the magnetic free and pinned layers are either positive or negative, the GMR/TMR devices show positive magnetoresistance, i.e. their resistance in antiparallel state is larger than the resistance in parallel state.

In contrast, if the spin polarities of the two magnetic layers are different, the magnetoresistance device shows negative MR ratio. This behavior can qualitatively be explained by Mott's two current model. In the parallel state, the equivalent resistor model can be described by case (b) in Figure. 1.5, which corresponds to a high resistance state. While the anti-parallel state can be represented by case (a) in Figure. 1.5, which shows a low resistance than the parallel state. For example, magnetic tunnel junctions with positive spin polarized CoFeB layer and negative spin polarized Fe_4N layer magnetic

electrodes have been demonstrated. Magnetoresistance ratio of -75% is observed in the device.

The novel negative MR ratio device and the regular positive MR ratio device are complementary. By including both of them in a circuit, a integrated device with NOR logic function is demonstrated[78], shown as Figure 1.10. NOR gates are so called 'universal gates' that can build up all the other logic functions and complicated logic circuits. Therefore, the novel negative MR ratio device and its counterpart may open a door to the spin based logic circuits. Among all the materials with negative spin polarization, Fe_4N is the one that attracts most attentions for its high spin polarization ratio due to its predicted large spin polarization as mentioned in previous sections.

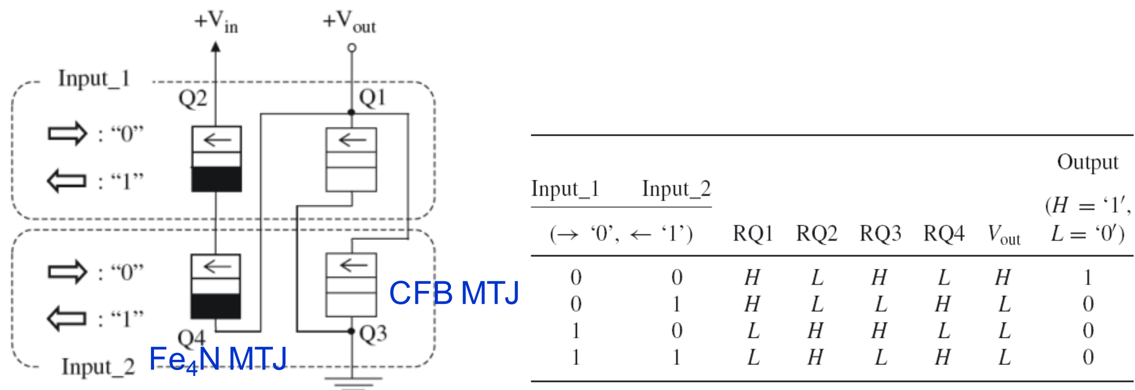

Input_1	Input_2	RQ1	RQ2	RQ3	RQ4	V_{out}	Output
(→ '0', ← '1')							(H = '1', L = '0')
0	0	H	L	H	L	H	1
0	1	H	L	L	H	L	0
1	0	L	H	H	L	L	0
1	1	L	H	L	H	L	0

Figure 1.10 Electronic circuit of a NOR gate with inverse and normal MTJs[78]

1.6 Overview of my thesis

In Chapter 1, I have covered the backgrounds of this thesis, including the magnetic material properties of $Fe_{16}N_2$ and Fe_4N. Basic concepts of CPP GMR, MTJ, STT effect, STT-RAM and inverse MR logic device are introduced in this chapter.

In Chapter 2, I will introduce the working principles of conventional sputtering and facing target sputtering for thin film deposition. A multi sources facing-target-sputtering system was built for the Fe-N CPP GMR stacks deposition. The CPP GMR stacks development, nanoscale device fabrication and device testing will also be discussed in details.

In Chapter 3, I will demonstrate the feasibility of a heavy-metal-free, low damping and non-interface perpendicular CPP GMR device based on $Fe_{16}N_2$ for future spintronic applications. The damping constant of the $Fe_{16}N_2$ is determined to be much smaller than the current crystalline perpendicular materials. The large perpendicular magnetic anisotropy of the $Fe_{16}N_2$ system is sufficient to support future spintronic devices as small as sub 10 nm.

Chapter 4 covers my work on the deposition and spin polarization study of Fe_4N thin films with (111) orientation. By optimizing the buffer layer, N:Fe composition, and substrate temperature, the (111) oriented Fe_4N thin films are deposited on thermally oxidized Si substrate. The spin polarization of the (111) Fe_4N is measured by the point contact Andreev reflection (PACR) technique. The thickness dependence of the spin polarization is also studied.

Chapter 5 includes my works on the damping constant (α) measurement of Fe_4N and the Fe_4N based giant inverse magnetoresistance device. Fe_4N (001) thin films have been prepared on Fe/Ag underlayers. The damping constant of the Fe_4N (001) is measured by the ferromagnetic resonance. The CPP GMR with Fe_4N/Ag/Fe sandwich is fabricated and characterized. Giant inverse magnetoresistance is observed in this CPP GMR device.

In the last chapter, I will give a summary of this thesis.

Chapter 2 Fe-N based CPP GMR stacks deposition and nanopillar devices fabrication

2.1 Conventional magnetron sputtering and Facing-target-sputtering

Two different thin film deposition techniques, conventional magnetron sputtering and facing-target-sputtering, are used to prepare the multilayer CPP GMR/TMR thin film stacks. Since the multi sources facing-target-sputtering system was built in our laboratory based on the working principles of conventional magnetron sputtering, we will start with the introduction of conventional magnetron sputtering.

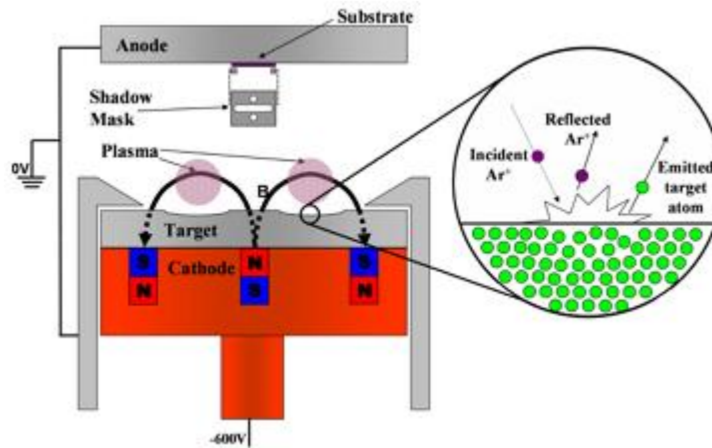

Figure 2.1 Schematic drawing of conventional magnetron sputtering[79].

In conventional magnetron sputtering, the sputter source target is connected to the cathode, and the deposition substrate is connected to the anode of DC power supply or floating, as shown in Figure 2.1. During the sputtering process, neutral Ar gas is introduced to the vacuum chamber and is subsequently ionized to be Ar+ and e- by the

electric field. Plasma is generated through the ionization and confined by the magnetic field near target surface as indicated by the light purple color in the Figure 2.1. Simultaneously, the Ar+ ions are accelerated by the electrical field and bombard the source target. As a result, the source atoms are ejected from the target surface and deposited onto the substrate. In order to control the amount of impurities in the deposited films, sputtering process needs a high base vacuum (normally 10^{-7}-10^{-9} Torr). If the target source material is non-conductive and a DC power source is used for sputtering, negative charges will accumulate on the target surface and they will eventually repeal further Ar-ion bombardment. Thus a stable plasma for sputtering cannot be maintained. In this case, a RF power supply is needed for non-conductive target source, since the negative charge can be dissipated by alternating electric field.

Conventional magnetron sputtering is widely used in thin film deposition. However, there are two main drawbacks when it is used to synthesize the materials with complicated crystal structures, such as iron nitrides. First, since the substrate is exposed to the plasma in conventional sputtering, the plasma radiation and bombardment can significantly influence the film quality and crystallinity. Moreover, if the sputtering targets are consisted of ferromagnetic materials, the magnetic flux tends to stay inside the target rather than escape out of the target surface. Therefore, the magnetic field may not be sufficient to maintain the intensity of plasma thus the deposition rate is low. It is known that more defects can be introduced into the films due to a low deposition rate.

To overcome the above issues of conventional sputtering, facing-target-sputtering technique is introduced for Fe-N thin film deposition[80]. In this sputtering method, two

pieces of targets with the same size and material are installed in the configuration of face to face, as illustrated in Figure 2.2. Magnets are placed behind both targets to generate magnetic field with proper intensity. When negative voltage is applied to both targets, Ar atoms are discharged and the electrons oscillate between the targets in helix motion due to the magnetic field. As mentioned above, the electron-neutron atom collision probabilities are significantly increased because of the geometry of facing-target-sputtering, which results in more intense plasma and higher sputter rate[80,81]. The substrate is installed by side of both targets and with the surface normal to the targets. Given the unique targets and substrate configurations, high energy ions and active electrons tend to stay between the targets other than reaching the substrate. Therefore, the radiation and bombardment damage on the deposited film can be largely reduced[82,83]. In this thesis, the $Fe_{16}N_2$ and Fe_4N thin films are prepared by the DC facing-target-sputtering technique. High quality crystallized Fe-N samples are obtained as shown in later chapters.

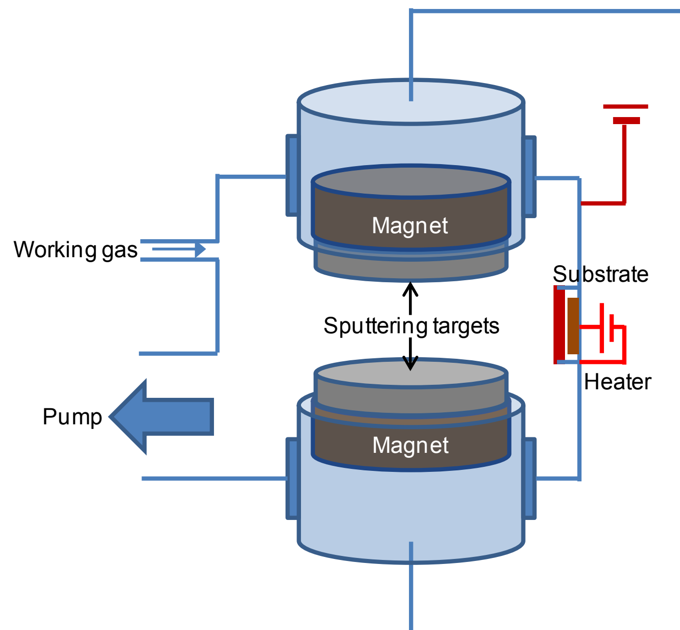

Figure 2.2 Schematic drawing of facing-target-sputtering

In order to prepare full CPP GMR stacks for device fabrication meanwhile maintain the qualities of the interfaces, all the layers, including under layer (also work as electrode), ferromagnetic layers, spacer, and capping layer, need to be deposited in a chamber without vacuum break. Therefore, we have designed and built a multi sources facing-target-sputtering system for Fe-N GMR deposition, as shown in Figure 2.3.

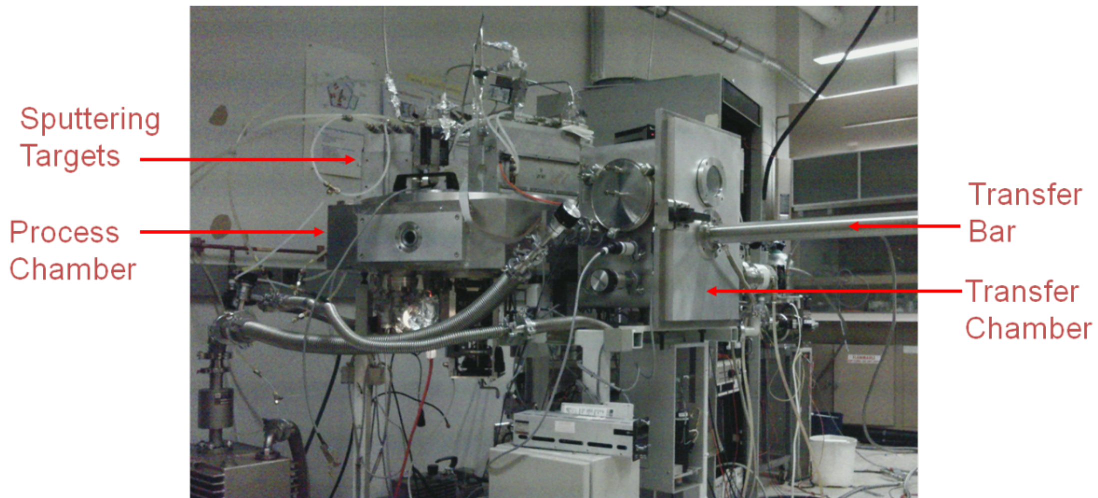

Figure 2.3 Multi sources facing-target-sputtering system

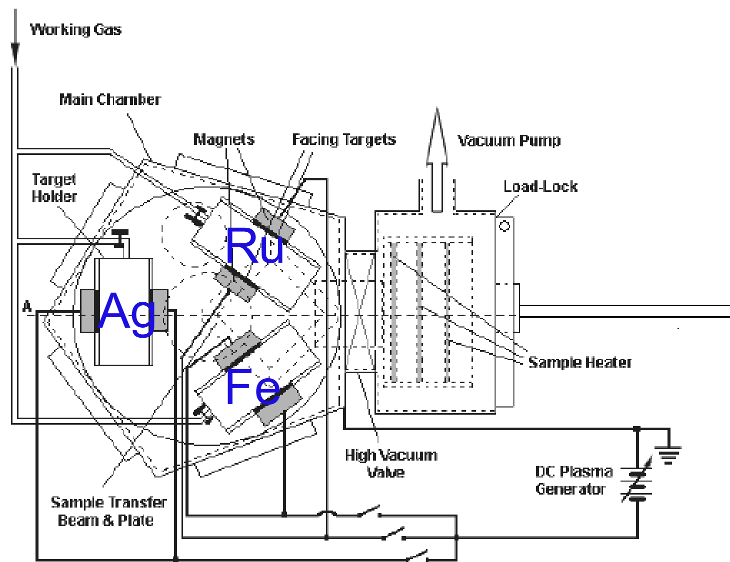

Figure 2.4 Top-down view of the multi sources facing-target-sputtering system

Figure 2.4 shows the top-down view of the multi sources facing-target-sputtering system built in our lab. It consists of a pentagon process chamber, and a large load-lock chamber. The load-lock chamber is able to load multiple pieces of samples each time. A heater is installed in the load-lock chamber to heat up the substrate and to perform the post-annealing. The base vacuum pressures of the system are 4×10^{-8} Torr and 3×10^{-7} Torr respectively for the process chamber and the load-lock chamber. There are three pairs of exchangeable facing targets located in the process chamber. All the targets are 3 inches in diameter and 0.0625 inch in thickness. Each target is fixed in a copper target stage, as shown in Figure 2.5. Two target stages with the same material are placed face-to-face in a rectangular shape target holder. Ar gas with a purity of 99.9999% is introduced into the process chamber to generate plasma during sputtering. The sputtering voltage is applied to the targets through the stages. To prevent the targets from overheated, the targets are cooled by the water-cooling circuits inside the stages.

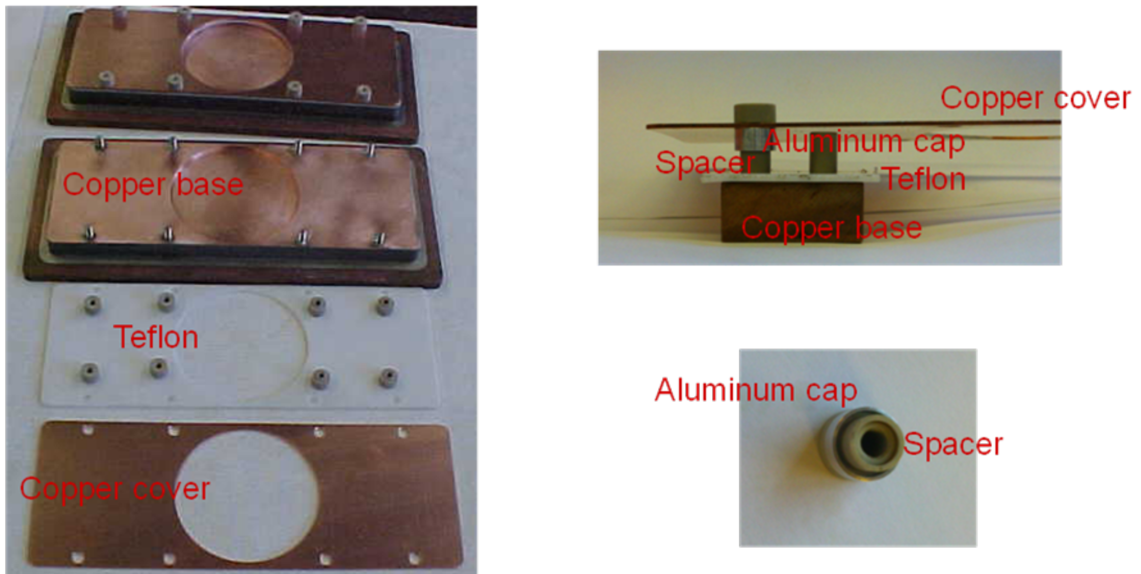

Figure 2.5 Cathode of home built multi sources facing-target-sputtering system

Three pairs of sputtering targets, Fe, Ag, and Ru with purity higher than 99.99%, are installed in the multi sources facing-target-sputtering system. Iron nitride layers can be deposited in the system by reactive sputtering in an Ar and N_2 working gas mixture. The sputtering targets in the system are exchangeable with other materials as needed.

2.2 Fe-N CPP GMR stack development

In the iron nitride CPP GMR full stack deposition, a number of factors need to be considered and controlled. For example, the roughness of buffer layers / bottom electrodes should be minimized to prevent the orange-peel coupling[84] between the free and fixed Fe-N layers. Also, the candidate of buffer layers need to have an appropriate lattice constant and in a desired crystal orientation to facilitate the growth of iron nitrides. In addition, the crystallinity of Iron nitride layers should be good enough to minimize the lattice mismatch at ferromagnetic/non-magnetic interfaces.

Based on these criteria, Ag (001) is selected as the buffer layer / bottom electrode of the iron nitride CPP GMR stacks, as it matches with both $Fe_{16}N_2$ and Fe_4N for their lattice constants. Before the Ag buffer layer, a thin Fe layer is deposited on the MgO (001) single crystal substrate at ~280°C to enhance the adhesion and crystallinity of Ag. The Ag (001) buffer layer is subsequently grown on the thin Fe layer. In pursuit of a small surface roughness, Ag layer is deposited after cooling the substrate to room temperature. Atomic force microscopy (AFM) result shows that a smooth surface of Ag buffer layer (*RMS* rougnness = 0.22nm) is obtained by above recipe. A strong (001)

crystal orientation is achieved in the buffer layer stack, confirmed by X-ray diffraction (XRD) measurements, as seen in Figure 2.6.

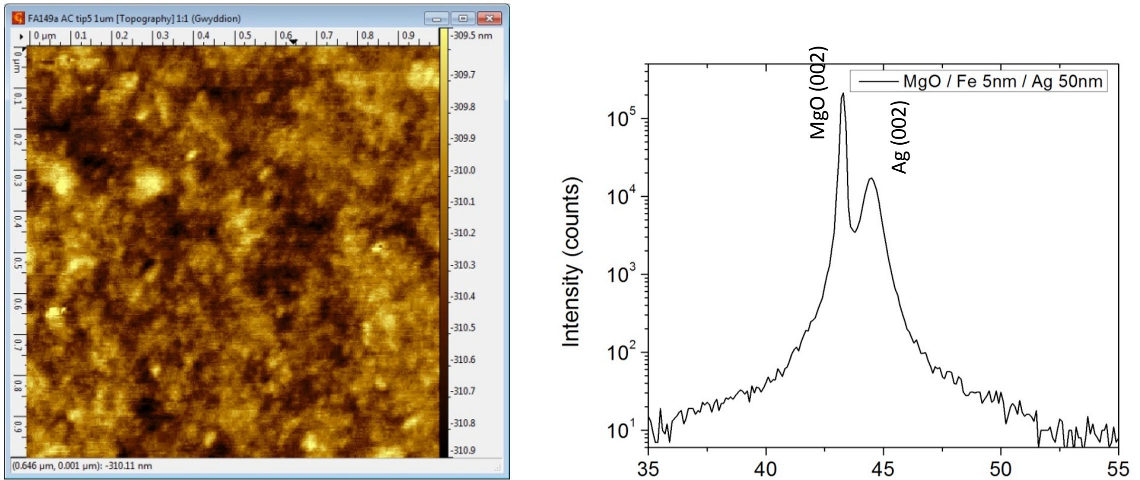

Figure 2.6 AFM image of MgO substrate / Fe 5nm / Ag 50nm (left); X-ray diffraction pattern of MgO substrate / Fe 5nm / Ag 50nm (right).

Figure 2.7 Fe-N CPP GMR stack

$Fe_{16}N_2$ and Fe_4N thin films are both developed on the Ag buffer layers, which will be discussed in detail in following chapters. Fe-N/Ag spacer/Fe-N CPP GMR sandwich, Ag

capping layer and Ru capping layer are subsequently deposited on Ag buffer layers / electrodes to complete the iron nitride CPP GMR full stacks, as illustrated in Figure 2.7.

2.3 Sub-100nm CPP GMR devices fabrication

In this section, I will introduce the fabrication processes that I have developed to make deep sub-micron/nano scale CPP GMR devices. The CPP GMR devices were fabricated in Minnesota Nano Center (MNC, former Nano Fabrication Center) at the University of Minnesota, Twin Cities. Before the Iron Nitride CPP GMR project, our research group had developed processes for sub-micron MTJ device patterning based on positive electron beam lithography and Ar+ ion beam etching. However, these processes involve hard masks to define the nanopillars, which is not an issue for high resistance MTJs but can introduce a large parasitic resistance for devices with low resistivity. Therefore they are not suitable for CPP GMR fabrication. To overcome this issue, fabrication processes based on negative electron beam lithography and Ar+ ion beam etching are developed specifically for the CPP GMR fabrication. The fabrication processes flow is illustrated in Fig. 2.8, which can be seperated into four main blocks: Bottom electrode definition (a-c), CPP GMR nanopillar definition (d), Oxide layer coverage (e) and E-beam resist lift off (f), Via open (g, h) and Top electrode deposition (i). The details of fabrication flows are described as follows:

Step (1): Deposit a thin Ta 5nm / Ru 7nm capping bi-layer on top of CPP GMR stack for extra protection during the device fabrication processes. (Fig. 2.8a)

Step (2): Define the shape of bottom electrode by photolithography. Positive resist 1813 is used for all the photolithography processes for better dimension control. The photolithography process includes following steps: pre-bake, spin coating resist, soft bake, photo exposure, resist developing and hard bake. After resist developing, bottom electrode areas are covered by photo-resist.

Step (3): Etch the bottom electrode by ion beam etching. Ion beam etching is a physical etching process, which removes uncovered area of the metal film stack by Ar^+ ion bombardment. The ion beam incident angle relative to the film surface is critical to this process. Large angle gives a sharp side wall slope on the bottom electrode but could cause re-deposition on the side wall of the photo-resist. Small ion beam angle reduces the risk of re-deposition but results in a shallower etch slope. In our process, the etching starts with a large ion beam angle of 75° until the uncovered area of the stack is fully removed, followed by a 3 min etching with 15° beam angle to clean the side wall. To prevent the photo-resist from overheat, 3 min cooling time is inserted between every 3 min etching sections. (Fig. 2.8b)

Step (4): Photo-resist is stripped after bottom electrode etching. (Fig. 2.8c)

Step (5): Define CPP GMR nanopillars by E-beam lithography. E-beam lithography has a similar mechanism as photolithography in pattern definition and transfer except that the resist is exposed by electron beams instead of UV light. Negative E-beam resist ma-N2403 is used in this process to define the nanopillars. Since we use the negative tone resist as the etching mask, only the nanoscale pillar areas

need to be exposed. The E-beam lithography process consists of: wafer cleaning, pre-bake, spinning coating, soft bake, electron beam exposure, and developing/rinsing.

Step (6): Etch CPP GMR nanopillar. This step is the most crucial one for CPP GMR nanopillar definition. A straight and sharp side wall profile is preferred for the device. In addition, re-deposition and material damage need to be well controlled. To satisfy these requirements, a two-step etching is applied in this process. 85° -90° beam angle is used in the first step to obtain a straight side wall and 15° angle is used for the second step (1-2 mins) to clean the re-deposition. A reference sample is placed in the etching tool as an end point detector. (Fig. 2.8d)

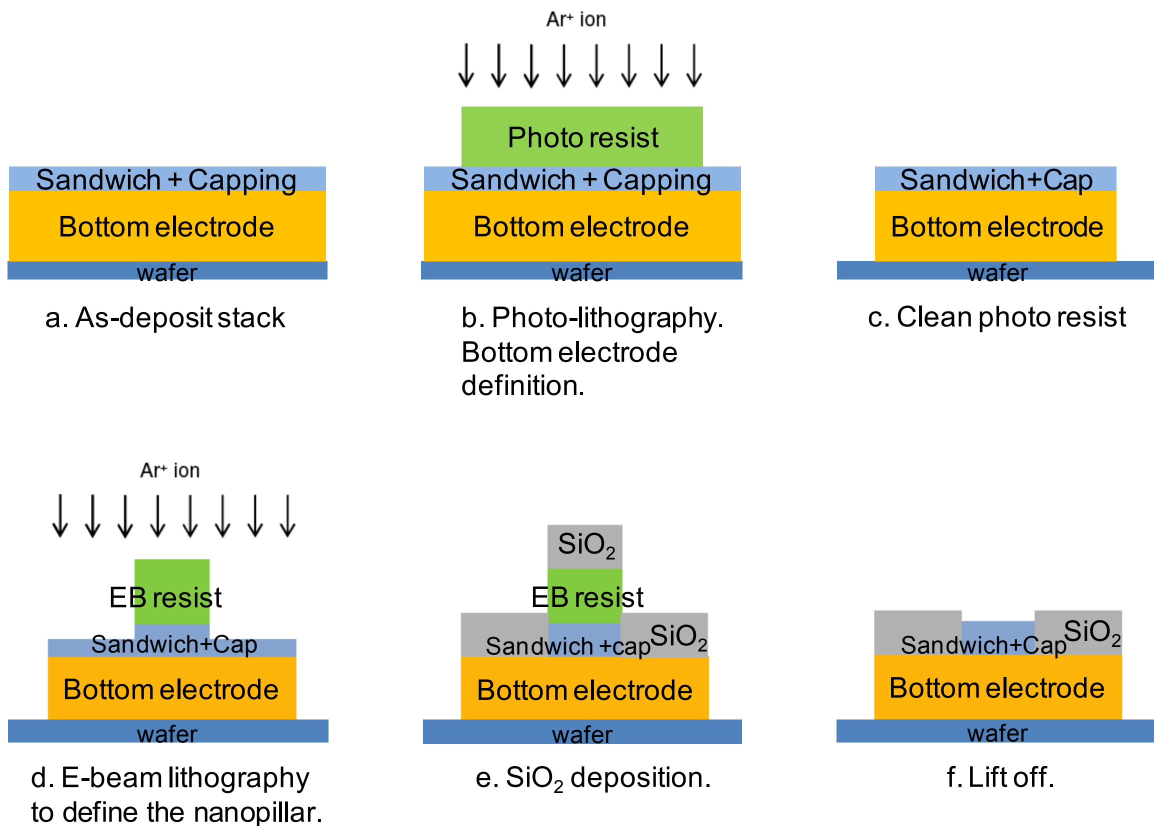

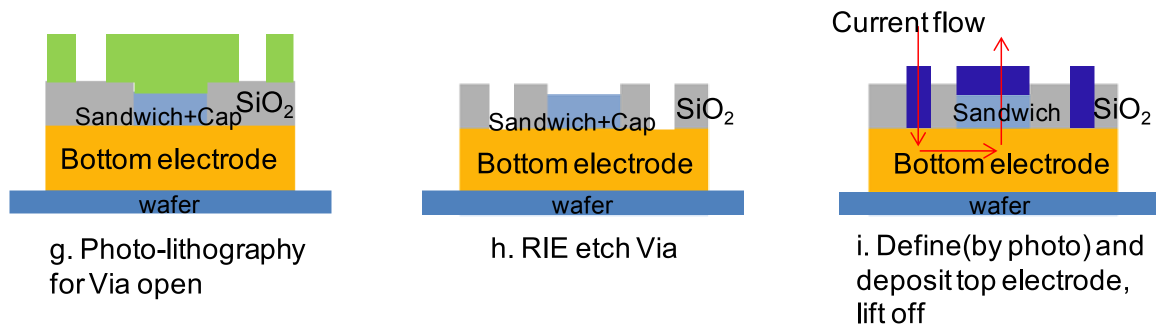

Figure 2.8 Nanometer scale CPP GMR device fabrication flow

Step (7): Deposit SiO_2 to cover the bottom electrode. The purpose of this step is to isolate the bottom electrode from the top electrode and expose the top of the nanopillar in the subsequent Step (8). The SiO_2 is deposited by plasma enhanced CVD (PECVD) for side wall coverage. During the deposition, the E-beam resist is still on top of the CPP GMR pillar. Therefore, the PECVD temperature needs to be kept under 120°C to prevent the resist from overheated. Otherwise the resist could be hard to lift off in the next step. (Fig. 2.8e)

Step (8) E-beam resist lift off. The wafer is soaked in NMP resist striper at 165°C for 2 hours and put in ultrasound for 30 minutes to lift off the E-beam resist. Sometimes resist striper could not reach the resist since the side wall is covered by SiO_2 deposited by PECVD. If that happens, more aggressive lift off process needs to be applied by using foam brush. After the lift off, the bottom electrode is covered by SiO_2 and the top of the CPP GMR nanopillar is exposed. (Fig. 2.8f)

Step (9) Make Via open by photolithography and Reactive ion etching (RIE). Use photolithography to define the areas that need to have Via. Use RIE to etch the uncovered SiO_2. Bottom electrode is partially exposed after Via open is done. (Fig. 2.8 g and h)

Step (10) Photolithography to define top electrode, deposit top electrode by E-beam evaporation, lift off the resist.

Figure 2.9 shows the scanning electron microscopy (SEM) images of the bottom electrode after Step (4) (Left) and E-beam resist pillar after E-beam lithography and developing (right). Figure 2.10 (a) and (b) are the microscope images of as-fabricated CPP GMR devices.

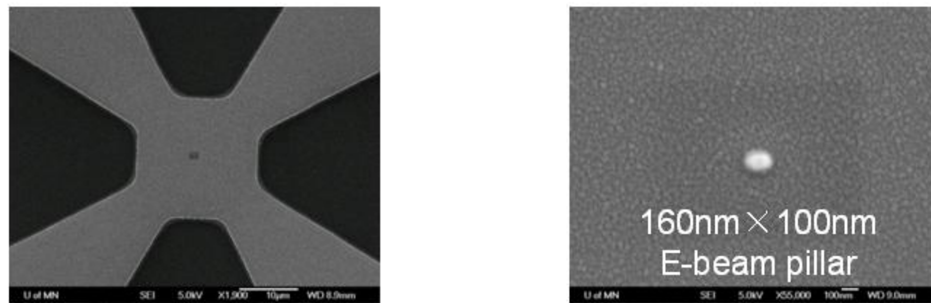

Figure 2.9 SEM images of bottom electrode (left) and Nano pillar (right)

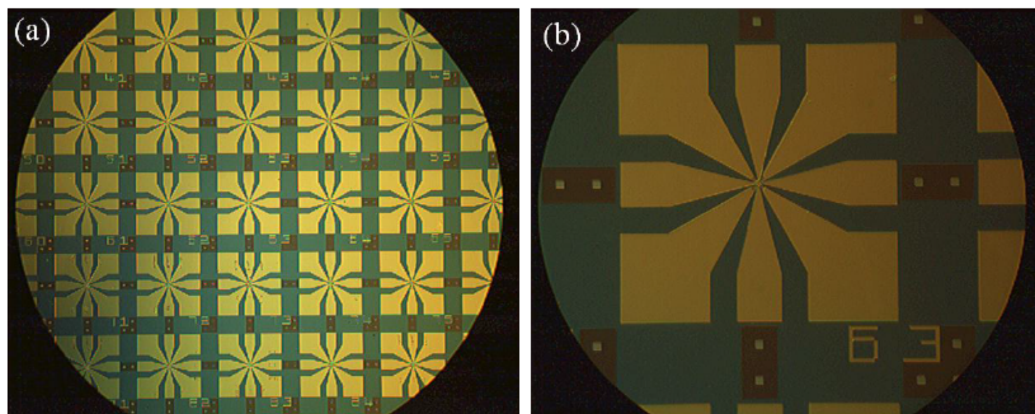

Figure 2.10 Microscope images of finished CPP GMR devices (a) and (b)

2.4 CPP GMR measurement

The resistance and giant magnetoresistance properties of CPP GMR devices are measured by a dc 4-point probe method with a constant sensing current (typically 0.1–1.0 mA), as shown in Figure 2.11. The current is applied on upper side of the top/bottom electrodes by a Keithley 6221 current source and the voltage is measured on lower side of the electrodes by a Keithley 2182 nanovolt meter. Due to the 4-point probe measurement configuration, the lead (electrode) resistance is subtracted, and only the resistance of CPP GMR nanopillar is tested. When measuring CPP GMR devices, a stable contact between the probe and electrode is very important for the resistance signal. Therefore, sometimes we use two Ground Source and Ground (GSG) probes for the 4-point measurement to improve the contact stability. The external field in the measurement is applied by a pair of magnetic coils with additional iron core, which can generate 1000Oe in-plane magnetic field (Figure 2.12). The in-plane coils can be replaced by an alternative perpendicular magnetic coil with 1800 Oe maximum field.

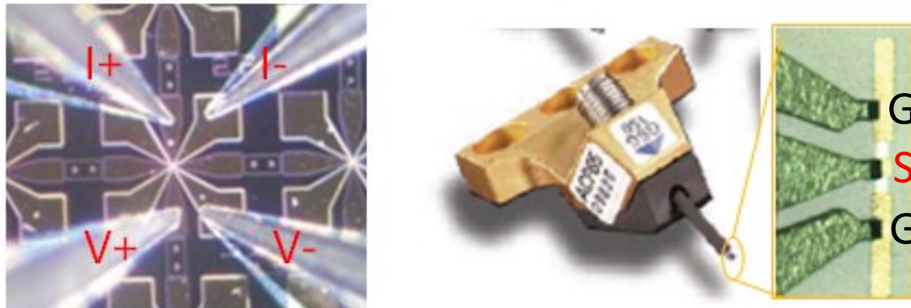

Figure 2.11 CPP GMR device measured by 4-point probe (left); GSG probe (right)

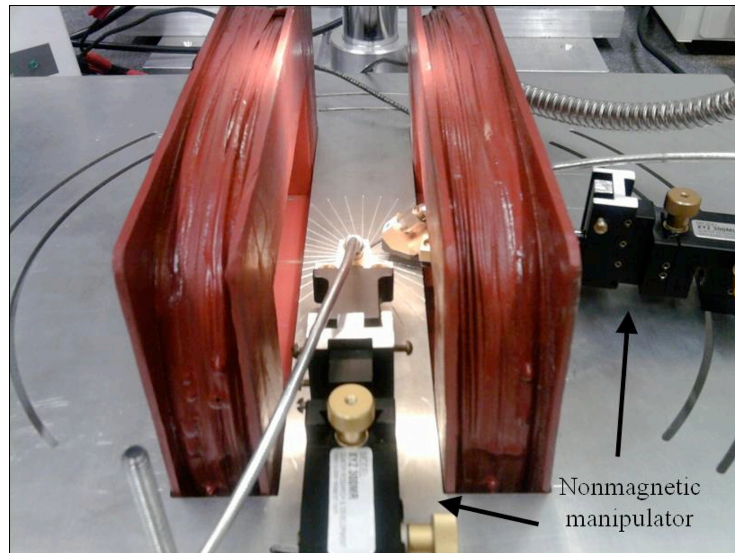

Figure 2.12 CPP GMR measurement setup

In order to measure very small resistance variation or for low temperature measurement, CPP GMR devices are also measured by a Quantum Design PPMS (Physical Property Measurement System), as shown in Figure 2.13. Before the measurement, the wafers need to be diced, and the devices need to be wire bonded to a testing chip. Both in-plane and perpendicular magnetic field can be applied by rotating the samples in the system.

Figure 2.13 Quantum Design PPMS

2.5 Spin polarization measurement by point contact Andreev refection method

All the spin polarization (P) measurements in this thesis are done by point contact Andreev refection (PCAR) method[24]. Andreev refection is a phenomenon in superconductivity, where current can only transport in form of majority and minority spin electron pairs. As shown in Fig. 2.14(a), the electron entering the superconducting condensate needs to pair with another electron in the reverse spin direction. The other electron required for the pair is obtained from the metal, thus a hole with opposite momentum of the incident electron is reflected. If the metal has P = 0, the reflected hole acts as a parallel conducting channel to the electron current, which doubles the conductance in the superconductor. On the contrary, there is no reverse spin state in the metal to pair with the incident electron if P = 100%. As a result, the current in the superconductor is blocked, as shown in Fig. 2.14(b). Therefore, the spin polarization of a metal can be measured by analysis the superconducting current in a circuit with metal/superconductor interface.

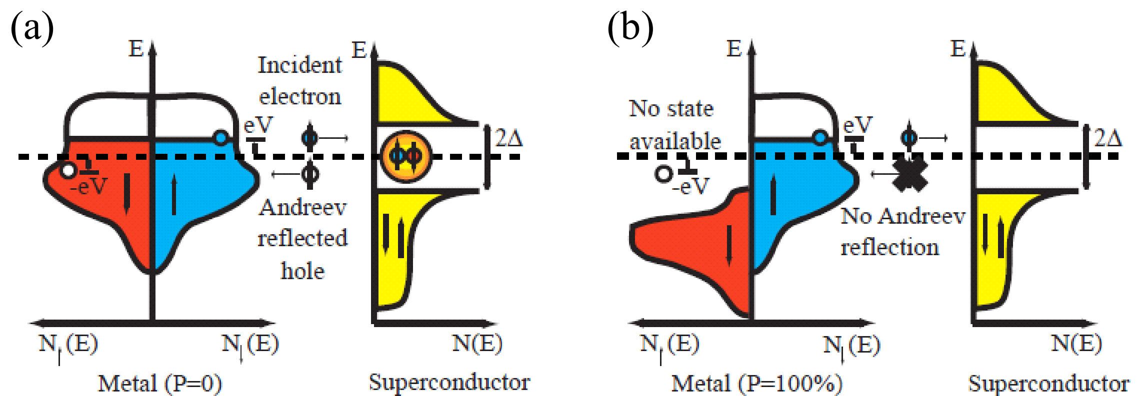

Figure 2.14 Schematic drawing of Andreev refection at metal/superconductor interface[24]

During the PCAR measurement, a superconducting (Nb) tip in the size of a few microns is gently pressed into the sample to minimize the effect of surface oxidation, as illustrated in Fig. 2.15. At least eight such different contacts are created and tested at a temperature of 1.6K. The PCAR experimental curves are fitted by a modified[85] Blonder-Tinkham-Klapwijk (BTK) model[86] with the spin polarization, *P*, and tunnel barrier strength, *Z*, as the fitting parameters. The mean and standard deviation of the eight fitted results are calculated to report the spin polarization of the sample. The PCAR measurements in this thesis are done by Michael Osofsky's group at Naval Research Laboratory.

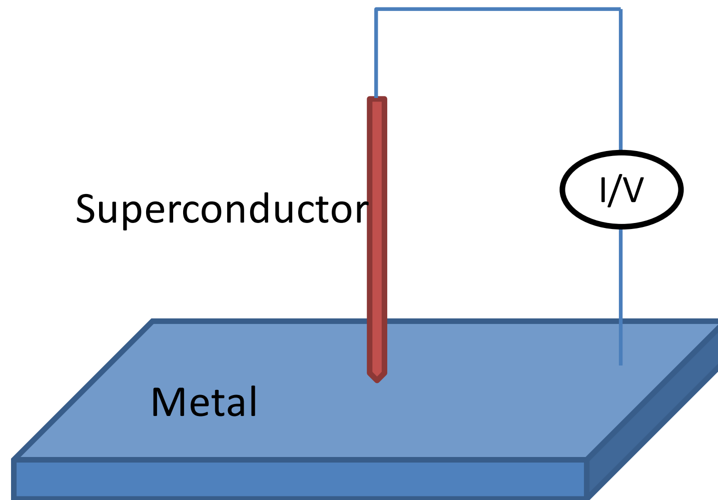

Figure 2.15 Schematic drawing of PCAR measurement circuit

Chapter 3 Heavy-metal free, low damping, and non-interface perpendicular CPP GMR devices based on $Fe_{16}N_2$ magnetic layers

Realization of sub-10 nm spin based logic and memory devices relies on the development of magnetic materials with perpendicular magnetic anisotropy (PMA) that can provide low switching current and large thermal stability simultaneously. In this chapter, a CPP GMR device based on the low damping $Fe_{16}N_2$ magnetic layers has been demonstrated. Crystalline based perpendicular anisotropy of the $Fe_{16}N_2$ in CPP GMR device is measured to be about 1.9×10^6 J/m^3 (1.9×10^7 erg/cm^3), which is sufficient to maintain the thermal stability of sub-10nm devices. A first-principles calculation is performed to support the large magnitude of the perpendicular anisotropy. Moreover, the Gilbert damping constant of the $Fe_{16}N_2$ thin film (α = 0.01) measured by ferromagnetic resonance (FMR) is lower than most existing materials with crystalline PMA. The non-interface perpendicular anisotropy and low damping properties of $Fe_{16}N_2$ may offer a pathway for future spintronic logic and memory devices.

3.1 Limits of state-of-the-art perpendicular magnetic anisotropy material systems

Giant/Tunneling magnetoresistance (GMR/TMR) devices with current-perpendicular-to-plane (CPP) geometry have been attracting substantial attention recently due to their potential applications in spin-transfer-torque RAM (STT-RAM) and logic devices[49,50]. As mentioned in the Chapter 1, the CPP GMR/TMR devices with perpendicular magnetic anisotropy (PMA) hold great promise towards much higher areal densities than the in-plane devices for the new generation spin based memory and logic circuits[69-71].

PMA of thin films can be introduced by reduced magnetic symmetry in the out-of-plane direction. It can be fulfilled by either crystal lattice asymmetry or interface coupling between ultra thin films[69-71,87-90]. Among those PMA materials for the electrodes of magnetoresistive devices, $L1_0$ ordered alloys[71,87] and multilayers[69,88-90] based on transition metals and heavy-elements have been intensively studied due to their high anisotropic constant value (~$10^6 J/m^3$, $10^7 erg/cm^3$). However, these materials usually have a large damping constant and a relatively small spin polarization due to their large spin-orbit coupling[77,91,92], which will lead to a high switching current density

A recently developed Ta/CoFeB/MgO perpendicularly magnetized structure with ultra thin magnetic layers maintains large tunneling magnetoresistance as well as relatively low switching current density[74,93]. Since the PMA of the ultra thin CoFeB layer is induced by the interface anisotropy, the thermal stability of this system may not be sufficient in sub-10 nm scale.

In addition, the very specific layer structure of Ta/CoFeB/MgO perpendicular system limits the choice of spacer/barrier, which can be a drawback to the resistance control for sub-10 nm devices. The total energy consumed by a magnetoresistive device for a single

switching can be written as $J_c^2 \cdot S^2 \cdot R \cdot t$, where S is the lateral area of the device, R is the resistance, and t is the switching time. Assuming we can realize the same J_c and t for both MTJs and CPP GMRs by special material designs, the device with smaller resistance consumes less energy in a single magnetization switching. When the diameter of the magnetoresistive device shrinks to sub-10nm, the resistance of MgO MTJs increases to 10-50 kohm or even higher, which is much larger than that (300-500 ohm) of the CPP GMR devices (Fig. 3.1). As a result, the CPP GMR devices are more likely to satisfy the small energy consumption in STT-RAM and Spin logic circuits in sub-10nm scale.

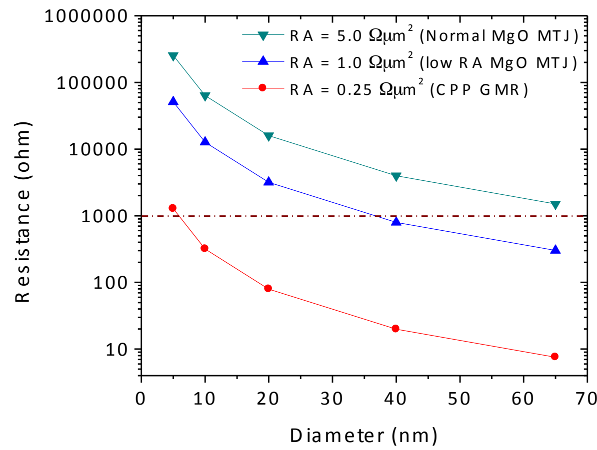

Figure 3.1 Resistance vs. device diameter for MTJs and CPP GMRs

Therefore, a heavy-metal free ferromagnet with large non-interface perpendicular anisotropy is highly demanded for future spintronic applications.

3.2 $Fe_{16}N_2$: a low damping and crystalline based perpendicular material system

Pure Fe has the body center cubic (bcc) crystal structure that possesses cubic anisotropy. With a buffer layer to constrain the in-plane lattice parameter (*a*), Nitrogen (N) dopant atoms introduce a tetragonal distortion to the Fe lattice by expanding its *c* lattice constant, hence magnetic crystalline anisotropy normal to the film plane is introduced in Fe-N martensites due to reduced crystal symmetry[9]. The magnitude of crystalline anisotropy continuously increases as the N doping concentration approaches the interstitial solubility limit (N:Fe at. ratio of 1:8)[11]. Furthermore, upon post-annealing of the Fe-N martensite at its interstitial solubility limit (Fe_8N), even stronger magnetic crystalline anisotropy (~10^6J/m^3, 10^7erg/cm^3) can be developed[9] because of the formation of chemically ordered body-center tetragonal (bct) phase $Fe_{16}N_2$ (Fig. 3.2)[5-7,15]. A strong out-of-plane magnetization component is observed in even partially ordered $Fe_{16}N_2$ thin films. It is expected that nano patterned (001) textured $Fe_{16}N_2$ may possess a magnetic easy axis perpendicular to the plane due to the reduced demagnetization energy. Also, point contact Andreev reflection measurement results have shown that the spin polarization of partially ordered $Fe_{16}N_2$ reaches 0.52, which is comparable to that of CoFe thin film used in current spintronic devices. More importantly, we could expect a low damping constant in $Fe_{16}N_2$ because of its unique heavy-metal free composition.

In our experiment, Ag layer is chosen as a template to constrain the in-plane lattice parameter of Fe-N. The in-plane lattice parameter of Ag (a_{Ag}=4.079Å) closely matches with those of Fe and Fe-N ($a_{Fe\text{-}N}$=2.86Å) martensites with a 45° lattice rotation (Fig. 3.2).

The CPP GMR thin film stack is prepared by the multi sources facing-target-sputtering system that has been introduced in Chapter 2. The base pressure of the sputtering chamber is lower than 4.0×10^{-8} Torr. During the CPP GMR stack preparation, a 5nm Fe layer is first grown onto a pre-cleaned MgO (001) single crystal substrate at 285°C, as an adhesive and seed layer for the following stack. After that, a multilayer structure of Ag(75)/Fe-N(6.5)/Ag(5)/Fe-N(4.5)/Ag(4.2)/Ru(10) (thickness in nanometers) is deposited onto the substrate at ambient temperature. The Fe-N layers are prepared by sputtering Fe targets in Ar and N_2 working gases mixture. The entire stack is prepared in the same multi sources facing-target-sputtering chamber without vacuum break. Subsequently, the film stack is fabricated into devices with 160×100 nm^2 elliptical pillars (Fig. 3.3) by electron beam lithography and Ar ion etching combined processes. Finally, the CPP GMR devices are annealed ex-situ at 150°C for 18 hours to facilitate the formation of the chemically ordered $Fe_{16}N_2$ phase. For X-ray diffraction and ferromagnetic resonance (FMR) measurements, a reference stack of MgO substrate/Fe(5)/Ag(30)/Fe-N(35)/Ru(10) (thickness in nanometers) is prepared.

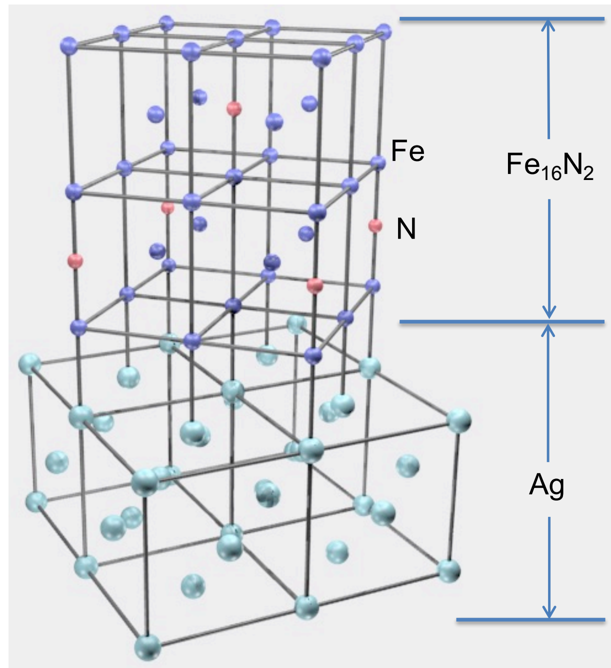

Figure 3.2 The lattice structure of ordered body-center tetragonal (bct) phase $Fe_{16}N_2$ on Ag under layer.

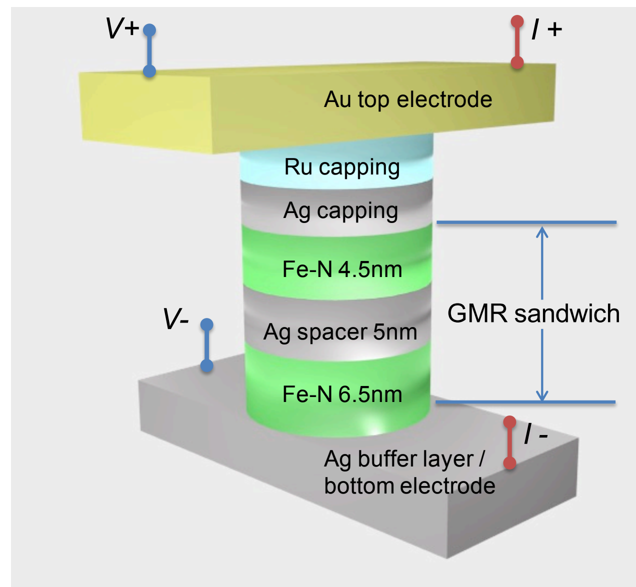

Figure 3.3 Schematic of the Fe-N based CPP GMR device.

Fig. 3.4 shows the out-of-plane X-ray diffraction pattern (measured by Bruker-AXS X-ray Diffractometer with Cu Kα radiation) of the as-deposited Fe(5)/Ag(33)/Fe-N(36)/Ru(6) (thickness in nanometers) multilayers and that of the same sample annealed at 150°C for 18 hours. Besides the peaks of MgO substrate and Ag seed layer, a peak at 2θ=59.2° can be observed for the as-deposited sample, which corresponds to the diffraction from the Fe_8N (002) crystal planes. After the post-annealing, this peak shifts to a lower 2θ angle by 0.2°, indicating that the crystal plane elongates along the out of plane (001) direction. Simultaneously, the $Fe_{16}N_2$ (002) peak at 2θ=28.6° develops, which is identified as the fingerprint of phase transformation from Fe_8N to $Fe_{16}N_2$. The degree of N site ordering of the annealed Fe-N thin film is determined to be D=35% by a previously developed calculation method, showing that the sample is partially ordered.

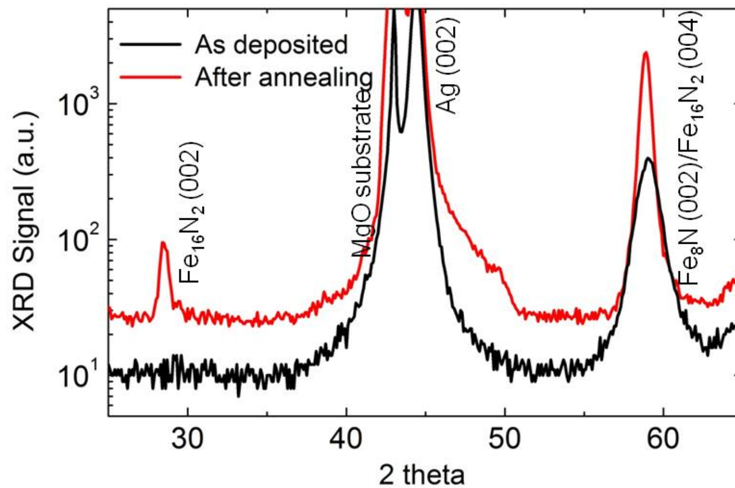

Figure 3.4 The out-of-plane X-ray diffraction patterns of as-deposited and annealed samples with the same layer structure MgO/Fe(5)/Ag(33)/Fe-N(36) /Ru(6) (thickness in nanometers).

In Fig. 3.5, the in-plane hysteresis loops (measured by a Princeton Measurement Vibrating Sample Magnetometer) of an as-deposited sample and a post-annealed (150°C for 18 hours) sample with the same nominal structure (MgO substrate/Fe(5)/Ag(33)/Fe-N(36)/Ru(6) (thickness in nanometers)) are compared. As the Ag buffer layer is thick enough to decouple the Fe and Fe-N layers, the in-plane magnetization switching can be divided into three segments: Segment 1: switching of the Fe under layer; Segment 2: switching of the in-plane component of the Fe-N layer; Segment 3: switching of the out-of-plane component of the Fe-N layer. The switching fields for the Fe layer are the same for both as-deposited and annealed samples, whereas a much larger magnetic field (H_s) is required to saturate the annealed Fe-N layer. Considering the saturation magnetization (M_s) of the Fe-N layer increases after post-annealing, substantial increase of crystal anisotropy (K_u) can be expected due to the formation of partially ordered $Fe_{16}N_2$ phase.

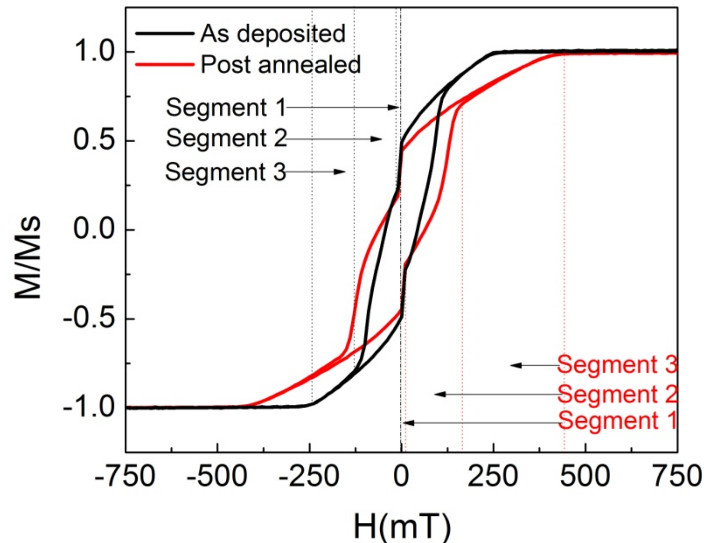

Figure 3.5 The in-plane hysteresis loops of the as-deposited and annealed Fe-N samples.

Fig. 3.6 (a) shows a high-resolution scanning transmission electron microscopy (HRSTEM) image of the $Fe_{16}N_2$/Ag/$Fe_{16}N_2$ GMR sandwich with a [Fe-N 110 || Ag 100] zone axis, measured by Prof. Paul M. Voyles's team in University of Wisconsin. The STEM electron energy loss spectroscopy (EELS) shows N K and Fe L edges from the $Fe_{16}N_2$ layers as indicated in Fig. 3.6 (b). The N/Fe ratio of the $Fe_{16}N_2$ thin film is 0.12 ± 0.02, which indicates that the $Fe_{16}N_2$ thin film is nearly stoichiometric.

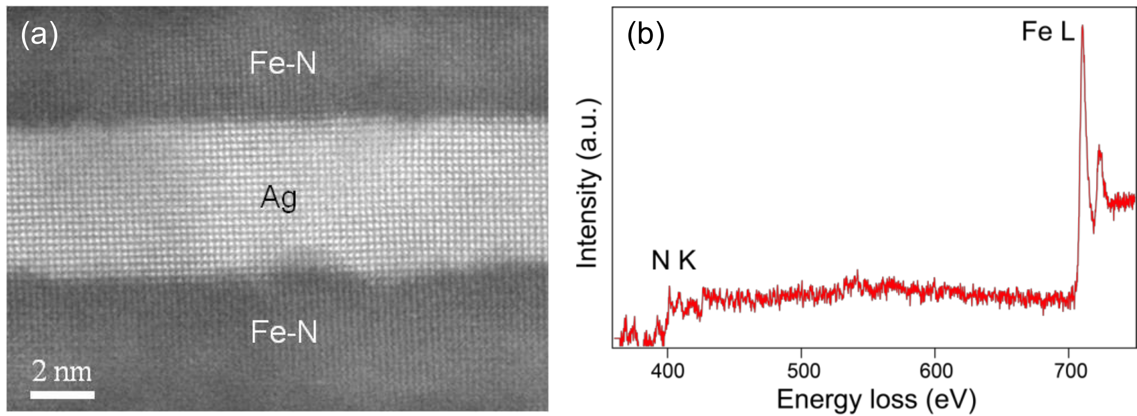

Figure 3.6 (a) High-resolution scanning transmission electron microscopy (HRSTEM) image of the $Fe_{16}N_2$/Ag/$Fe_{16}N_2$ GMR sandwich with a [Fe-N 110 || Ag 100] zone axis. (b) STEM electron energy loss spectroscopy (EELS) of the Fe-N layer.

The HRSTEM images in Fig. 3.7 (a) show atomically sharp $Fe_{16}N_2$/Ag interfaces with little inter-diffusion between those two layers, confirmed by STEM EELS spectrum imaging (SI). The power spectrum of the HRSTEM image is shown in Fig. 3.7 (b). The superlattice reflection from ordered $Fe_{16}N_2$ (002) crystal planes (highlighted by the yellow circles) confirms that partially order $Fe_{16}N_2$ presents in the Fe-N thin film, which coincides with the X-ray diffraction pattern of the annealed Fe-N sample (Fig. 3.4).

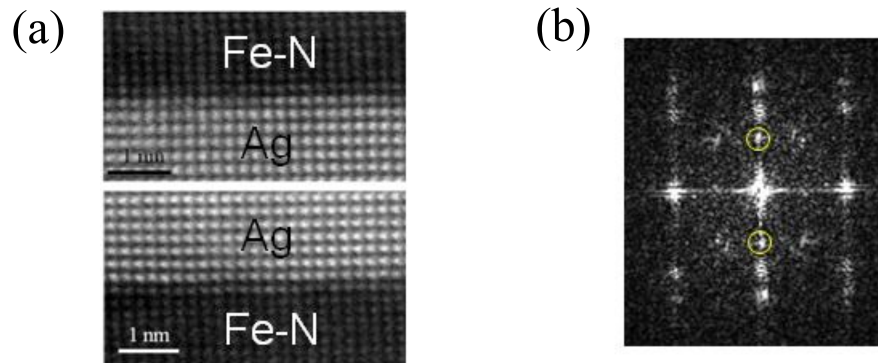

Figure 3.7 (a) The cross-sectional HRSTEM images of upper and lower interfaces of Fe-N/Ag/Fe-N GMR sandwich layers. The zone axis is along [Fe-N 110 || Ag 100] direction. (b) The power spectrum of the Fe-N/Ag/Fe-N HRSTEM image. The superlattice reflection from ordered $Fe_{16}N_2$ (002) crystal planes is highlighted.

To confirm the multilayer structure of the Fe-N CPP GMR stack, we perform both Auger electron spectroscopy (AES, Physical Electronics Model 545) and X-ray photoelectron spectroscopy (XPS) depth profile measurements on our thin film sample. In the AES depth profile (Fig. 3.8), the AES surveys are carried out after each sputter cycles. Each sputter cycle corresponds to 30 seconds of Ar ion etching time. We have ensured that the AES surveys are dense enough to identify every layer and interface in the stack.

The same multilayer structure is observed in the XPS depth profile. Fig. 3.9 shows the XPS Fe $2p^{1/2}$ binding energy of the top and bottom Fe-N layers in the CPP GMR stack. The XPS Fe $2p^{1/2}$ binding energy in both Fe-N layers remains the same at all the XPS survey positions.

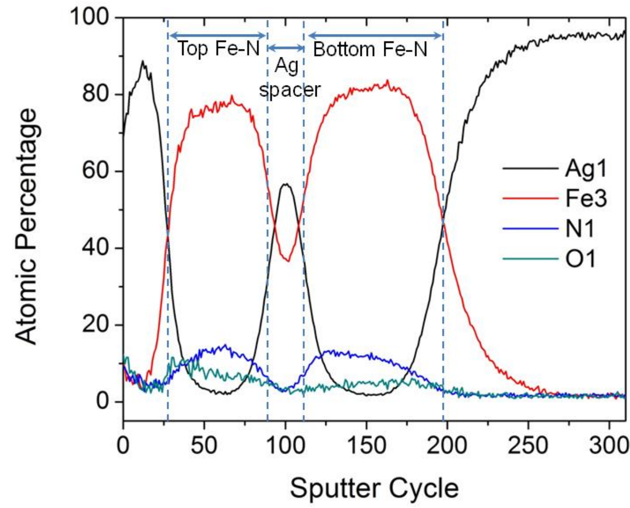

Figure 3.8 Auger electron spectroscopy (AES) depth profile result of the Fe-N CPP GMR thin film stack.

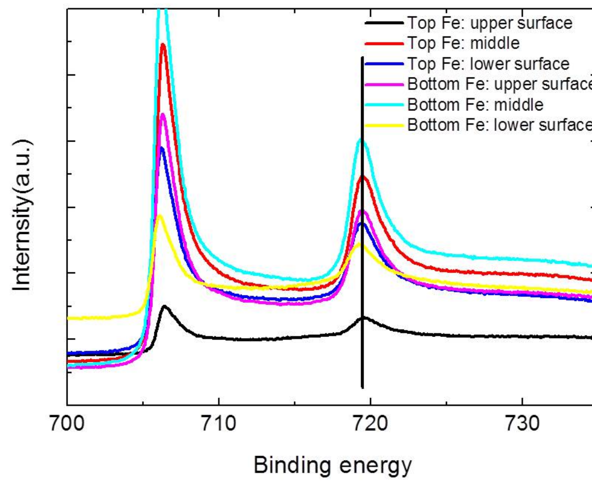

Figure 3.9 The X-ray photoelectron spectroscopy (XPS) Fe $2p^{3/2}$ binding energy of the top and bottom Fe-N layers in the CPP GMR stack. The upper surface, middle and lower surface in the caption indicate the position where the XPS surveys are taken.

3.3 Magnetoresistance of $Fe_{16}N_2$ based perpendicular CPP GMR devices

The CPP GMR thin film stack is subsequently fabricated into 160×100 nm^2 elliptical pillars by electron beam lithography and Ar ion etching combined processes mentioned in Chapter 2. The CPP GMR devices are annealed ex-situ at 150°C for 18 hours to facilitate the formation of chemically ordered $Fe_{16}N_2$ phase after nanoscale device fabrication.

The room temperature magnetoresistance signal of the partially ordered $Fe_{16}N_2$ CPP GMR device is measured in a physical properties measurement system (PPMS). A standard butterfly shaped giant magnetoresistive loop is observed when the magnetic field sweeps in the out-of-plane direction (Fig. 3.10). Sharp switching of the resistance occurs at ± 55mT (550Oe) and ± 400mT (4000Oe), which corresponds to the magnetization switching of the free layer and fixed layer respectively. While during the in-plane magnetic field sweeping, the resistance value of the CPP GMR device remains almost a constant (Fig. 3.10a), indicating that the magnetic easy axes of both free and fixed layers are normal to the film plane. We also acquire the minor R-H loop of the same device by only switching the magnetization of the free layer (Fig. 3.10b). In ± 100mT(1kOe) magnetic field range, the resistance change and the switching field of free layer coincide with those in the major R-H loop. The difference in coercive field of the free layer and the fixed layer can be explained by their different shape anisotropy and magnetic crystalline anisotropy values.

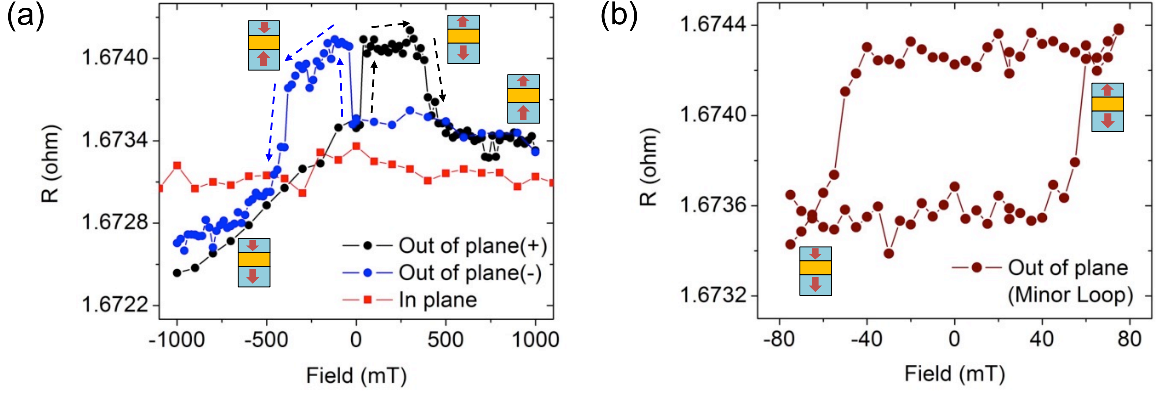

Figure 3.10 GMR signal of perpendicular $Fe_{16}N_2$ based CPP GMR device. (a) Giant magnetoresistance signal of a partially ordered $Fe_{16}N_2$ CPP GMR (post-annealed) as a function of out-of-plane magnetic field (black and blue circles) and in-plane magnetic field (red squares). The black and blue circles represent positive and negative field sweeping direction respectively. (b) Giant magnetoresistance minor loop of the partially ordered $Fe_{16}N_2$ CPP GMR device.

To calculate the perpendicular anisotropy constant of the partially ordered $Fe_{16}N_2$, an analysis is performed based on the Stoner Wohlfarth model of the fixed layer of the CPP GMR device. The total energy of the nanomagnet can be written as:

$$E = \left(K + \frac{2K_s}{t_F}\right)\sin^2\theta \; - \; {\mu_0}^2 H M_s \cos(\varphi - \theta) - \frac{1}{2} N_z {\mu_0}^2 M_s^2 \sin^2\theta \qquad \text{Eq. 3-1}$$

where K is the crystalline perpendicular anisotropy of the partially ordered $Fe_{16}N_2$. K_s is the perpendicular anisotropy introduced by the $Fe_{16}N_2$/Ag interface. t_F is the fixed layer thickness. N_z is the demagnetization factor in perpendicular direction. φ represents the angle between the applied field and the film normal direction, and θ is the angle between the fixed layer magnetization and the film normal direction. By taking the energy minimum as $\partial E/\partial\theta = 0$, the relationship between volume/interfacial anisotropy, switching field and demagnetization can be written as:

$$K + \frac{2K_s}{t_F} = \frac{1}{2}(\mu_0{}^2 H M_s + N_z \mu_0{}^2 M_s^2) \quad \text{Eq. 3-2}$$

The value of N_z is calculated to be 11.01 for the fixed layer nanomagnet[94]. M_s is determined to be 1.79×10^6A/m (1790emu/cm^3) from the VSM measurement result of the CPP GMR thin film stack. Here I also assume that the $Fe_{16}N_2$/Ag interface has the same K_s as the Fe/Ag interface, which is 0.8mJ/m^{-2} (0.8erg/cm^2) from reported results[95]. Consequently, the K value is calculated to be 1.876×10^6J/m^3 (1.876×10^7erg/cm^3), which is very close to the result derived from the torque curve measurement (1.6×10^6J/m^3, 1.6×10^7erg/cm^3)[8].

To verify that the formation of partially ordered $Fe_{16}N_2$ increases the perpendicular anisotropy, the R-H loops of the as-fabricated (not annealed) Fe_8N CPP GMR device with the same lateral dimension are also measured (Fig. 3.11). Giant magnetoreistance signals are observed when magnetic field sweeps both in-plane and out-of-plane. The result reveals that the magnetic easy axis of the Fe_8N CPP GMR device is partially out of plane.

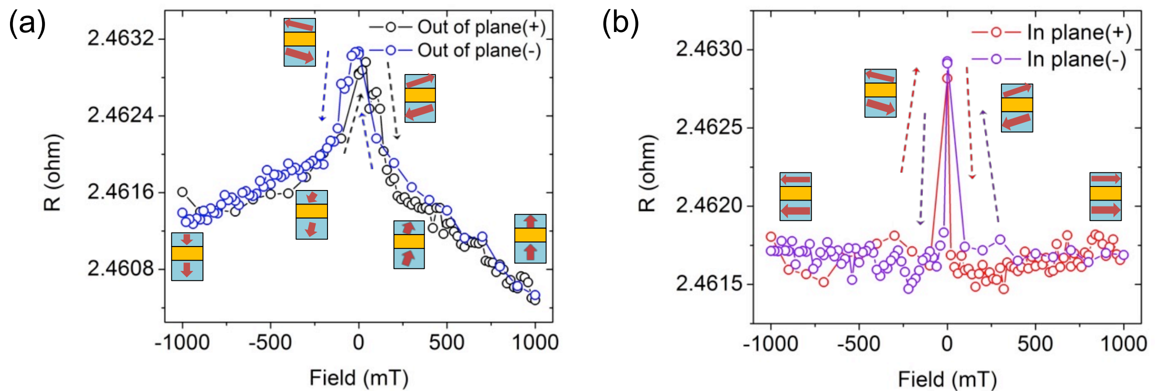

Figure 3.11 Giant magnetoresistance signal of a Fe-N CPP GMR (as-fabricated) as a function of out-of-plane (a) and in-plane (b) magnetic field. The black and blue circles (a) represent positive and negative field sweeping in out-of-plane

direction. The red and purple circles (b) represent positive and negative field sweeping in in-plane direction.

During the perpendicular magnetic field sweeping, the magnetization of the free and fixed layers starts from parallel alignment normal to the film plane, with the presence of large negative field. When the magnetic field decreases, the magnetization of both magnetic layers tilts toward the in-film-plane direction, accompanied with the gradual increase of the device resistance. Next, an increase of resistance occurs at -45 mT external field, which corresponds to the switching of the out-of-plane component of the free layer magnetization. After that, the magnetic field sweeps to the positive polarity, causing the switching of the fixed layer magnetization at a field equal to 130 mT. Finally, the magnetization of both the free and fixed layers aligns perpendicularly by a large positive magnetic field. The reversed evolution of the magnetization happens as the field sweeps back from positive to negative direction. When the magnetic field sweeps in-plane, the magnetization of the free and fixed layers favors a quasi-parallel state with the presence of magnetic field (Fig. 3.11b). While at remanence, a quasi-antiparallel state is favorable due to the dipolar interaction, which results in the resistance jump near zero magnetic field.

The previous point contact Andreev reflection (PCAR) results demonstrated that the spin polarization ratio of partially ordered $Fe_{16}N_2$ is 52% [9], which is as large as that of CoFe. However, both the ΔR and giant magnetoresistance ratio are smaller than those of CoFe/Cu/CoFe CPP GMR. The lower magnetoresistance signal than expectation is attributed to the electron band mismatch between $Fe_{16}N_2$ and Ag layers. Since the bulk

spin dependent scattering of $Fe_{16}N_2$ is quite small due to its low resistivity, the CPP GMR of the $Fe_{16}N_2/Ag/Fe_{16}N_2$ sandwich is mainly contributed by the interfaces. There are existing calculation results showing that both majority and minority spin bands of $Fe_{16}N_2$ have several electron bands across the Fermi level[96]. Consequently, the interface spin scattering asymmetry between the two spin states is small, since neither spin electron bands match well with the electron band of Ag. It suggests that the choice of the spacer of $Fe_{16}N_2$ based CPP GMR is crucial to further improve the giant magnetoresistance signal of the device.

3.4 The scaling limit of $Fe_{16}N_2$ perpendicular material system

To further investigate the mechanism of the large crystalline perpendicular anisotropy observed in $Fe_{16}N_2$, Prof. Mryasov's team in University of Alabama perform first-principles calculations of anisotropy constant *K* for different lattice constants as summarized in Fig. 3.12. The calculation is based on DFT-LDA method and includes the effect of Coulomb correlations on the crystalline magnetic anisotropy of $Fe_{16}N_2$ [97]. To illustrate how the variation of lattice constants (seed layer effect) influence the effective anisotropy constant, they show a contour plot of crystalline anisotropy constant K ($\times 10^6$ J/m^3) calculated for U-J = 4 eV. For a certain *a* constant (5.72 Å e.g.), increasing the *c* lattice can improve the anisotropy constant *K* which coincides with the results of doping N into Fe lattice to increase the *c* lattice of Fe-N. Note that further increasing the *c* lattice up to around 6.7 Å can continuously enhance the anisotropy constant *K* according to the

calculation result. However, this cannot be realized by over-doping of N since the extra N atoms can destabilize the Fe-N phase. The optimized lattice constants for stability and anisotropy are a = 5.71Å and c = 6.45-6.61Å, with calculated values of K = 1.8-2.1×10^6 J/m^3. These calculated values are in a reasonable agreement with that of the fixed layer in $Fe_{16}N_2$ CPP GMR device, where K= 1.9×10^6 J/m^3. They also find good agreement with the measurements for MBE grown films by Sugita et.al[8], in which K= 1.55-1.60×10^6 J/m^3. Following the results shown in Fig. 3.12, it has a slight increase of K in the range of lattice constants highlighted with green contour (a ~ 5.63Å and c ~ 6.74Å).

Maintaining the thermal stability of the free/pinned layer nanomagnet ($K_u V / k_B T \geq 60$ for 10 years) is one of the most important issues for the scaling of magnetoresistive device. The recently developed Ta/CoFeB/MgO system maintains perpendicular magnetic anisotropy (PMA) and its thermal stability by the interfacial coupling between Ta/CoFeB and CoFeB/MgO layers. It has been demonstrated that this perpendicular magnetic system is able to support device as small as 22nm[98]. However, if the size of the device is further scaled down to sub-10nm, the thermal stability of this system is no longer large enough[75] because of its ultra thin magnetic layer thickness [Fig. 3.13 (a)]. Besides, the magnitude of perpendicular anisotropy constant of this system decreases dramatically with thicker CoFeB layer. One cannot gain much thermal stability by increasing the thickness of CoFeB, for example, to 5nm, while maintaining the perpendicular anisotropy [Fig. 3.13(b), Fig. 3.13(c)].

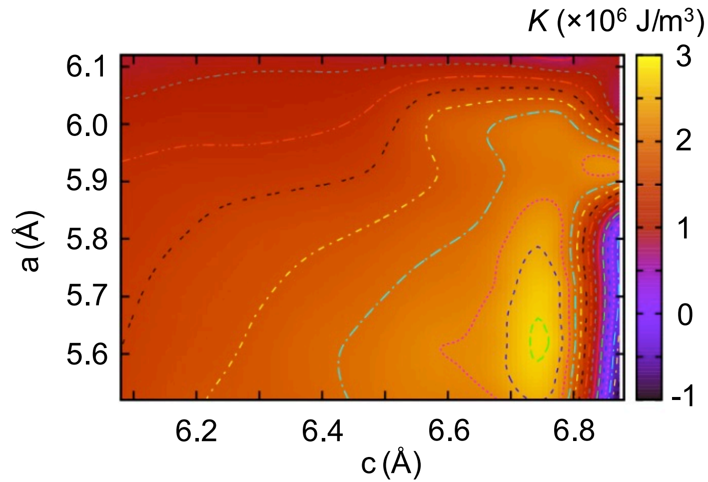

Figure 3.12 Calculated crystalline anisotropy of $Fe_{16}N_2$ as a function of a,c

In comparison with the Ta/CoFeB/MgO system, the $Fe_{16}N_2$ has more robust perpendicular anisotropy for the sub-10nm magnetoresistive devices due to its non-interface (crystalline based) perpendicular characteristic. The magnitude of the perpendicular anisotropy of $Fe_{16}N_2$ does not decrease with thicker film thickness so that we can obtain higher thermal stability by increasing the volume of the $Fe_{16}N_2$ nanomagnet [Fig. 3.13(c)]. Moreover, thicker film thickness in sub-10nm dimension can significantly reduce the demagnetization factor in perpendicular direction. Therefore the perpendicular anisotropy and thermal stability can be further promoted in the $Fe_{16}N_2$ system.

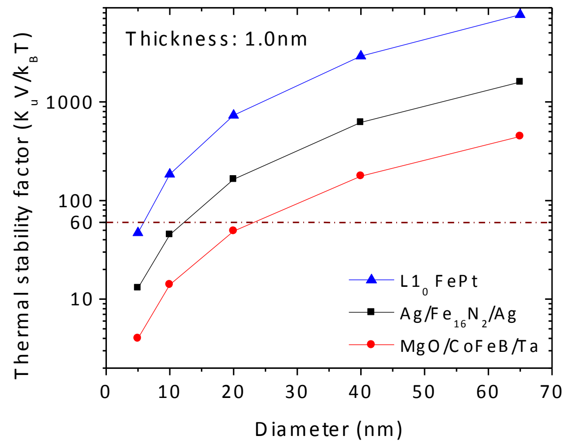

Figure 3.13 (a) Thermal stability factor vs. device diameter with 1.0nm magnetic thin films

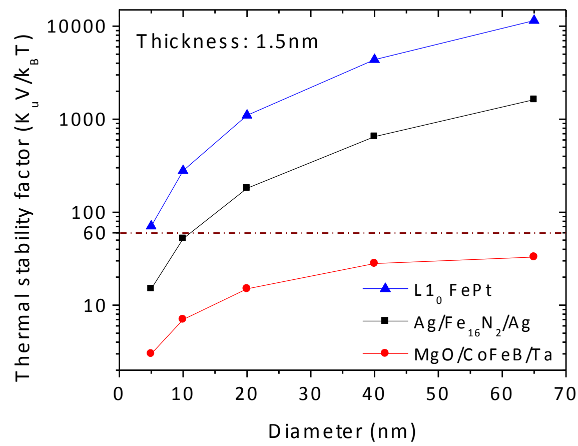

Figure 3.13 (b) Thermal stability factor vs. device diameter with 1.5nm magnetic thin films

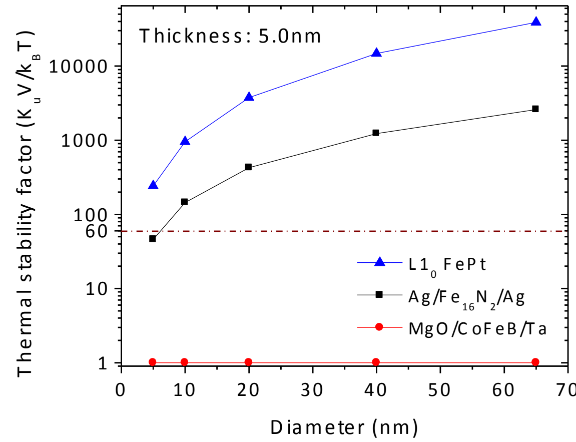

Figure 3.13 (c) Thermal stability factor vs. device diameter with 5.0nm magnetic thin films. In such a thickness, the magnetic easy axis of MgO/CoFeB/Ta structure is in-plane.

Another crystalline based PMA material, FePt, can also satisfy the requirement of thermal stability for sub-10nm magnetoresistive devices. However its damping constant α is 20-26 times larger than $Fe_{16}N_2$ [77,92]. As discussed above, the large damping constant can tremendously increase the critical switching current density of the device.

3.5 Improving the magnetoresistance signal

As mentioned in section 3.3, the electron band mismatch between $Fe_{16}N_2$ and Ag causes the small magnetoresistance ratio and resistance change in our $Fe_{16}N_2$/Ag/$Fe_{16}N_2$ CPP GMR devices. To improve the magnetoresistance signal, thin Fe layers are inserted between both $Fe_{16}N_2$/Ag and Ag/$Fe_{16}N_2$ interfaces. It has been known that the electron band of Fe matches with that of Ag for the majority spin electrons, but they mismatch for

the minority spin electrons. Consequently, such interfacial spin scattering asymmetry can improve the magnetoresistance behavior.

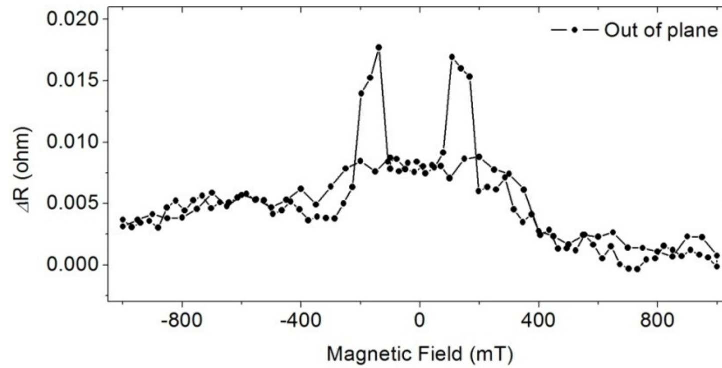

Figure 3.14 (a) The Out-of-plane R-H loop of CPP GMR with Fe16N2/Fe composite magnetic layers

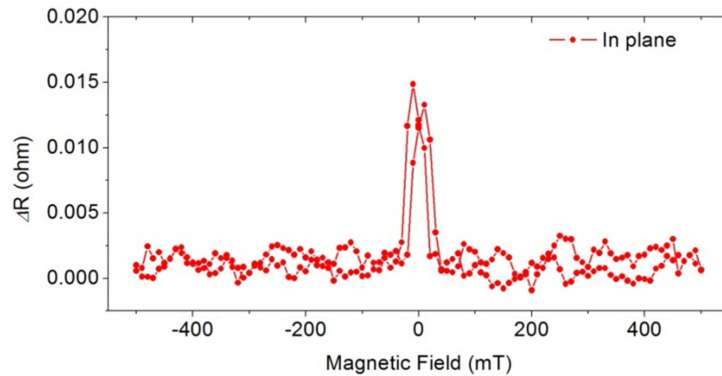

Figure 3.14 (b) The In-plane R-H loop of CPP GMR with Fe16N2/Fe composite magnetic layers

The following film stack is deposited on single crystal MgO substrate: Fe(5)/Ag(60)/Fe_8N(8.5)/Fe(0.67)/Ag(5)/Fe(0.67)/Fe_8N(4.5)/Ag(5)/Ru(12) (from the substrate side, thickness in nanometers). XRD pattern of this sample show lower Fe_8N (002) peak intensity than the GMR stack in the main article, indicating weaker crystalline perpendicular anisotropy of this sample. The film stack is subsequently fabricated into 60nm × 60nm circular devices, and the devices are post-annealed to promote partially

ordered $Fe_{16}N_2$. Both out-of-plane and in-plane R-H loops show magnetoresistance component (Fig. 3.14). The coercivities of the out-of-plane switchings are much larger than those of in-plane switchings, indicating that the anisotropy of the device is mostly out of plane. The ΔR value is one order of magnitude larger than the $Fe_{16}N_2$/Ag/$Fe_{16}N_2$ CPP GMR, and the ΔRA value increases by a factor of 3. The MR signal can be further improved if we properly integrate $Fe_{16}N_2$ into MTJ devices.

3.6 Damping constant of $Fe_{16}N_2$

In order to approximate the damping constant of the $Fe_{16}N_2$ thin film with perpendicular crystalline anisotropy, the ferromagnetic resonance (FMR) frequency of a partially ordered $Fe_{16}N_2$ sample with 35nm thickness has been characterized at different bias magnetic fields. FMR is measured inside a microwave cavity with an electromagnet as shown in Fig. 3.15(a). In a magnetic film with perpendicular magnetic anisotropy, the FMR resonance frequency (f) and the magnetic field (H_r) are connected through this relation[99-102]:

$$f = \frac{\gamma}{2\pi}(\mu_0 H_r - \mu_0 M_s + \frac{2K}{M_s}) \qquad \text{Eq. 3-3}$$

where γ is the gyromagnetic ratio, M_s is the saturation magnetization, and K is the perpendicular magnetic anisotropy constant. Fig. 3.15(b) demonstrates the FMR spectrum of the $Fe_{16}N_2$ measured at the excitation frequency of 10, 12, 14, and 16 GHz. It is clear

that the resonance field has a blue shift from 100 to 300 mT upon increasing the microwave excitation frequency from 10 to 16 GHz. The FMR resonant field has been shown as a function of the excitation frequency as seen in Fig. 3.15(c). FMR frequency has a linear relation to the field which is consistent with Eq. 3-3. In addition, the perpendicular magnetic anisotropy constant and gyromagnetic ratio have been extracted from the curve fitting of Eq. 3-3 over the experimental data (Fig. 3.15(c)). Utilizing the saturation magnetization M_s = 1.9×10^{6}A/m (1900 emu/cm^3) derived from the VSM measurement, it is found that K = 2.27×10^{6}J/m^3 (2.27×10^7 erg/cm^3) and γ = 2.62×10^5 m/A.s indicating that $Fe_{16}N_2$ has a quite large perpendicular magnetic anisotropy. The damping constant of the film can be extracted from the FMR linewidth as shown in Fig. 3.15(d). At an excitation frequency of 15 GHz, the FMR center field is about 160 mT (1.6 kOe) and the FMR linewidth is about 9.63 mT (96.3 Oe). The Gilbert damping constant is related to the FMR linewidth by $\Delta H ; \frac{4\pi\alpha f}{|\gamma|}$ relation *(27)* from which the damping constant is calculated to be about α = 0.01.

We have also performed the ferromagnetic resonance (FMR) characterization by changing the external field angle relative to the out of the plane direction [z-axis in Fig. 3.16(a)]. The resonance frequency can be written as[103,104]:

$$(\frac{2\pi f}{\gamma})^2 = [H\cos(\theta-\theta_0)+H_u\cos 2\theta_0][H\cos(\theta-\theta_0)+H_u\cos^2\theta_0] \qquad \text{Eq. 3-4}$$

where θ is the angle of the magnetic field from z-axis, θ_0 is the rest position of the magnetization from the z-axis, and $H_u = 2K/M_s - \mu_0 M_s$. Fig. 3.16 (b) shows the angle

measurement of the resonant field for an excitation frequency of 14 GHz together with the curve fitting of the Eq. 3-4 overlaid on the experimental results in our $Fe_{16}N_2$ thin film. From the curve fitting, it is found that H_u = 0.338 T where results in $K = 2.56\times10^6$ J/m^3, which is similar to the result obtained from the fitting of Eq. 3-3 in Fig. 3.15(c).

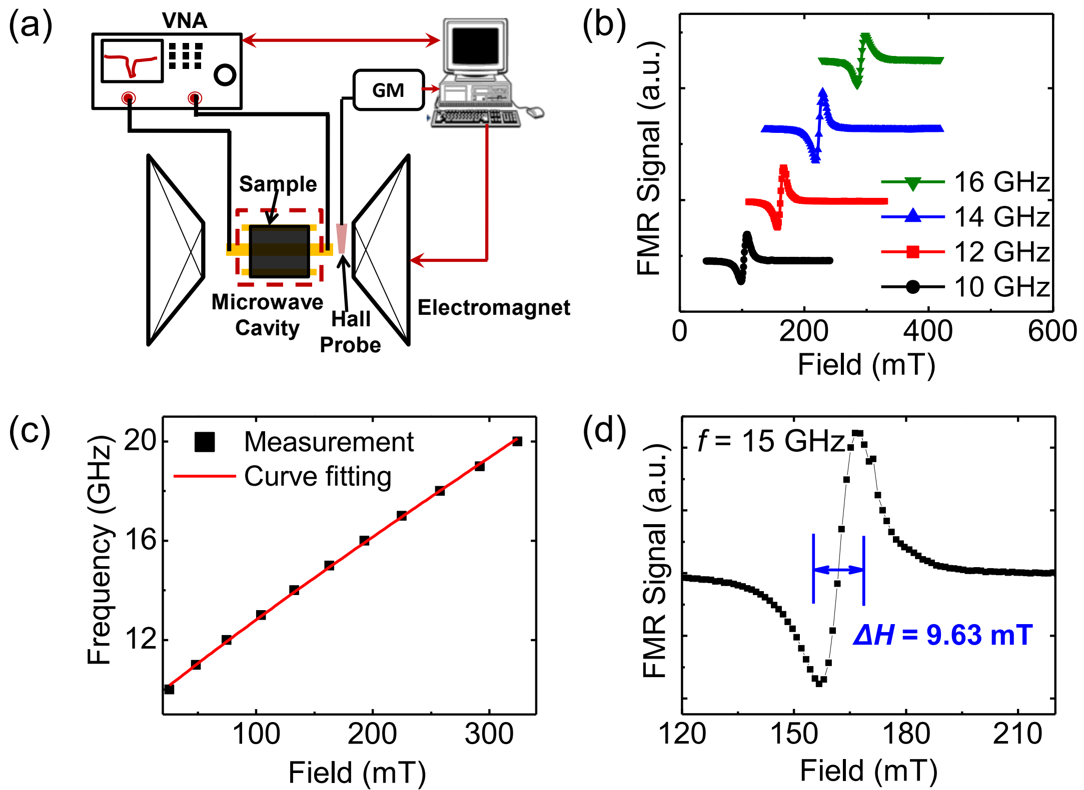

Figure 3.15 FMR spectra of partially ordered Fe16N2. (a) FMR characterization setup including vector network analyzer (VNA), microwave cavity, and electromagnet where all control from computer. (b) FMR characterizations of the Fe16N2 film at the excitation frequency of 10, 12, 14, and 16 GHz. (c) The FMR magnetic fields as a function of excitation frequency overlaid with the Kittel formula curve fitting. (d) FMR linewidth measured at the excitation frequency of 15 GHz.

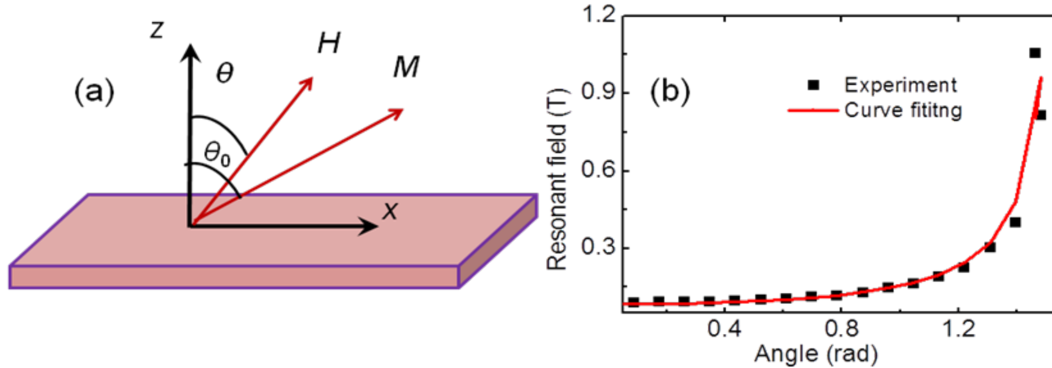

Figure 3.16 (a) Angle measurement of the FMR characterization (b) The experimental results of the angle measurement of the FMR on $F_{16}N_2$ for the excitation frequency of 14 GHz with the curve fitting data.

The Gilbert damping constant is very small knowing that $Fe_{16}N_2$ has a large perpendicular magnetic anisotropy of about $K \sim 2\times10^6$ J/m^3. Comparing the Gilbert damping in $Fe_{16}N_2$ with another perpendicular ferromagnetic material FePt, which has a PMA constant of about 6×10^6 J/m^3, could lead to an interesting implication. The damping constant of $L1_0$ ordered FePt is about 0.2-0.26[77,92], which is at least 20 times larger than the damping constant in $Fe_{16}N_2$. The switching current density could be 10-15 times lower for $Fe_{16}N_2$ than that for $L1_0$ FePt, if we consider their M_s difference and assume that they have the same energy barrier to overcome. Small damping constant in $Fe_{16}N_2$ is in fact not surprising since there is no heavy element like Pt or Pd in the ferromagnetic material composition. It is known that heavy elements result in large damping of the magnetization dynamics due to their large spin-orbit coupling. Absence of heavy elements in the $Fe_{16}N_2$ structure makes the damping constant in $Fe_{16}N_2$ very similar to soft magnetic materials. This merit makes $Fe_{16}N_2$ a better choice for the spintronic

devices with low switching current than the current PMA materials (eg. $L1_0$-FePt, CoPt and FePd).

3.7 The limitations of $Fe_{16}N_2$ perpendicular material system

The main drawback of the $Fe_{16}N_2$ perpendicular system is its chemical instability at high temperature. As mentioned in Chapter 1, the α''-$Fe_{16}N_2$ is a metastable phase which decomposes to be Fe and Fe_4N at above 250°C[105]. Although we develop the $Fe_{16}N_2$ perpendicular system in the CPP GMR with Ag spacer, which does not require post annealing to show the magnetoresistance, its giant magnetoresistance signal is small. It is expected that the optimum platform for $Fe_{16}N_2$ is the MTJs with MgO barrier due to its decent tunneling magnetoresistance ratio. However, to crystallize the MgO barrier and adjacent magnetic layers to facilitate coherent tunneling, the MTJ stack needs to be annealed at 250-300 ^{o}C, which is higher than the decomposition temperature of $Fe_{16}N_2$. To stabilize the α''-$Fe_{16}N_2$ phase at higher temperature, researches have introduced dopants to partially substitute the Fe atoms. For example, it was found that the doping of Ti for less than 10% atomic ratio increases the chemical stability of α''-$Fe_{16}N_2$ at higher temperature than pure iron nitride[106]. Another method to obtain more stable α''-$Fe_{16}N_2$ is to partially replace the N atoms by substance with larger atomic size, for instance phosphorus. The improvement on thermal chemical stability of $Fe_{16}N_2$ has yet to be discovered.

In addition, as mentioned in section 3.3, both the majority and minority electron bands of $Fe_{16}N_2$ don't match with that of Ag. Since the band structures of MgO and Ag are similar, it is expected that the electron bands of $Fe_{16}N_2$ may also not match with that of MgO, which could cause lower tunneling magnetoresistance ratio than the existing CoFeB/MgO MTJs. In order to mitigate this issue, an ultra thin Fe or CoFeB layer could be inserted between $Fe_{16}N_2$ and MgO, therefore the band mismatch can be partially corrected. With the $Fe_{16}N_2$/Fe (or CoFeB) composite free/pinned layers, the device can take advantages of the large bulk perpendicular anisotropy of $Fe_{16}N_2$ as well as the the high spin tunneling asymmetry of MgO/Fe (or CoFeB) interface.

3.8 Summary

In this chapter, I have demonstrated the feasibility of a heavy-metal-free, low damping and non-interface perpendicular CPP GMR device for future spintronic applicatioins. The crystalline perpendicular anisotropy K of $Fe_{16}N_2$ is derived to be $1.876\times10^6 J/m^3$ ($1.876 \times 10^7 erg/cm^3$) and the coercivity of the $Fe_{16}N_2$ layer is up to 400 mT based on the fabricated ~100nm scale device. The damping constant of the $Fe_{16}N_2$ thin film is determined as 0.01 by a ferromagnetic resonance measurement, about 50 times smaller than that of the $L1_0$ FePt perpendicular material. Compared with the existing CoFeB-MgO based perpendicular MTJ, the perpendicular anisotropy in our device is not limited by the thickness of the magnetic layer. That will enable its scaling down to sub 10 nm

while maintaining its thermal stability. The limitations of $Fe_{16}N_2$ perpendicular system is also discussed.

Chapter 4 Deposition and spin polarization study of Fe_4N thin films with (111) orientation

In this chapter, the (111) oriented Fe_4N thin films have been developed and the spin polarization of (111) Fe_4N has been studied. The Fe_4N thin films with (111) out-of-plane orientation are successfully deposited on thermally oxidized Si substrate using a facing-target-sputtering system. The buffer layer, N:Fe composition, and substrate temperature during sputtering are optimized to promote the formation of the Fe_4N phase and to induce the (111) out-of-plane orientation. Furthermore, the spin polarization of the (111) Fe_4N is measured by the point contact Andreev reflection (PACR) technique. The thickness dependence of the spin polarization is also studied.

4.1 Introduction

As we discussed in Chapter 1, Fe_4N has been attracting attentions in spintronics due to its large spin asymmetric conductance and negative spin polarization at the Fermi level. To date, most of the spintronics related studies on Fe_4N are based on epitaxial or polycrystalline thin films with (001) out-of-plane orientation[29,107,108]. It is worthwhile to explore Fe_4N films with other orientations for the purpose of multilayer stack integration. For example, the (111) crystal plane is sometimes preferred by exchange bias materials for tunneling/giant magnetoresistive (TMR/GMR) devices[109]. To improve its flexibility

for applications, it is also of interest to deposit Fe_4N on the non-magnetic metal buffer layers rather than single crystal substrates, as the metal layers underneath Fe_4N may facilitate a variety of spintronics devices[1,2]. Although the spin polarization (SP) of Fe_4N was reported on a (001) oriented Fe_4N thin film[23], the SP ratio of a material is closely related to its growth conditions and crystallinity. Therefore, studying the spin polarization of Fe_4N grown on a practical metal buffer layer is also very helpful for its applications in spintronics.

In this chapter, I have deposited polycrystalline Fe_4N thin films on thermally oxidized Si substrates. Strong (111) out-of-plane orientation is induced by a Ta/Ru composite buffer layer. The nitrogen compositions of the films and the deposition temperature are tuned to optimize the phase formation of Fe_4N. Moreover, the spin polarization of the (111) oriented Fe_4N is measured by the point contact Andreev reflection (PACR) method. The thickness dependence of the spin polarization is also studied.

4.2 Deposition of polycrystalline Fe_4N (111) thin films

Fe_4N multilayer stacks with a structure of Si thermal oxide/Ta(2nm)/Ru(18nm) /Fe_4N(40nm) are prepared. The Ta/Ru composite buffer layer is first deposited on the thermally oxidized Si substrate at room temperature in a Shamrock conventional sputtering system. After that, the substrate is transferred to a facing-target-sputtering system that has only a pair of Fe targets, as shown in Figure 2.2. The base pressure of the sputtering chamber is lower than 6.0×10^{-8}Torr. Fe_4N layer is deposited by reactive sputtering at different substrate temperatures, i.e., 120, 150, 200 and 250°C. To obtain

near stoichiometric Fe_4N thin films, the N_2 partial pressure varies from 0.5 mTorr to 1.0 mTorr while the Ar working gas pressure is maintained at 10 mTorr.

The Fe_4N phase and out-of-plane orientations are detected by θ-2θ X-ray diffraction (XRD) using a Simens Bruker D5005 system with Cu Kα radiation. X-ray photoelectron spectroscopy (XPS) is measured by a Surface Science SSX-100 system to further characterize the compositions and the binding energies of the Fe_4N thin films. Magnetic properties of the samples are examined by Princeton Measurements vibrating sample magnetometry (VSM). The surface roughness is characterized by an Agilent 5500 atomic force microscope (AFM).

Figure 4.1 shows the out-of-plane X-ray diffraction (XRD) patterns of Fe-N thin films deposited on Ta/Ru buffer layers. A strong hcp-Ru (0002) diffraction signal can be observed in the θ-2θ XRD results. Since Ru does not match with either Ta or Si for their in-plane lattices, the growth mode of the Ru buffer layer is expected to be fiber-textured instead of epitaxial. This is confirmed by the XRD in-plane φ scan, in which no diffraction peak is observed for the Ru due to various lattice rotations in the in-plane direction. The γ'-Fe_4N has the face-centered-cubic Fe lattice with a N atom located at the body center. The in-plane lattice constants of (111) oriented Fe_4N and (0001) Ru are 2.68Å ($a_{Fe4N}/\sqrt{2}$) and 2.69Å (a_{Ru}) respectively, with only a 0.4% lattice mismatch between the Fe_4N [111] and Ru [0001] planes. Therefore, the Ta/Ru buffer layer can facilitate the deposition of (111) oriented Fe_4N. Followed by the growth mode of the Ta/Ru buffer layer, the (111) Fe_4N thin film is also fiber-textured.

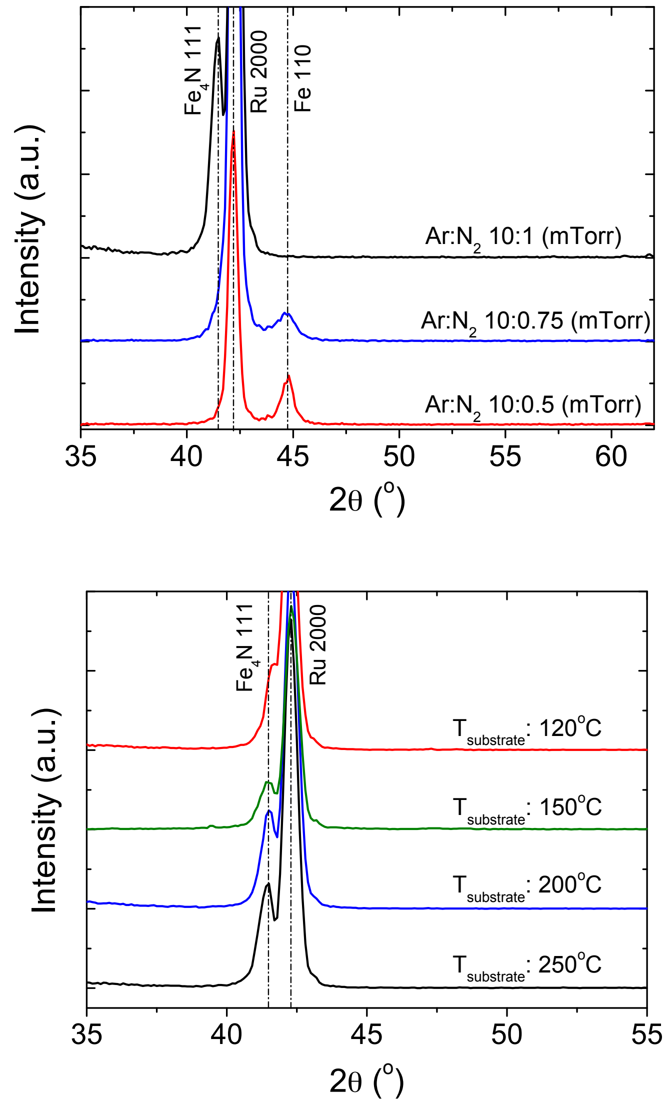

Figure 4.1 Out-of-plane X-ray diffraction patterns of 40nm Fe_4N thin films deposited with (a) different N2 partial pressures; (b) different substrate temperatures.

Based on the Fe-N phase diagram, several iron nitride compounds can be formed with different Fe:N compositions and temperatures, thus the N_2 partial pressure and substrate temperature need to be controlled in the deposition processes. Figure 4.1(a) shows the out-of-plane XRD patterns of Fe-N thin films deposited with different N_2 partial

pressures. The substrate temperature is maintained at 250°C for all the conditions in Figure 4.1(a). When the N_2 partial pressure is 0.5 mTorr, Fe (011) diffraction peak is present in the XRD result, which indicates that the nitrogen composition is insufficient. As the N_2 partial pressure is increased to 0.75 mTorr, the Fe diffraction peak intensity drops, and the Fe_4N (111) peak starts to show up. As we further increase the N_2 partial pressure to 1.0 mTorr, the Fe_4N (111) peak becomes very pronounced, and the Fe (011) signal entirely disappears. Diffraction peaks from other iron nitrides, for examples Fe_3N near $2\theta = 57.5°$ and 60.8°, are absent. Fine tuning the N_2 partial pressure by ±0.1 mTorr around 1.0 mTorr slightly decreases the Fe_4N (111) peak intensity. In subsequent X-ray photoelectron spectroscopy (XPS) results, we also observe that the N/Fe atomic ratio is nearly stoichiometric for the 1.0 mTorr N_2 sample. Therefore, the N_2 partial pressure is optimized at 1.0 mTorr for the growth of Fe_4N thin films.

Figure 4.1(b) shows the out-of-plane XRD results of Fe_4N deposited at different substrate temperatures. As the temperature is gradually tuned from 120°C to 250°C, the intensity of Fe_4N (111) diffraction peaks increases continuously. The strongest Fe_4N (111) signal is observed on the sample deposited at 250°C. Constrained by the deposition system set-up, the substrate temperature cannot be further increased during deposition. Alternatively, we post-anneal the best sample (deposited at 250°C) in a different vacuum chamber. When the annealing temperature is set to be 325°C, no noticeable change is shown in the XRD result. The saturation magnetization of the optimized sample is measured to be 1250 emu/cm^3 by vibrating sample magnetometry, as shown in Figure 4.2, which is consistent with our previous experiment result for Fe_4N[110].

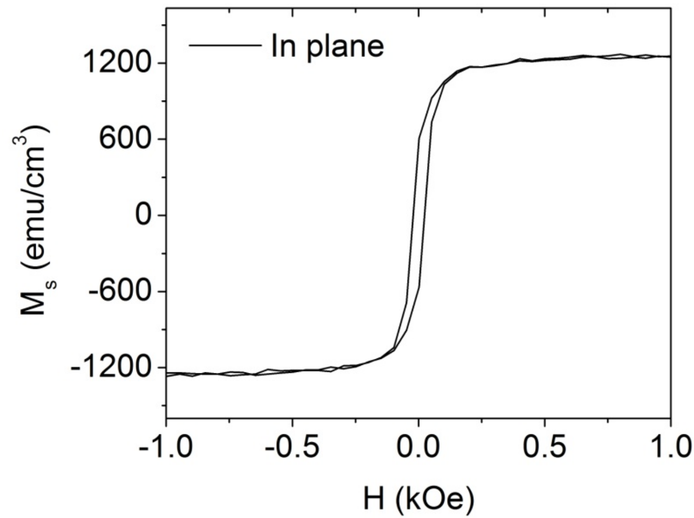

Figure 4.2 Hysteresis loop of 40nm polycrystalline (111) Fe_4N thin film

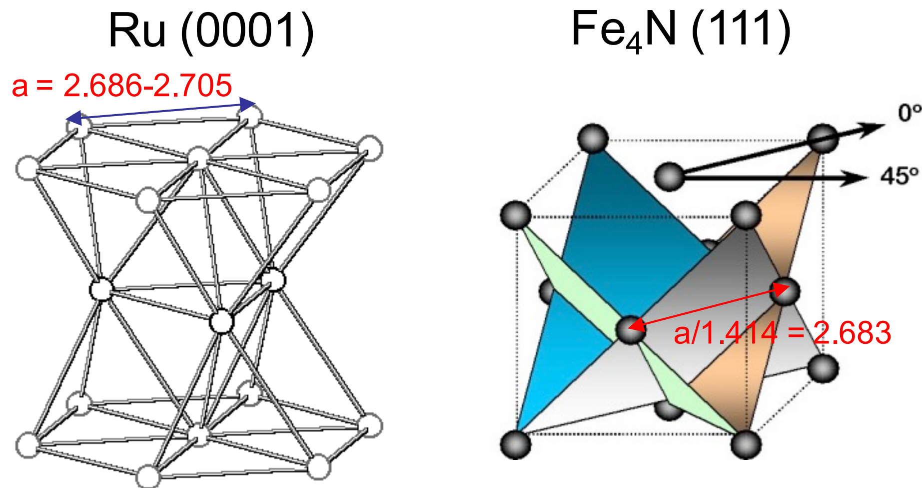

Figure 4.3 Out-of-plane X-ray diffraction patterns of 40nm Fe_4N thin films deposited on thermally oxidized Si substrates with Ru, Pd and Pt buffer layers.

To demonstrate the effect of buffer layers on the (111) preferred orientation of Fe_4N, we also substitute the Ru (0001) buffer layer with Pd (111) and Pt (111) layers. Compared to

the small lattice mismatch between the Fe_4N [111] and Ru [0001] planes (i.e. 0.4%, as shown in Figure 4.3), the mismatches of Pd [111] and Pt [111] are 3.8% and 4.2% respectively. With the optimized N_2 partial pressure and substrate temperature, the Fe_4N (111) XRD peaks can barely be detected when the films are deposited on 18nm Pd or Pt layers, as shown in Figure 4.4. In contrast, the sample deposited on the Ru (0001) buffer layer shows a substantially stronger (111) diffraction signal. No Fe_4N peak from the other crystal plane, i.e. (002) at 2θ = 47.8° or (022) at 2θ = 71.2°, is observed in the XRD results. Thus we conclude that the Ru (0001) buffer layer is quite effective for inducing the (111) out-of-plane orientation of Fe_4N.

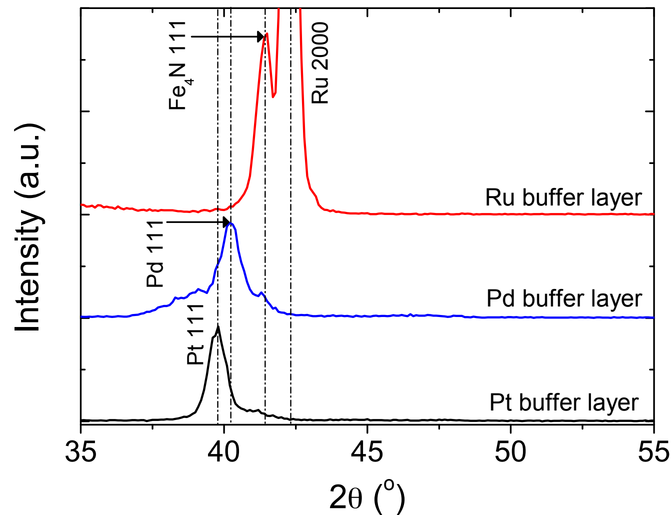

Figure 4.4 Out-of-plane X-ray diffraction patterns of 40nm Fe_4N thin films deposited on thermally oxidized Si substrates with Ru, Pd and Pt buffer layers.

4.3 Spin polarization measurement of Fe_4N (111)

To further investigate the transport spin polarization of (111) oriented Fe_4N, we perform point contact Andreev reflection (PCAR) measurements on samples with optimized growth conditions. A superconducting (Nb) tip is gently pressed into the sample to minimize the effect of surface oxidation. At least eight such different contacts are created and tested at a temperature of 1.6K. Figure 4.5(a) shows normalized conductance $G(V) / G_n$ versus V / V_Δ, in which G_n is the conductance at applied voltage $V >> V_\Delta$ and V_Δ is the superconducting gap of Nb. The PCAR experimental curves are fitted by a modified[85] Blonder-Tinkham-Klapwijk (BTK) model[86] with the spin polarization, P, and tunnel barrier strength, Z, as the fitting parameters. The superconducting gap, Δ, is fixed to the value for Nb. For comparison, the same measurement is made on a 40nm Fe (001) sample deposited on a GaAs (001) substrate. It appears that the spin polarization of (111) oriented Fe_4N ($P_{\mathrm{Fe4N}} = 0.5$) is statistically larger than that of (001) Fe ($P_{\mathrm{Fe}} = 0.44$), as shown in the inset of Figure 4.5(a). Compared to the Fe_4N deposited on MgO single crystal substrate ($P = 0.59$), our sample shows lower spin polarization, which can be partially attributed to the smaller in-plane grain size and the lower degree of crystallinity due to the fiber-textured growth mode of Fe_4N on the Ta/Ru under layer. Also, these samples deposited by sputtering tend to contain more defects than the samples prepared by molecular beam epitaxy (MBE). The defects increase the chance of spin-independent scattering for the electrons thus may also account for the lower spin polarization of our experiment..

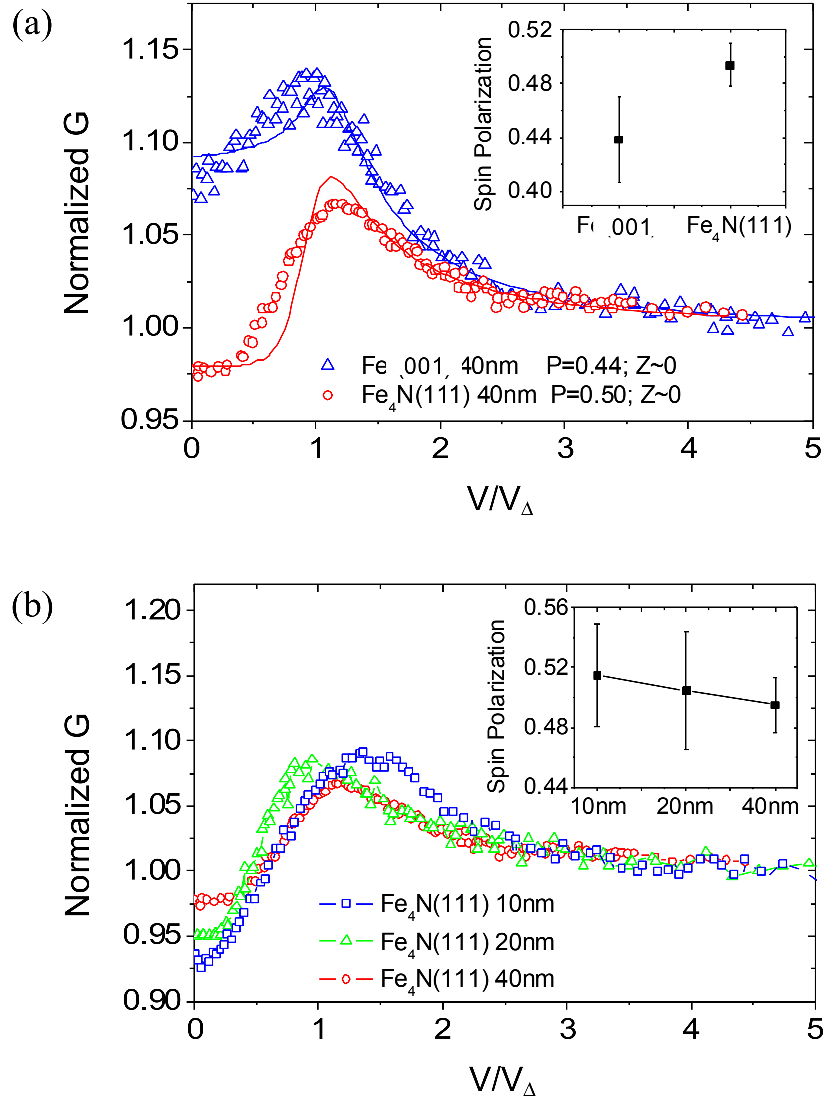

Figure 4.5 Point contact Andreev reflection results: Normalized conductance as a function of applied voltage (V) divided by superconducting gap (V_Δ) (a) For (111) oriented Fe_4N and Fe (001); (b) For (111) Fe_4N with different film thicknesses. Experiment data are shown in dots, and fittings are shown in continuous curves.

Although smaller spin polarization was observed, our work does show some advantages compared to the earlier report. First of all, our Fe_4N stack with Ta/Ru under layer is applicable for a group of spintronics devices, for examples MTJ/GMR and spin pumping

devices. The spin polarization of Fe_4N in the stack may better represent the properties of Fe_4N in the devices for applications. Furthermore, the Fe_4N film thickness in our report is in a few tens of nanometers, which is closer to the ferromagnetic layer thickness in the spintronics devices. Due to the above two benefits, our spin polarization result of Fe_4N is more practical than the pure material studies. In addition, the spin polarization in this work was reported as a mean of at least eight PCAR measurements for each sample. The averaging of measurements help minimize the testing variations thus make the results more reliable.

The spin polarization of (111) oriented Fe_4N with different film thicknesses is also studied, as shown in Figure 4.5(b). The PCAR measurements and fits are performed on the 10nm, 20nm and 40nm (111) Fe_4N thin films. To present the individual measurement curves clearly, the fits are not shown in this figure. As shown in the inset of Figure 4.5(b), the (111) oriented Fe_4N samples with smaller thickness (i.e. 10nm, 20nm) do not show a statistical difference from the 40nm Fe_4N sample. On average, the spin polarizations of the three samples are around 0.5 with minor variations. In Figure 4.6(b), the surface roughness of the 10nm (111) Fe_4N sample was measured by atomic force microscopy, showing a R_a of 0.153nm. It appears that our (111) Fe_4N thin film prepared at 250°C has a relatively smooth surface, which is essential for spintronics device integration.

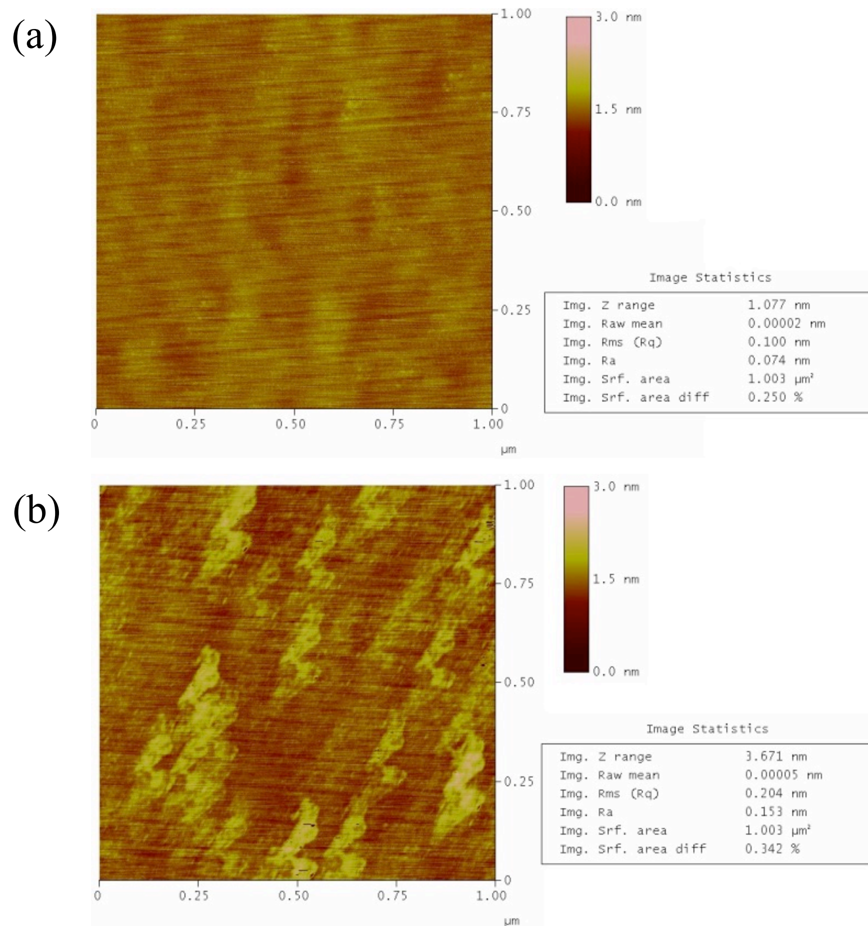

Figure 4.6 AFM image of Si wafer with (a) Thermal oxide (100nm) / Fe_4N (10nm), and (b) Thermal oxide (100nm) / Ta (2nm) / Ru (18nm) / Fe_4N (10nm)

Finally, we perform an X-ray photoelectron spectroscopy (XPS) measurement on the optimized (111) Fe_4N thin film. In Figure 4.7, Fe 2p3/2, Fe 2p1/2, and N 1s peaks are observed in the XPS result. By calculating the areas under these peaks and normalizing them to their sensitive factors, the N/Fe atomic ratio of 0.22±0.025 is obtained. This result indicates that the optimized (111) Fe_4N sample is close to stoichiometric. In addition, we perform a high resolution scan for the N 1s peak after carbon energy calibration. The N 1s binding energy of the sample is measured to be 397.6eV, which is

comparable to the result of $Fe_{16}N_2$[105]. Compared to the binding energy of N free radical (400eV), the large shift of N 1s peak in Fe_4N indicates electrons transfer from N to Fe, which may give us hints on the large spin polarization of Fe_4N.

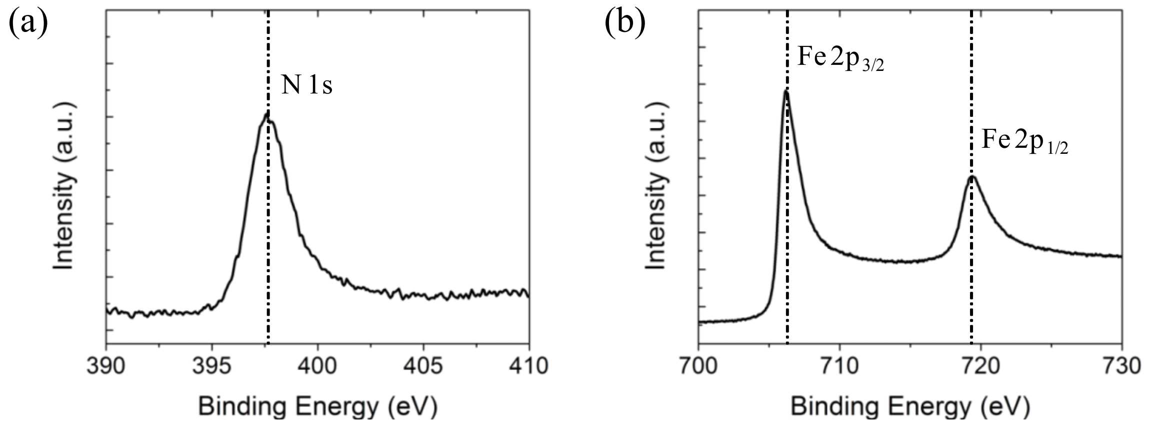

Figure 4.7 X-ray photoelectron spectroscopy spectra on (111) Fe_4N sample. (a) Fine scan on N 1s peak; (b) Fe $2p_{3/2}$ and Fe $2p_{1/2}$ peaks.

4.4 Summary

In conclusion, (111) oriented Fe_4N thin films are prepared on thermally oxidized Si wafers by facing-target-sputtering. A Ta/Ru composite buffer layer is used to induce the (111) out-of-plane orientation. The N_2 partial pressure and substrate temperature are optimized to facilitate Fe_4N phase formation. Furthermore, point contact Andreev reflection (PCAR) measurements and fits are performed on the (111) oriented Fe_4N. The transport spin polarization is found to be 0.50, which is larger than that of (001) Fe. The

spin polarization of (111) oriented Fe_4N measured by PCAR does not show degradation as the sample thickness approaches 10nm.

Chapter 5 Fe_4N based CPP GMR devices with giant inverse magnetoresistance

In this chapter, I will introduce my works on the damping constant (α) measurement of Fe_4N and the Fe_4N based giant inverse magnetoresistance device. Fe_4N (001) thin films have been prepared on Fe/Ag underlayers. The damping constant of the Fe_4N (001) is measured by the ferromagnetic resonance using coplanar waveguides and microwave excitation. The CPP GMR with Fe_4N/Ag/Fe sandwich is fabricated and characterized. Giant inverse magnetoresistance is observed in the CPP GMR device, which proves the negative spin polarization of Fe_4N and Fe_4N/Ag interface.

5.1 Introduction

In previous chapter, I have prepared the Fe_4N thin film in a single source facing-target-sputtering system. Spin polarization study has been done on the Fe_4N thin film, which shows its potential in spintronics application. Based on above results, it would be quite intriguing to further incorporate Fe_4N in a magnetoresistive device, as the negative spin polarization of Fe_4N may provides a pathway for a group of novel spintronic logic devices, and the magnetoresistive device is an important building block. In previous studies by Komasaki, Y et al., tunneling magnetoresistive device with Fe_4N

ferromagnetic layer has been demonstrated. There is no existing study on Fe_4N CPP GMR. With our home-built multi sources facing-target-sputtering system, Fe_4N GMR thin film stack can be prepared in the same sputtering chamber without vacuum break. It ensures high quality interfaces of the GMR stack, which is critical for magnetoresistive devices.

Recently, the current induced magnetization switching has been realized in Fe_4N based magnetic tunnel junctions[1]. According to Slonczewski's spin transfer torque (STT) model[49], the critical switching current densities of TMR/GMR devices are proportional to the damping constants of the magnetic free layers. Thus it is also of great interest to study the damping constant (α) of Fe_4N to understand its limitation for STT induced magnetization switching. Until now, only a few articles have reported the damping constant of Fe_4N[111,112]. Those results are subject to strong spin pumping effect which tends to overestimate the damping constant.

Since the entire CPP GMR stack need to be deposited in the multi sources facing-target-sputtering system with three pairs of sputtering targets, the Fe_4N deposited on Ta/Ru buffer layer shown in previous chapter may not be appropriate for the stack, as both Ta and Ru cannot work as the spacer in CPP GMR. Therefore, I developed a new recipe to prepare (001) Fe_4N thin film in the multi sources facing-target-sputtering system. A Fe(001)/Ag(001) composite buffer layer is selected to promote the (001) orientation of the Fe_4N thin film. The Ag layer in contact with Fe_4N works natively as the bottom electrode for tunneling/giant magnetoresistive devices. Moreover, the ferromagnetic resonance (FMR) of the Fe_4N (001) thin film has been measured using coplanar

waveguides and microwave excitation. Due to the weak spin pumping effect of Ag[113], the stack structure does not artificially increase the effective damping of the Fe_4N (001) thin film. I have also fabricated and characterized the current-perpendicular-to-plane (CPP) giant magnetoresistance (GMR) device with Fe_4N/Ag/Fe sandwich. Giant inverse magnetoresistance is observed in the CPP GMR device, which suggests that the spin polarization of Fe_4N and Fe_4N/Ag interface is negative.

5.2 Fe_4N (001) thin films deposited on Ag under layers

Fe_4N multilayer stacks with a structure of MgO(001)/Fe(5nm)/Ag(35nm)/Fe_4N(17nm)/Ru(5nm) are prepared. The base pressure of the sputtering chamber is lower than 4.0×10^{-8} Torr. During the multilayer stack preparation, the Fe/Ag bilayer is first grown onto a MgO (001) single crystal substrate at room temperature. Thereafter, the substrate is heated to 285°C and the Fe_4N thin film is deposited by reactive sputtering in a Ar and N_2 gases mixture. To obtain stoichiometric Fe_4N thin films, the N_2 partial pressure varies from 0.35 mTorr to 0.6 mTorr while the total gas pressure is maintained at 2.5 mTorr during the sputtering process. The Ru capping layer is then deposited on top of the Fe_4N layer. After optimizing the grown conditions of the Fe_4N thin film, stacks of MgO substrate/Fe(5)/Ag(50)/Fe_4N(7)/Ag(5)/Fe(7)/Ag(5)/Ru(8) (nm) are deposited for the CPP GMR nanoscale devices fabrication.

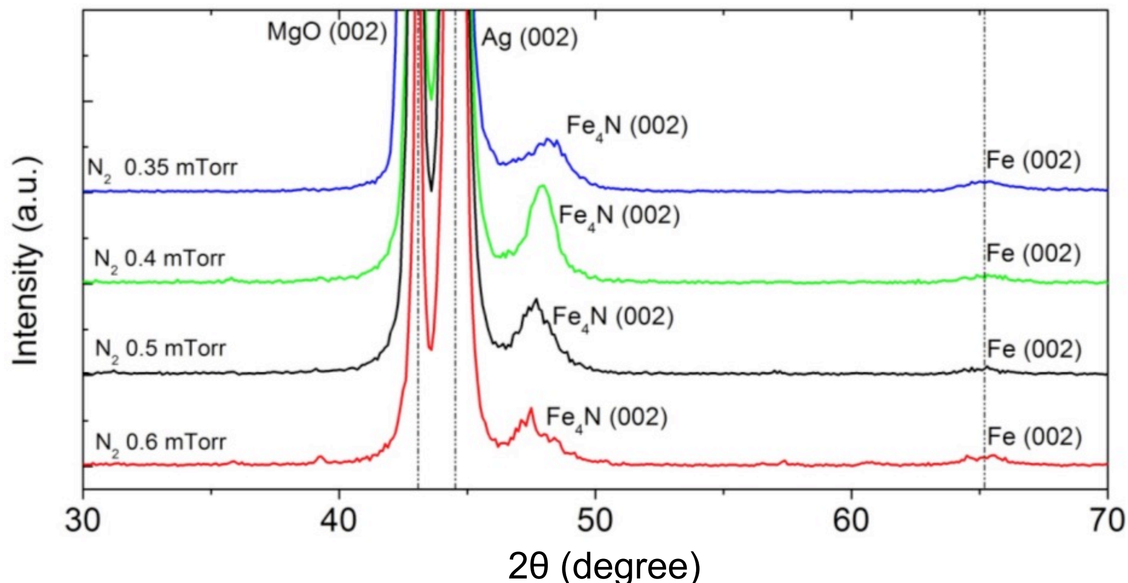

Figure 5.1 XRD θ-2θ scans of the 17nm Fe-N thin films deposited with different N2 partial pressures. The Fe(002) diffraction signals are from the Fe buffer layer.

In order to characterize the Fe_4N phase and out-of-plane crystal orientations, θ-2θ X-ray diffraction (XRD) measurements are performed on a Simens Bruker D5005 system with Cu Kα radiation. The rocking curves of the Fe_4N thin films are measured by a Panalytical X'Pert Pro System. X-ray photoelectron spectroscopy (XPS) is performed on a Surface Science SSX-100 system to further confirm the stoichiometry. The surface roughness is characterized by an Agilent 5500 atomic force microscope (AFM). Magnetic properties of the samples are examined by a Princeton Measurements vibrating sample magnetometer (VSM).

Figure 5.1 shows the out-of-plane X-ray diffraction (XRD) patterns of Fe-N thin films deposited on Fe(001)/Ag(001) under-layers. Fe_4N has the face-centered-cubic Fe lattice

with N atom located at the body center. The in-plane lattice constants of Fe_4N and Ag are 3.795Å and 4.079Å respectively, thus there is a 7% lattice mismatch between the Fe_4N [001] and Ag [001] planes. Based on the Fe-N phase diagram, several iron nitride compounds can be formed with different Fe:N compositions, therefore the N_2 partial pressure during sputtering needs to be optimized. As the N_2 partial pressure is gradually tuned from 0.35 mTorr to 0.6 mTorr, the nitrogen composition increases continuously in the Fe-N thin films. In Figure 5.1, Fe_4N (002) diffraction peaks can be observed for all the growth conditions, because the high substrate temperature promotes the formation of Fe_4N phase. The Fe_4N (001) diffraction peak is absent in our samples due to the small film thickness. When the N_2 sputtering partial pressures are 0.5 mTorr and 0.6 mTorr, besides the Fe_4N (002) peak, two small peaks of Fe_3N near 39.2° and 57.5° are present in the XRD pattern, which indicates that the N:Fe atomic ratio is larger than 1:4. As we decrease the N_2 partial pressure to 0.4 mTorr, the peaks of Fe_3N disappear, and the Fe_4N (002) peak becomes very pronounced. When we further decrease the N_2 partial pressure to 0.35 mTorr, the intensity of the Fe_4N (002) peak is weaker, and the Fe (002) peak appears. Therefore we conclude that the 0.4 mTorr N_2 partial pressure is the optimized condition for the growth of Fe_4N thin films. In our experiment, the substrate temperature is maintained at 285°C for all the growth conditions. The substrate temperature cannot be further increased in the deposition process due to the limitation of the sputtering system. Alternatively, we post-annealed the optimized sample at 325°C in a different vacuum chamber. No noticeable change is seen in the XRD result of the annealed sample.

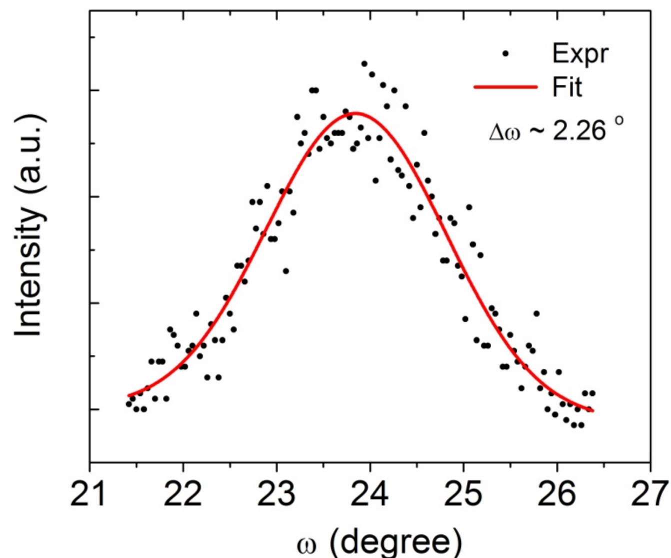

Figure 5.2 The rocking curve measured on Fe_4N (002) peak of the sample with 0.4 mTorr N_2 partial pressure.

The rocking curve is measured on the Fe_4N (002) diffraction peak of the optimized sample, as shown in Figure 5.2. Considering that the Fe_4N layer is as thin as 17nm, the FWHM ($\Delta\omega$=2.26°) of the rocking curve indicates that the film has strong (001) out-of-plane orientation.

In order to confirm the stoichiometry of the Fe_4N thin film, we perform X-ray photoelectron spectroscopy (XPS) measurement on the optimized Fe_4N sample. In Figure 5.3, Fe 2p3/2, Fe 2p1/2, and N 1s peaks are presented in the XPS spectrum. By integrating the areas under these peaks and dividing them by their sensitive factors, the N/Fe atomic ratio of 0.22±0.025 is obtained. This result indicates that the Fe_4N thin film with 0.4 mTorr N_2 sputtering partial pressure is nearly stoichiometric.

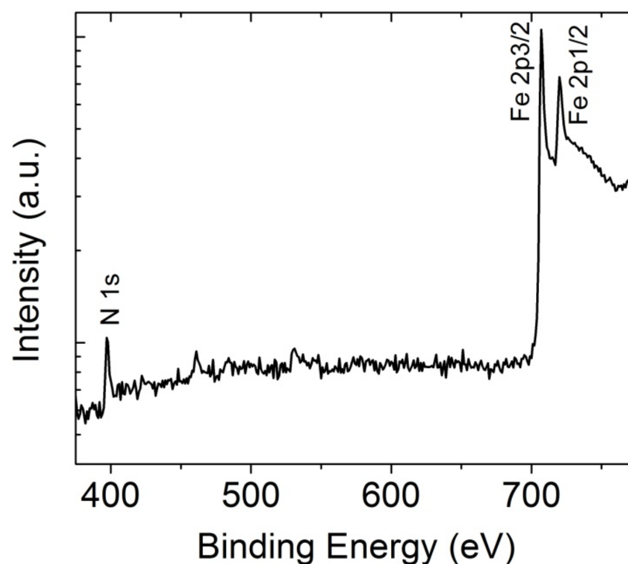

Figure 5.3 The XPS spectrum of the Fe_4N sample with 0.4 mTorr N_2 partial pressure.

To control the spin-independent scattering in magnetoresistive devices, the surface roughness of the magnetic layers needs to be minimized. We measure the surface roughness of the optimized Fe_4N sample by atomic force microscope (AFM). The *RMS* roughness of the as-deposited Fe_4N thin film is 0.75nm. We subsequently post-anneal the sample at 325°C for 2 hours in a vacuum chamber. The *RMS* roughness of the post-annealed Fe_4N thin film is reduced significantly to 0.34nm. As mentioned above, the intensity of the Fe (002) XRD peak does not show noticeable change after we annealed the sample. The saturation magnetization of the post-annealed Fe_4N sample is measured to be 1050 emu/cm^3 by vibrating sample magnetometry.

5.3 Damping constant measurement of Fe_4N (001) thin films

In order to measure the ferromagnetic resonance (FMR) of the Fe_4N (001) thin film, the 5nm Fe underlayer needs to be excluded from the stack to prevent the interference of FMR signal. We initially tried to deposit MgO substrate/Ag/ Fe_4N samples without the Fe underlayer, but both the film adhesion and crystal quality of the samples are poor. It has been reported that Fe_4N (001) thin films can be grown epitaxially on MgO substrates[2], though the lattice mismatch between Fe_4N and MgO is as large as 9.6%. Therefore, we deposit thin film stacks with the structure of MgO substrate/Fe_4N 17/Ag 17/Ru 5 (nm) and pattern the sample into micrometer scale coplanar waveguides for the magnetization excitation. The details of coplanar waveguides and magnetization excitation methods are discussed in our previous publication[114].

Next, we measure the ferromagnetic resonance (FMR) of the Fe_4N thin film. The radio frequency (RF) signals are injected into the waveguides, and the resonance field of the magnetization excitation is measured. The frequency of the RF signal ranges from 4GHz to 17GHz. The excitation frequency versus the resonance field relationship matches well with the Kittel formula $f = \frac{\gamma}{2\pi}\sqrt{H(H+M_s)}$, as shown in Figure 5.4. By the curve fitting, we extract the saturation magnetization to be ~1000 emu/cc, which is consistent with the vibrating sample magnetometry measurement results. The gyromagnetic ratio γ is fitted to be 2.88×10^5rad/(A/m). The Gilbert damping constant of Fe_4N is calculated from $\alpha = \frac{\sqrt{3}\gamma\Delta H}{2\omega}$, and it is found to be about α = 0.019 for the excitation frequency of 16GHz. The damping constant of Fe_4N deduced from the full excitation frequency range is α =

0.021±0.02. As mentioned in the introduction of this chapter, since the Ag in contact with Fe_4N is known to have a small spin pumping effect, the damping constant of Fe_4N measured in our sample is expected to be closer to the intrinsic number than the previous report.

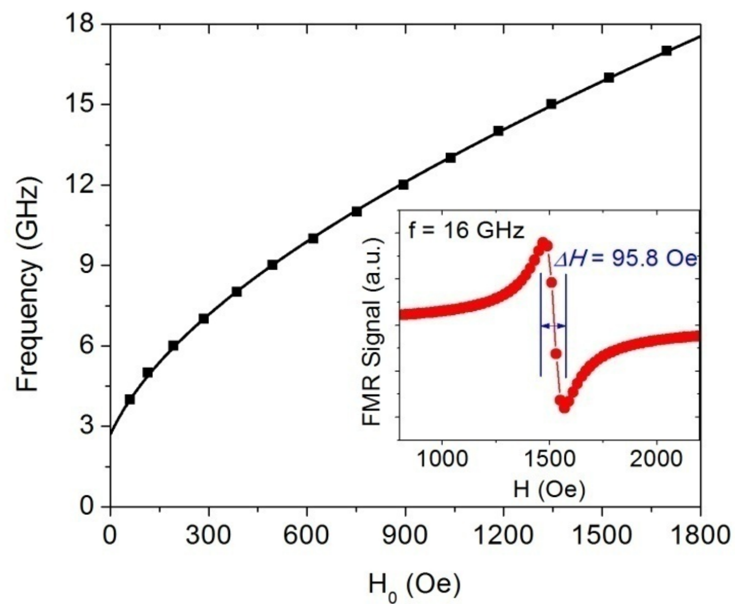

Figure 5.4 The resonant magnetic fields for different excitation frequencies which are overlaid with the Kittle formula curve fitting. The inset shows the FMR line width of Fe4N (001) thin film measured at 16GHz.

5.4 Giant inverse magnetoresistance in Fe_4N/Ag/Fe

Based on the Fe_4N (001) thin films that we have developed, we further prepare current-perpendicular-to-plane (CPP) giant magnetoresistance (GMR) stacks with a multilayer

structure of MgO substrate/Fe(5)/Ag(50)/Fe_4N(7)/Ag(5)/Fe(7)/Ag(5)/Ru(8) (thickness in nm), as seen in Figure 5.5. A reference multilayer stack is also prepared by replacing the Fe_4N (7nm) layer with another Fe (7nm) layer. These two samples are subsequently fabricated into ~100nm nanopillar devices by electron beam lithography and Ar^+ ion beam etching combined processes. The lateral dimensions of the elliptical nanopillars are $160 \times 100nm^2$ and $140 \times 100nm^2$ respectively for the CPP GMR devices with Fe_4N/Ag/Fe and Fe/Ag/Fe sandwiches. Both the Fe_4N and the Fe layers of the as-fabricated devices have their easy magnetic axis along in-plane long axes of the ellipses. Giant magnetoresistance signals of the devices are measured by a four-point-probe method.

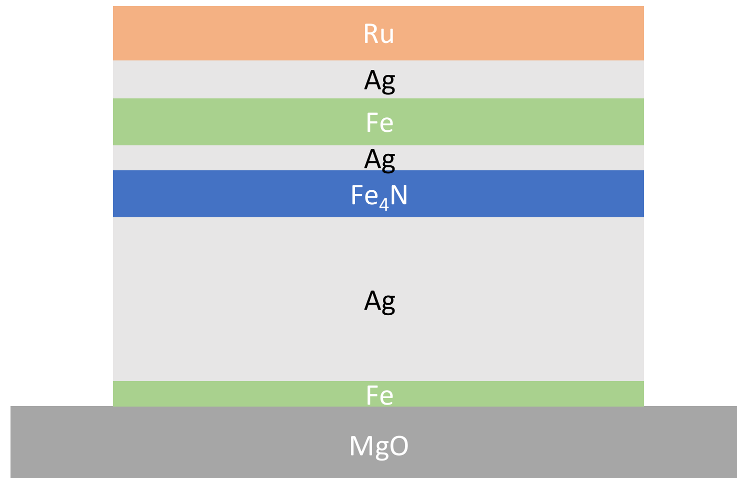

Figure 5.5 Schematic drawing of Fe_4N/Ag/Fe GMR stack

The ΔR-H loops of Fe_4N/Ag/Fe CPP GMR and Fe/Ag/Fe CPP GMR are given in Figure 5.6 (a) and Figure 5.6 (b) respectively. Since there is no pinned magnetic layer in both the CPP GMR devices, the magnetizations of the two magnetic layers are anti-parallel

coupled by dipolar magnetic interactions in remanence states. When a relatively large magnetic field is applied along the long axis of the nanoscale ellipses, the two magnetic layers are parallel aligned by the external field. Figure 5.6 (a) shows that the Fe_4N/Ag/Fe CPP GMR device has lower resistance in the anti-parallel state and higher resistance in the parallel state, namely the giant inverse magnetoresistance is observed. This behavior is quite different from the typical giant magnetoresistance which presents in the CPP GMR devices with the same ferromagnetic free and fixed layers, as seen in the Fe/Ag/Fe CPP GMR device in Figure 5.6 (b). We attribute this unique giant inverse magnetoresistance behavior to the negative spin polarization of Fe_4N and the negative spin scattering asymmetry at the Fe_4N/Ag interface.

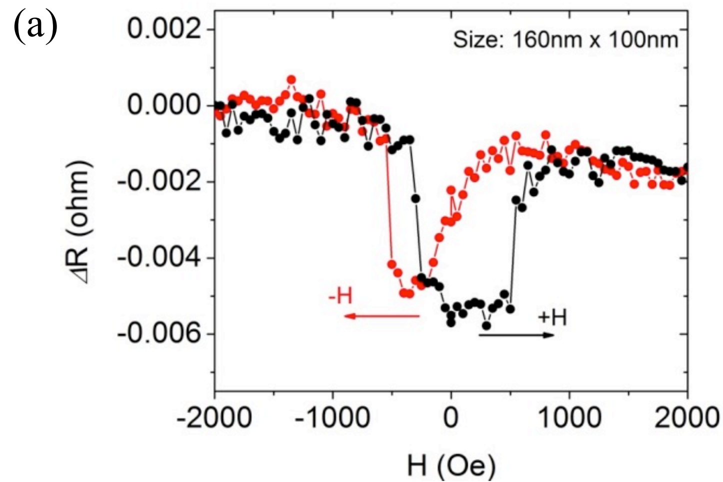

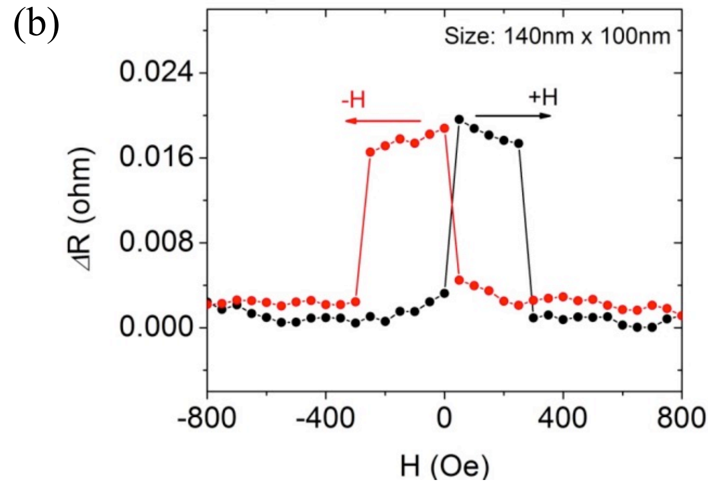

Figure 5.6 Giant magnetoresistance signal of (a)Fe4N/Ag/Fe CPP GMR; (b)Fe/Ag/Fe CPP GMR as a function of in-plane magnetic field

5.5 Summary

Fe_4N (001) thin films are prepared on Fe(001)/Ag(001) buffer layers by facing-target-sputtering. The N_2 partial pressure during sputtering is optimized to promote the formation of Fe_4N phase. The nearly stoichiometric Fe_4N thin film is confirmed by XPS measurement. The surface flatness of the Fe_4N thin film is significantly improved by a post-annealing process. Furthermore, the Gilbert damping constant (α) of the Fe_4N (001) thin film in contact with Ag is measured by ferromagnetic resonance and is extracted from the damping-linewidth relationship. The α_{Fe4N} is determined to be 0.021±0.02. Giant inverse magnetoresistance is observed in the Fe_4N/Ag/Fe CPP GMR device. This unique

magnetoresistance behavior can be explained by the negative spin polarization of Fe_4N and the negative spin scattering asymmetry at Fe_4N/Ag interface.

Chapter 6 Conclusions and Outlook

In this thesis, I have shown the experimental studies of the material properties and the spintronic devices based on two iron nitride materials, i.e. $Fe_{16}N_2$ and Fe_4N.

In the $Fe_{16}N_2$ material studies and magnetoresistance device development, I have demonstrated a perpendicular material system that can be integrated into high density spintronic devices. Based on the heavy-metal-free, low damping and crystalline perpendicular anisotropy properties of $Fe_{16}N_2$, a current-perpendicular-to-plane (CPP) giant magnetoresistance (GMR) device with perpendicular $Fe_{16}N_2$ magnetic layers has been fabricated. The crystalline based perpendicular anisotropy of the $Fe_{16}N_2$ in the device has been measured, and the anisotropy constant of $Fe_{16}N_2$ as large as 1.9×10^7 erg/cm^3 is confirmed by a first principle calculation. We showed that the thermal stability of this material system is sufficient to support the perpendicular spintronic device with sub-10nm dimension. Moreover, due to the absence of heavy metal in $Fe_{16}N_2$, the damping constant of $Fe_{16}N_2$ is measured to be 0.01, which is much lower than the current crystalline based perpendicular materials. These advantages of $Fe_{16}N_2$ facilitate low power consumption in spin based logic and memory device thus offer a pathway for future spintronic applications.

In the spin polarization study of (111) oriented Fe_4N thin film, I started from the Fe_4N thin film preparation and optimization on thermally oxidized Si substrate. The buffer layer, N:Fe composition, and substrate temperature during sputtering are tuned to

promote the formation of the Fe_4N phase and to induced the (111) out-of-plane orientation. The transport spin polarization of the (111) oriented Fe_4N is found to be 0.50 for the Fe_4N thin film deposited on thermal oxide with buffer layer. The thickness dependence of the spin polarization is also studied. The spin polarization of (111) oriented Fe_4N measured by PCAR does not show degradation as the sample thickness approaches 10nm.

In the development of Fe_4N based CPP GMR device, I first prepare the (001) oriented Fe_4N thin films on Fe/Ag underlayers. The damping constant of the (001) Fe_4N is measured by the ferromagnetic resonance using coplanar waveguides and microwave excitation. The α_{Fe4N} is determined to be 0.021±0.02 by the damping-linewidth relationship. The CPP GMR incorporating Fe_4N is fabricated, and it demonstrates the giant inverse magnetoresistance. This unique magnetoresistance behavior is explained by the negative spin polarization of Fe_4N and the negative spin scattering asymmetry at Fe_4N/Ag interface.

For future research directions, to address the small magnetoresistance ratio of the $Fe_{16}N_2$ CPP GMR, magnetic tunneling junctions (MTJ) incorporating $Fe_{16}N_2$ and MgO barrier is recommended to study. To deposit the thin film stack of $Fe_{16}N_2$ MTJ, the multi source facing target system needs to be modified by adding a process chamber with RF sputtering source. The $Fe_{16}N_2$/MgO interface may need to be engineered in term of electron band matching.

Appendix A: Perpendicular multi-bit magnetic tunnel junctions

In Appendix A, I will show my work on developing multi-bit MTJs based on $[Co/Pd]_n$ multilayer and ultra-thin MgO/CoFeB/Ta/CoFeB/MgO perpendicular material systems. The multi-bit MTJ thin film stacks are deposited in a six-target conventional sputtering system. Multi-bit MTJ devices are fabricated by photolithography and Ar+ ion beam etching combined processes. The TMR results are measured by a four point probe tester.

1. Developing $[Co/Pd]_n$ multilayer for perpendicular multi-bit MTJs

The $[Co/Pd]_n$ multilayer is a robust material system for perpendicular MTJs. By adjusting the thickness of Co and Pd sub layers, the coercivity of $[Co/Pd]_n$ multilayer can be tuned in a wide range (300Oe to 3000Oe). Thus the $[Co/Pd]_n$ multilayer can be adopted as both free and fixed layers of the multi-bit MTJs. Furthermore, the $[Co/Pd]_n$ multilayer has a small damping constant α, since this material system does not contain any heavy metal elements. Small damping can result in a low current density for spin transfer torque switching. Due to the above advantages, we choose the $[Co/Pd]_n$ multilayer as the bottom fixed layer and the top free layer of the multi-bit MTJ stacks.

To develop the bottom fixed layer, $[Co\ 0.4/Pd\ 0.7]_5$ multilayers are deposited on Ta 5/Pd 10 (nm) and Ta 5/Pd 5/Ta 5/Pd 10 (nm) buffer layers respectively. Both samples show

strong perpendicular magnetic anisotropy. The [Co 0.4/Pd 0.7]$_5$ multilayer deposited on Ta 5/Pd 10 (nm) has sharper field switching profile than the sample deposited on Ta 5/Pd 5/Ta 5/Pd 10 (nm), which is likely caused by their different film roughness, as shown in Fig. 7.1(a). The sharper switching field ensures cleaner TMR signal, therefore the Ta 5/Pd 10 (nm) is chosen as the buffer layer for the multi-bit MTJ stacks.

In order to control the coercivity of the top free layer, we fix the Pd sub-layer thickness and vary the thickness of the Co layer. The coercivity of [Co X/Pd 0.7]$_5$ multilayer increases from 500Oe to 2500Oe as the Co layer thickness is reduce from 0.4nm to 0.3nm, as shown in Fig. 7.1(b).

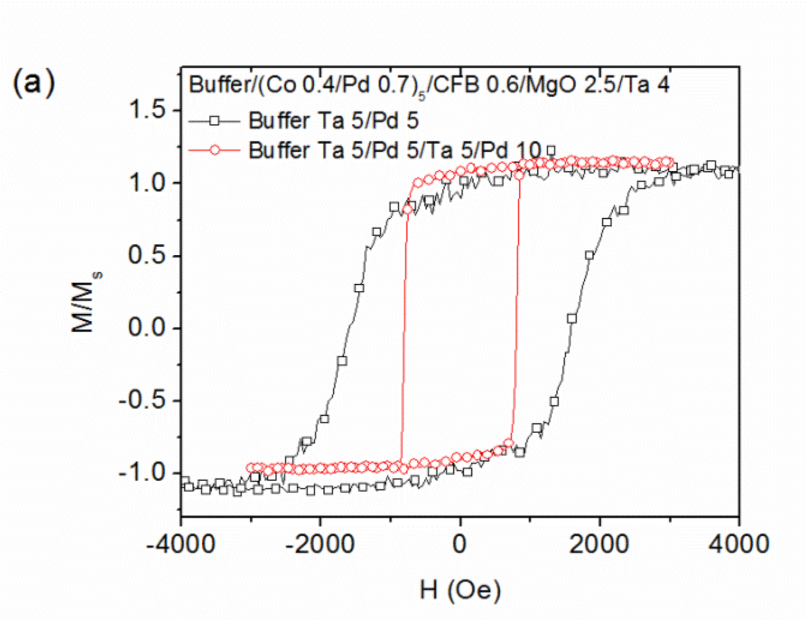

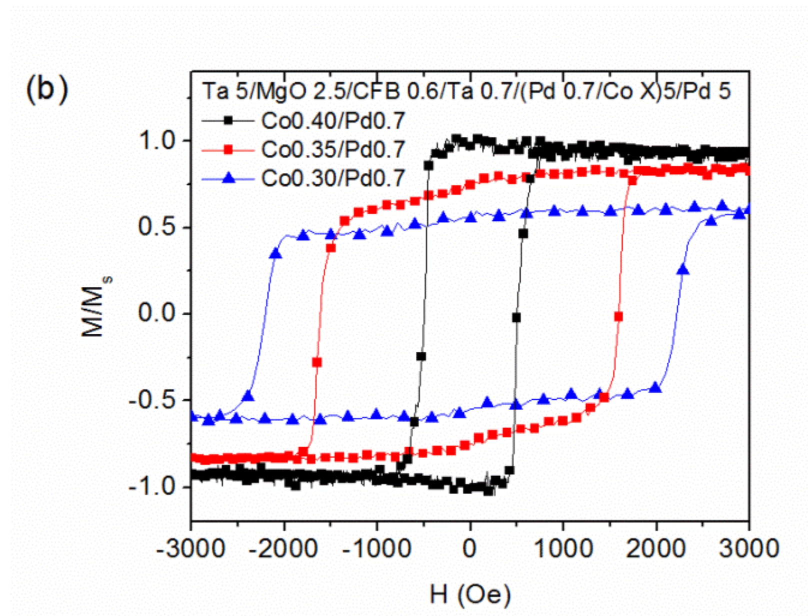

Figure 7.1 Perpendicular hysteresis loops of [Co/Pd]n multilayer (a) for bottom fixed layer; (b) for top free layer.

2. Developing MgO/CoFeB/Ta/CoFeB/MgO composite layers for multi-bit MTJs

Recently, MgO/CoFeB/Ta/CoFeB/MgO perpendicular system has been developed to increase the thermal stability of interface PMA CoFeB. Since the magnetic layers are sandwiched by MgO tunneling barrier, this material system is suitable for the middle free layer of multi-bit MTJs. We fine tuned the thickness of CoFeB layers in this system to control the perpendicular magnetic anisotropy of the composite layers. In addition, all the samples are post-annealed at 200°C for 2 hours to enhance the perpendicular anisotrypy.

Fig. 7.2 shows that the MgO/CoFeB/Ta/CoFeB/MgO composite structure is fully perpendicular with 1.4-1.6 (nm) bottom CoFeB and 1.0-1.2 (nm) CoFeB on the top.

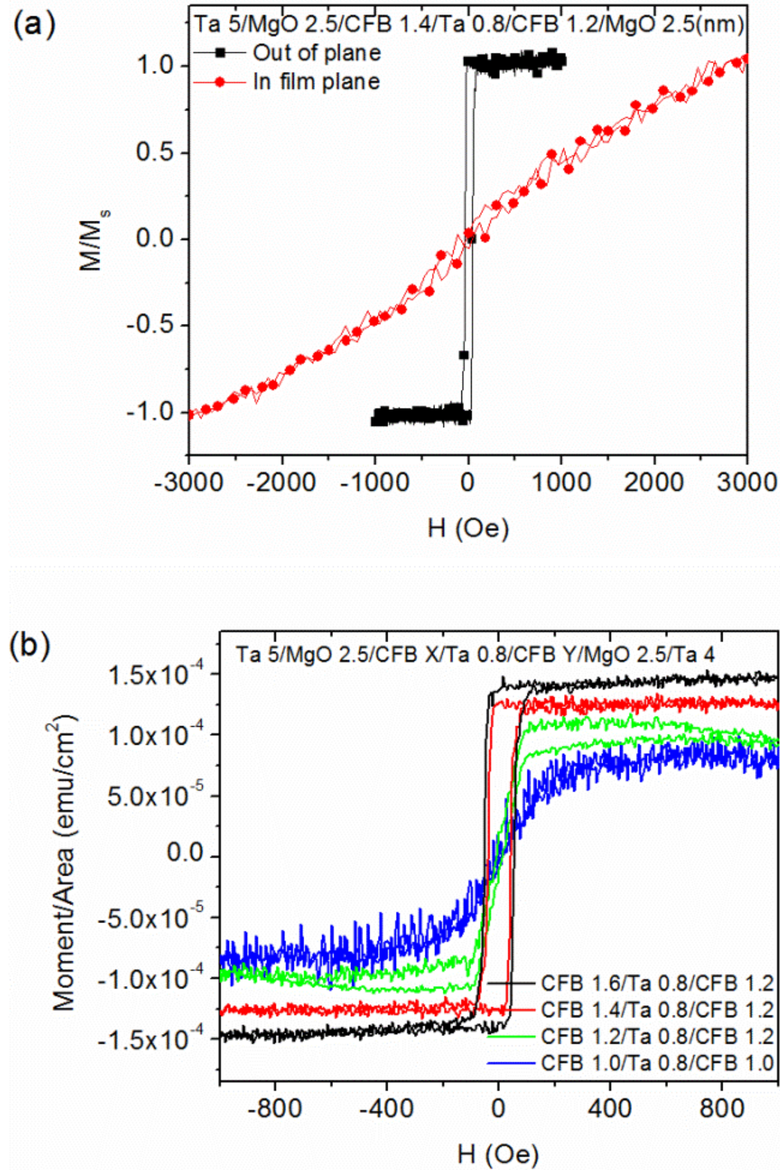

Figure 7.2 Hysteresis loops of MgO/CoFeB/Ta/CoFeB/MgO composite structure for middle free layer.

3. Multi-bit Perpendicular MTJ stacks

After the multi-bit building blocks of the individual magnetic layers are successfully developed, we combine those layers into a complete multi-bit perpendicular MTJ stack, as illustrated in Fig. 7.3. In a combined multi-bit stack, the film roughness accumulates from the lower layers to the upper layers. Thus the middle and upper free layers in the full stacks are more susceptible to the film roughness than those stand alone free layers. Consequently, the magnetic properties of the combined stack could be influenced by this additional roughness.

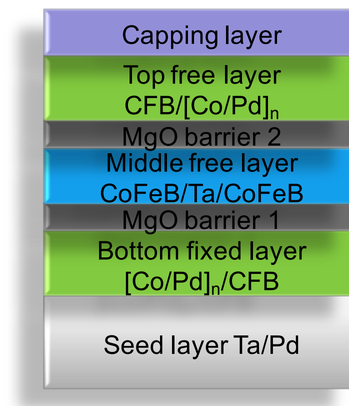

Figure 7.3 Schematics of a designed multi-bit perpendicular MTJ stack

Fig. 7.4 shows the M-H loops of two multi-bit MTJ stacks that we have studied. Clear three steps switchings are observed in the hysteresis loops of both stacks. The switching fields of the magnetic layers are well seperated. As the magetic field sweeps from positive to negative direction, the first, second and third switching steps correspond to the switching of middle free layer, top free layer and bottom fixed layer respectively.

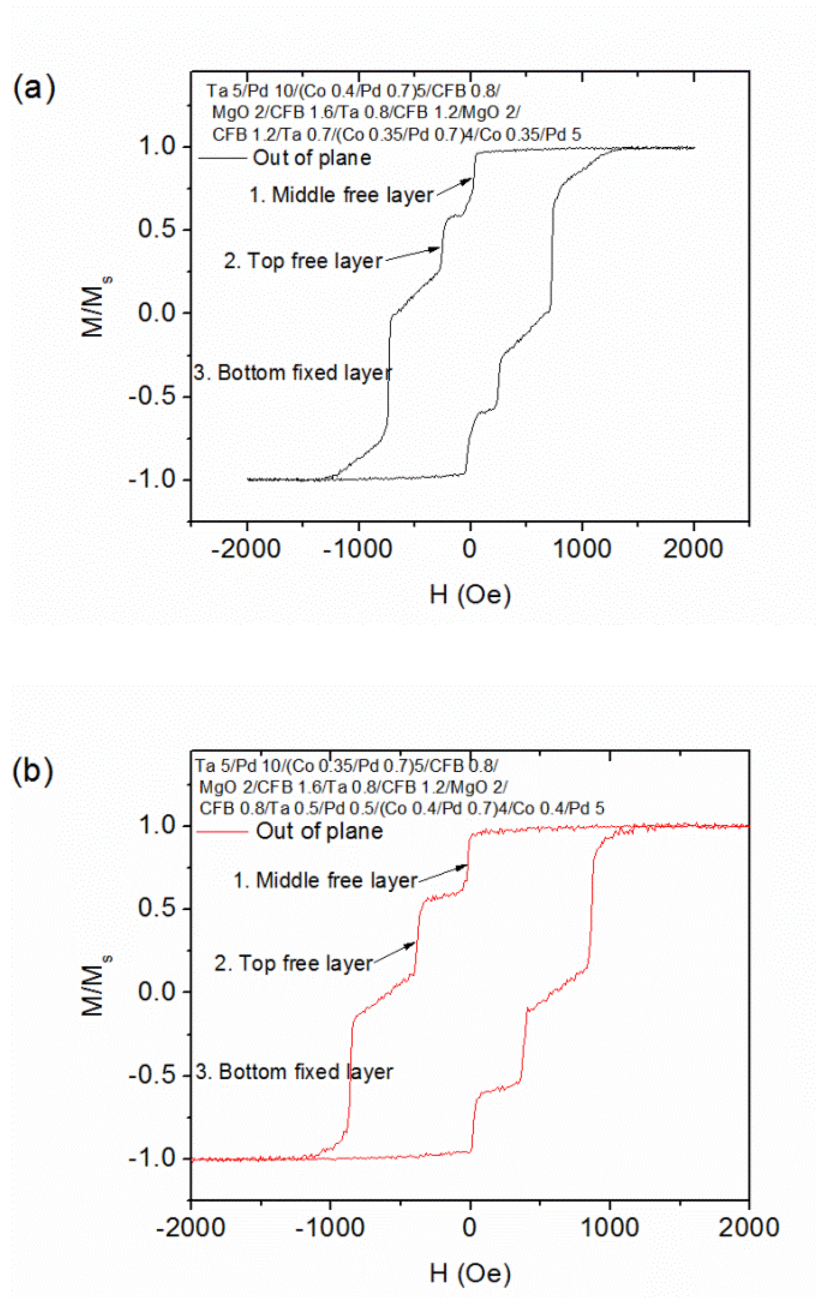

Figure 7.4 M-H loops of Multi-bit MTJ stacks measured by VSM

4. Multi-bit Perpendicular MTJs fabrication and TMR testing

The multi-bit perpendicular MTJ stacks are fabricated into micron size elliptical pillars devices by photolithography and Ar ion etching combined processes. The room temperature TMR signal of the device is measured. As shown in Fig. 7.5, the TMR signal of the perpendicular MTJ device is up to 7%. However, only two steps switching is observed in the R-H loops, which is quite different from the three steps switching that we obtain previously from the M-H measurement.

We attribute the absence of three steps switching in R-H loops to the leakage of MgO barrier 2. It has been mentioned that the thin film layers close to the top surface may have larger roughness than the lower layers. The extra roughness may introduce pin holes in the MgO barrier 2. As a result, the MgO barrier 2 and its adjacent magnetic layers do not contribute enough TMR signal to the device. Therefore, the TMR signal that we observe in the R-H measurement could be only from the bottom fixed layer and the middle free layer.

The suggestion to the future work for improving the multi-bit stack and device would be increasing the thickness of the MgO barrier 2 to eliminate the pin holes. In addition, the device fabrication processes may need to be improved to prevent any current short circuits in the micron scale pillars. With these modifications, we expect that both magnetic signal and electrical signal can show the three steps switching in the future.

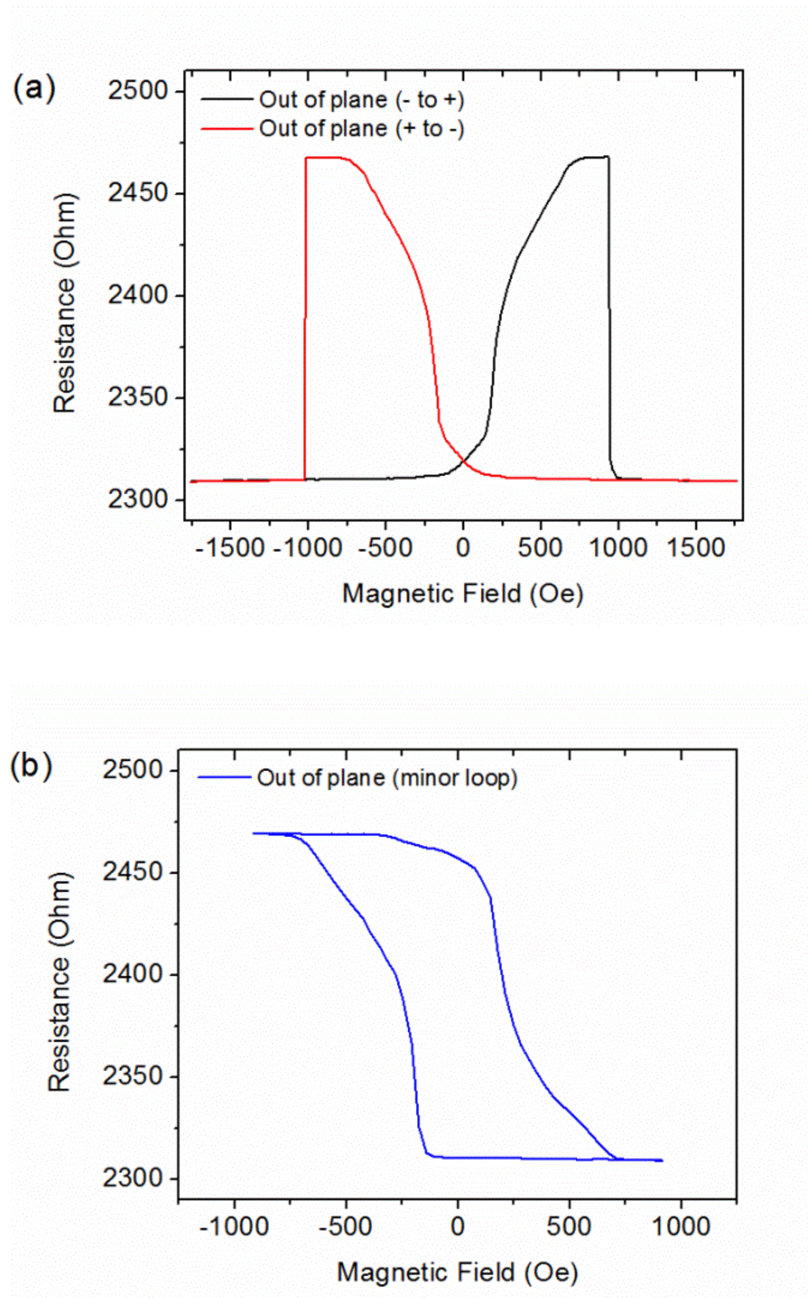

Figure 7.5 TMR signal of multi-bit MTJ device with stack structure Ta 5/Pd 10/(Co 0.35/Pd 0.7)5/CFB 0.8/MgO 2/CFB 1.6/Ta 0.8/CFB 1.2/MgO 2/CFB 0.8/Ta 0.5/Pd 0.5/(Co 0.4/Pd 0.7)4/Co 0.4/Pd 5

Appendix B: Sub-100nm CPP GMR fabrication Run Sheet

Wafer: 3" Si or 1"x1" MgO
Step 1: CPP GMR bottom electrode mask exposing. **Photo Resist Coating:** (PR 1813) Equipment: CEE Photo-resist Spinner Condition: □ Pre-bake 115°C for 1 minute □ Program 4: Coat PR1813 at 4000RPM 30 seconds (around 18000Å thick). □ Soft Bake 105°C for 1 minute **Mask exposing:** Equipment: KARL SUSS MA6 Condition: Program: Hard-Ct/cont. □ Time: 5.5 seconds, Distance 20 *u*m. **Photo Resist developing:** □ Solution: H_2O:351=5:1 (wet bench) Time= 30 sec □ Rinse tank, DI wafer rinse and N2 blow dry □ Hard Bake: 120 °C time=1 minute
Step 2: Bottom electrode definition. Equipment: Ion Mill II □ Conditions: Base pressure: 8×10^{-6} Torr, Etching pressure: 8×10^{-5} Torr. Beam voltage: 300V, Accelerate voltage: 500V, Current:9 mA. Angel: 60° (right column: angle between sample and beam is 90-60=30) Ration: 4RPM, Time: 40 minutes (depend on total bottom layer thickness).
Step 3: Photo Resist Removal. Solution: Acetone. Condition: Put Acetone into Ultrasonic(48%) for 10 minutes; DI water tank, DI water rinse, N2 blow dry □

Step 4: Deep sub-micron/Nano scale CPP GMR exposure.
Equipment: EBPG E-beam lithography

Conditions:

Ebeam resist coating: (MaN-2403)
Prebake: 170C for 15 minute.
HMDS 5 minutes.
Ebeam resist coating: NEB31 at 6000RPM for 1 minute.
Softbake: 110C for 2 minute.

Ebeam resist exposure:
Voltage=100kV, app=10um, current=1nA, dose= ~100 uC/cm2, align mark p20

Ebeam resist develop:
Hardbake: 95C for 4 minute
MF319 10 seconds
DI water rinse. Blow dry with N2.

Step 5: Deep sub-micron/Nano scale CPP GMR definition
Equipment: Ion Mill II
Conditions:
Base pressure: 8×10^{-6} Torr, Etching pressure: 8×10^{-5} Torr.
Beam voltage: 300V, Accelerate voltage: 100V, Current: 9 mA.
Ration: 4RPM
Angel: first 10° (3min etching + 3min stopping);
Change to 70° when reference sample gone for 3 min.

Calibration sample is needed to control the etching.

Comment: this step is very critical, make reference sample a little thicker than the pillar height (~5nm), to avoid the under milling happens.

Step 6: Insulator layer between bottom electrode and top electrode deposition (SiO_2)
Equipment: PECVD
□ Conditions: Load process “$SiO_2$150” (SiO_2- 150°C); then press “ready” to anneal
Deposition rate: 5.8787Å/sec
SiO_2 thickness= pillar +50Å

Step 7: lift-off (remove the photo resist and insulator layer).
Solution: Developer 1165
□ Condition: Heat set point at 70 ^{o}C for 2h+.

Put 1165 into Ultrasonic(**40%**) for 30min+ (1165 heated to 60 ^{o}C first).
Water tank; DI water rinse; N2 blow dry.
Check with Microscopes.

Comments: The time for 1165 Bath cannot be too long 3h 30min is fine, plus 2hr 45m is too long(1165 erode metal if too long).
Note: write down the heating time and Ultrasonic time

Step 8: Bottom electrode hole masks exposing.

Photo Resist Coating:

Equipment: CEE Photoresist Spinner
Condition:

- □ Pre-bake 115°C for 1 minute.
- □ Program 4: Coat PR1813 at 4000RPM 30 seconds (around 18000Å thick).
- □ Soft Bake 105°C for 1 minute

Comments: CEE **vacuum** test first!

Mask exposing:

Equipment: KARLSUSS MAB6
Condition: Program: Hard-Ct/cont.

- □ Time: 5.5 seconds, Distance 20 *u*m, Power: 12mW/cm^2

Photo Resist developing:

Solution: H2O:351 developer
Condition:

- □ H2O: 315 time=1 minute
- □ DI water rinse; N2 blow dry
- □ Hard Bake: 120°C for 1 min.
- □ Microscope: to check the pattern shape

Comments: little bit over developing is good for this step.

Step 9: STS etching
Equipment: STS
Condition:
Comment: for PECVD 150°C SiO2, etching rate is 304.6A/min
STS doesn't etch metal or metal oxide
Actual etching time =SiO2 thickness+2min.

□ Put acetone into ultrasonic to clean PR for 10 min
□ DI water tank; DI water rinse; N2 blow dry
□ Microscope to check the pattern

Step 10: Top electrode masks exposing. (clean-room, bay2)

Photo Resist Coating:

Equipment: CEE Photoresist Spinner(Double layers: SF 5, PR 1813)
Condition: **SF5:**
□ Pre-bake 170°C for 5 minute (to remove H2O totally), cool down for a few sec.
□ Program 9: 500RPM/500RPM (acc)-10sec/4000RPM/4000PRM (acc)-35sec.
□ Bake at 150°C for 5 minute
PR1813:
□ Program 4: Coat PR1813 at 4000RPM 30 seconds
□ Soft Bake 105°C for 1 minute

Mask exposing:

Equipment: KARLSUSS MAB6
Condition: Program: Hard-Ct/cont.
□ Time: 5.5 seconds, Distance 20 *u*m, Power: 12mW/cm^2

Photo Resist developing:

Solution: MF319 (avoid water)
Condition:
□ Clean beaker: use DI water and MF319 to clean the beaker and blow dry
□ MF319 time: 1.5 min
□ DI water rinse and N2 blow dry.
□ Microscope: to check if the pillar shape is good
□ Hard Bake: 120°C for 1 min.

Step11: Leads Deposition (Ta 50/Cu 1000/Ta 200A)
Equipment: Shamrock
Condition:
□ Pre-sputter #2-Ta #5-Cu
□ Etching 5min
□ Deposit #2 Ta 170w 50sccm 160sec (50 Å)
□ Deposit #5 Cu 386w 45sccm 640sec (1000 Å)
□ Deposit #2 Ta 180w 50sccm 600sec (200 Å)

Comments: Ta 0.001848068 A/W*s; Cu 0.0040449297 A/W*s
Step 12: lift-off. (clean-room, bay 2) Solution: Developer 1165 □ Condition: Heat set point at 70 ^{o}C for 45min+. Put 1165 into Ultrasonic for 25min+ (1165 can be heated to 60 ^{o}C first). Water tank; DI water rinse; N2 blow dry. Check with Microscopes. Comments: Before lift-off, make some stripes on the unuseful area to help lift-off. Several bathes during the heating and Ultrasonic

Bibliography

1 Sunaga, K., Tsunoda, M., Komagaki, K., Uehara, Y. & Takahashi, M. Inverse tunnel magnetoresistance in magnetic tunnel junctions with an Fe4N electrode. *Journal of Applied Physics* **102**, doi:10.1063/1.2753576 (2007).

2 Komasaki, Y., Tsunoda, M., Isogami, S. & Takahashi, M. 75% inverse magnetoresistance at room temperature in Fe4N/MgO/CoFeB magnetic tunnel junctions fabricated on Cu underlayer. *Journal of Applied Physics* **105**, doi:10.1063/1.3072827 (2009).

3 Kokado, S., Fujima, N., Harigaya, K., Shimizu, H. & Sakuma, A. Theoretical analysis of highly spin-polarized transport in the iron nitride Fe4N. *Physical Review B* **73**, doi:10.1103/PhysRevB.73.172410 (2006).

4 Jack, K. H. Vol. 208 216-224 (The Royal Society, Proceedings of the Royal Society of London Series A Mathematical and Physical Sciences, 1951).

5 Kim, T. K. & Takahashi, M. Vol. 20 492-494 (AIP, Applied Physics Letters, 1972).

6 Sugita, Y. *et al.* GIANT MAGNETIC-MOMENT AND OTHER MAGNETIC-PROPERTIES OF EPITAXIALLY GROWN FE16N2 SINGLE-CRYSTAL FILMS. *Journal of Applied Physics* **70**, 5977-5982, doi:10.1063/1.350067 (1991).

7 Wang, J. P. *et al.* Fabrication of Fe16N2 Films by Sputtering Process and Experimental Investigation of Origin of Giant Saturation Magnetization in Fe16N2. *Ieee Transactions on Magnetics* **48**, 1710-1717, doi:10.1109/tmag.2011.2170156 (2012).

8 Takahashi, H., Igarashi, M., Kaneko, A., Miyajima, H. & Sugita, Y. Perpendicular uniaxial magnetic anisotropy of Fe16N2(001) single crystal films grown by molecular beam epitaxy. *Ieee Transactions on Magnetics* **35**, 2982-2984, doi:10.1109/20.801054 (1999).

9 Ji, N. *et al.* Perpendicular magnetic anisotropy and high spin-polarization ratio in epitaxial Fe-N thin films. *Physical Review B* **84**, doi:10.1103/PhysRevB.84.245310 (2011).

10 Kardonina, N. I., Yurovskikh, A. S. & Kolpakov, A. S. TRANSFORMATIONS IN THE Fe - N SYSTEM. *Metal Science and Heat Treatment* **52**, 457-467, doi:10.1007/s11041-010-9301-y (2011).

11 Jack, K. H. Vol. 208 200-215 (Proceedings of the Royal Society of London Series A Mathematical and Physical Sciences, 1951).

12 Jack, K. H. THE SYNTHESIS AND CHARACTERIZATION OF BULK ALPHA"-FE16N2. *Journal of Alloys and Compounds* **222**, 160-166, doi:10.1016/0925-8388(94)04901-7 (1995).

13 Sun, D. C., Jiang, E. Y., Tian, M. B., Lin, C. & Zhang, X. X. Epitaxial single crystal Fe16N2 films grown by facing targets sputtering. *Journal of Applied Physics* **79**, 5440-5442, doi:10.1063/1.361843 (1996).

14 Okamoto, S., Kitakami, O. & Shimada, Y. Characterization of epitaxially grown Fe-N films by sputter beam method. *Journal of Applied Physics* **79**, 1678-1683, doi:10.1063/1.361421 (1996).

15 Ji, N. A., Allard, L. F., Lara-Curzio, E. & Wang, J. P. N site ordering effect on partially ordered Fe16N2. *Applied Physics Letters* **98**, doi:10.1063/1.3560051 (2011).

16 Slater, J. C. Electronic Structure of Alloys. *Journal of Applied Physics* **8**, doi: 10.1063/1.1710311 (1937).

17 Pauling, L. The Nature of the Interatomic Forces in Metals. *Physical Review* **54** doi: 10.1103/PhysRev.54.899 (1938).

18 Bozorth, R. M. Atomic Moments of Ferromagnetic Alloys. *Physical Review* **79** doi: 10.1103/PhysRev.79.887 (1950).

19 Uchida, S., Kawakatsu, T., Sekine, A. & Ukai, T. Magnetocrystalline anisotropy energies of Fe16N2 and Fe16C2. *Journal of Magnetism and Magnetic Materials* **310**, 1796-1798, doi:10.1016/j.jmmm.2006.10.708 (2007).

20 Seemann, K. M. *et al.* Diffusive and ballistic current spin polarization in magnetron-sputtered L1(0)-ordered epitaxial FePt. *Physical Review B* **76**, doi:10.1103/PhysRevB.76.174435 (2007).

21 Yakushiji, K. *et al.* Current-perpendicular-to-plane magnetoresistance in epitaxial Co2MnSi/Cr/Co2MnSi trilayers. *Applied Physics Letters* **88**, doi:10.1063/1.2207987 (2006).

22 Nakatani, T. M. *et al.* Co-Based Heusler Alloys for CPP-GMR Spin-Valves With Large Magnetoresistive Outputs. *Ieee Transactions on Magnetics* **48**, 1751-1757, doi:10.1109/tmag.2011.2174436 (2012).

23 Narahara, A. *et al.* Spin polarization of Fe4N thin films determined by point-contact Andreev reflection. *Applied Physics Letters* **94**, doi:10.1063/1.3140459 (2009).

24 Soulen, R. J. *et al.* Measuring the spin polarization of a metal with a superconducting point contact. *Science* **282**, 85-88, doi:10.1126/science.282.5386.85 (1998).

25 Ito, K. *et al.* Negative spin polarization at the Fermi level in Fe4N epitaxial films by spin-resolved photoelectron spectroscopy. *Journal of Applied Physics* **112**, doi:10.1063/1.4733327 (2012).

26 Tsunoda, M. *et al.* Negative Anisotropic Magnetoresistance in Fe4N Film. *Applied Physics Express* **2**, doi:10.1143/apex.2.083001 (2009).

27 Tsunoda, M. *et al.* Anomalous Anisotropic Magnetoresistance in Pseudo-Single-Crystal gamma '-Fe4N Films. *Applied Physics Express* **3**, doi:10.1143/apex.3.113003 (2010).

28 Ito, K. *et al.* Negative Anisotropic Magnetoresistance in gamma '-Fe4N Epitaxial Films on SrTiO3(001) Grown by Molecular Beam Epitaxy. *Japanese Journal of Applied Physics* **51**, doi:10.1143/jjap.51.068001 (2012).

29 Li, Z. R., Feng, X. P., Wang, X. C. & Mi, W. B. Anisotropic magnetoresistance in facing-target reactively sputtered epitaxial gamma '-Fe4N films. *Materials Research Bulletin* **65**, 175-182, doi:10.1016/j.materresbull.2015.01.053 (2015).

30 Ito, K. *et al.* Sign of the spin-polarization in cobalt-iron nitride films determined by the anisotropic magnetoresistance effect. *Journal of Applied Physics* **116**, doi:10.1063/1.4892179 (2014).

31 Baibich, M. N. *et al.* GIANT MAGNETORESISTANCE OF (001)FE/(001) CR MAGNETIC SUPERLATTICES. *Physical Review Letters* **61**, 2472-2475, doi:10.1103/PhysRevLett.61.2472 (1988).

32 Binasch, G., Grunberg, P., Saurenbach, F. & Zinn, W. ENHANCED MAGNETORESISTANCE IN LAYERED MAGNETIC-STRUCTURES WITH ANTIFERROMAGNETIC INTERLAYER EXCHANGE. *Physical Review B* **39**, 4828-4830, doi:10.1103/PhysRevB.39.4828 (1989).

33 Parkin, S. S. P. ORIGIN OF ENHANCED MAGNETORESISTANCE OF MAGNETIC MULTILAYERS - SPIN-DEPENDENT SCATTERING FROM MAGNETIC INTERFACE STATES. *Physical Review Letters* **71**, 1641-1644, doi:10.1103/PhysRevLett.71.1641 (1993).

34 Mott, N. F. The resistance and thermoelectric properties of the transition metals. *Proceedings of the Royal Society of London Series A Mathematical and Physical Sciences* **156**, 368-382 (1936).

35 Valet, T. & Fert, A. THEORY OF THE PERPENDICULAR MAGNETORESISTANCE IN MAGNETIC MULTILAYERS. *Physical Review B* **48**, 7099-7113, doi:10.1103/PhysRevB.48.7099 (1993).

36 Parkin, S. S. P., Bhadra, R. & Roche, K. P. OSCILLATORY MAGNETIC EXCHANGE COUPLING THROUGH THIN COPPER LAYERS. *Physical Review Letters* **66**, 2152-2155, doi:10.1103/PhysRevLett.66.2152 (1991).

37 Schad, R. *et al.* INTERPLAY BETWEEN INTERFACE PROPERTIES AND GIANT MAGNETORESISTANCE IN EPITAXIAL FE/CR SUPERLATTICES. *Journal of Magnetism and Magnetic Materials* **148**, 331-332, doi:10.1016/0304-8853(95)00259-6 (1995).

38 Araki, S. MAGNETISM AND TRANSPORT-PROPERTIES OF EVAPORATED CO/AG MULTILAYERS. *Journal of Applied Physics* **73**, 3910-3916, doi:10.1063/1.352879 (1993).

39 Rodmacq, B., Vaezzadeh, M., George, B. & Mangin, P. INFLUENCE OF ANNEALING ON THE MAGNETIC AND TRANSPORT-PROPERTIES OF AG/NI MULTILAYERS. *Journal of Magnetism and Magnetic Materials* **121**, 213-215, doi:10.1016/0304-8853(93)91188-d (1993).

40 Parkin, S. S. P. *et al.* OSCILLATIONS OF INTERLAYER EXCHANGE COUPLING AND GIANT MAGNETORESISTANCE IN (111) ORIENTED PERMALLOY AU MULTILAYERS. *Physical Review Letters* **72**, 3718-3721, doi:10.1103/PhysRevLett.72.3718 (1994).

41 Julliere, M. TUNNELING BETWEEN FERROMAGNETIC-FILMS. *Physics Letters A* **54**, 225-226, doi:10.1016/0375-9601(75)90174-7 (1975).

42 Miyazaki, T. & Tezuka, N. GIANT MAGNETIC TUNNELING EFFECT IN FE/AL2O3/FE JUNCTION. *Journal of Magnetism and Magnetic Materials* **139**, L231-L234, doi:10.1016/0304-8853(94)01648-8 (1995).

43 Moodera, J. S., Kinder, L. R., Wong, T. M. & Meservey, R. LARGE MAGNETORESISTANCE AT ROOM-TEMPERATURE IN FERROMAGNETIC THIN-FILM TUNNEL-JUNCTIONS. *Physical Review Letters* **74**, 3273-3276, doi:10.1103/PhysRevLett.74.3273 (1995).

44 Wang, D. X., Nordman, C., Daughton, J. M., Qian, Z. H. & Fink, J. 70% TMR at room temperature for SDT sandwich junctions with CoFeB as free and reference layers. *Ieee Transactions on Magnetics* **40**, 2269-2271, doi:10.1109/tmag.2004.830219 (2004).

45 Yuasa, S., Nagahama, T., Fukushima, A., Suzuki, Y. & Ando, K. Giant room-temperature magnetoresistance in single-crystal Fe/MgO/Fe magnetic tunnel junctions. *Nature Materials* **3**, 868-871, doi:10.1038/nmat1257 (2004).

46 Parkin, S. S. P. *et al.* Giant tunnelling magnetoresistance at room temperature with MgO (100) tunnel barriers. *Nature Materials* **3**, 862-867, doi:10.1038/nmat1256 (2004).

47 Butler, W. H., Zhang, X. G., Schulthess, T. C. & MacLaren, J. M. Spin-dependent tunneling conductance of Fe vertical bar MgO vertical bar Fe sandwiches. *Physical Review B* **63**, doi:10.1103/PhysRevB.63.054416 (2001).

48 Ikeda, S. *et al.* Tunnel magnetoresistance of 604% at 300 K by suppression of Ta diffusion in CoFeB/MgO/CoFeB pseudo-spin-valves annealed at high temperature. *Applied Physics Letters* **93**, doi:10.1063/1.2976435 (2008).

49 Slonczewski, J. C. Current-driven excitation of magnetic multilayers. *Journal of Magnetism and Magnetic Materials* **159**, L1-L7, doi:10.1016/0304-8853(96)00062-5 (1996).

50 Berger, L. Emission of spin waves by a magnetic multilayer traversed by a current. *Physical Review B* **54**, 9353-9358, doi:10.1103/PhysRevB.54.9353 (1996).

51 Slonczewski, J. C. Excitation of spin waves by an electric current. *Journal of Magnetism and Magnetic Materials* **195**, L261-L268, doi:10.1016/s0304-8853(99)00043-8 (1999).

52 Tsoi, M. *et al.* Excitation of a magnetic multilayer by an electric current. *Physical Review Letters* **80**, 4281-4284, doi:10.1103/PhysRevLett.80.4281 (1998).

53 Myers, E. B., Ralph, D. C., Katine, J. A., Louie, R. N. & Buhrman, R. A. Current-induced switching of domains in magnetic multilayer devices. *Science* **285**, 867-870, doi:10.1126/science.285.5429.867 (1999).

54 Katine, J. A. & Fullerton, E. E. Device implications of spin-transfer torques. *Journal of Magnetism and Magnetic Materials* **320**, 1217-1226, doi:10.1016/j.jmmm.2007.12.013 (2008).

55 Kawahara, T. *et al.* 2 Mb SPRAM (SPin-transfer torque RAM) with bit-by-bit bi-directional current write and parallelizing-direction current read. *Ieee Journal of Solid-State Circuits* **43**, 109-120, doi:10.1109/jssc.2007.909751 (2008).

56 Huai, Y. Spin-transfer torque MRAM (STT-MRAM): Challenges and prospects. *AAPPS BulletinAAPPS Bulletin* **18**, 33-40 (2008).

57 Silva, T. J. & Rippard, W. H. Developments in nano-oscillators based upon spin-transfer point-contact devices. *Journal of Magnetism and Magnetic Materials* **320**, 1260-1271, doi:10.1016/j.jmmm.2007.12.022 (2008).

58 Slonczewski, J. C. Currents, torques, and polarization factors in magnetic tunnel junctions. *Physical Review B* **71**, doi:10.1103/PhysRevB.71.024411 (2005).

59 Sankey, J. C. *et al.* Measurement of the spin-transfer-torque vector in magnetic tunnel junctions. *Nature Physics* **4**, 67-71, doi:10.1038/nphys783 (2008).

60 Zhang, S., Levy, P. M. & Fert, A. Mechanisms of spin-polarized current-driven magnetization switching. *Physical Review Letters* **88**, doi:10.1103/PhysRevLett.88.236601 (2002).

61 Li, Z. *et al.* Perpendicular spin torques in magnetic tunnel junctions. *Physical Review Letters* **100**, doi:10.1103/PhysRevLett.100.246602 (2008).

62 Stiles, M. D. & Zangwill, A. Anatomy of spin-transfer torque. *Physical Review B* **66**, doi:10.1103/PhysRevB.66.014407 (2002).

63 Raychowdhury, A., Somasekhar, D., Karnik, T., De, V. & Ieee. Design Space and Scalability Exploration of 1T-1STT MTJ Memory Arrays in the Presence of Variability and Disturbances. *2009 Ieee International Electron Devices Meeting*, 661-664 (2009).

64 Driskill-Smith, A. *et al.* Non-volatile Spin-Transfer Torque RAM (STT-RAM): Data, Analysis and Design Requirements for Thermal Stability. *2010 Symposium on Vlsi Technology, Digest of Technical Papers*, 51-52, doi:10.1109/vlsit.2010.5556124 (2010).

65 Lee, Y. M. *et al.* Highly Scalable STT-MRAM with MTJs of Top-pinned Structure in 1T/1MTJ Cell. *2010 Symposium on Vlsi Technology, Digest of Technical Papers*, 49-+, doi:10.1109/vlsit.2010.5556123 (2010).

66 Kawahara, T., Ito, K., Takemura, R. & Ohno, H. Spin-transfer torque RAM technology: Review and prospect. *Microelectronics Reliability* **52**, 613-627, doi:10.1016/j.microrel.2011.09.028 (2012).

67 Hosomi, M. *et al.* A novel nonvolatile memory with spin torque transfer magnetization switching: Spin-RAM. *Ieee International Electron Devices Meeting 2005, Technical Digest*, 473-476 (2005).

68 Engel, B. N. *et al.* A 4-mb toggle MRAM based on a novel bit and switching method. *Ieee Transactions on Magnetics* **41**, 132-136, doi:10.1109/tmag.2004.840847 (2005).

69 Meng, H. & Wang, J. P. Spin transfer in nanomagnetic devices with perpendicular anisotropy. *Applied Physics Letters* **88**, 3, doi:10.1063/1.2198797 (2006).

70 Mangin, S. *et al.* Current-induced magnetization reversal in nanopillars with perpendicular anisotropy. *Nature Materials* **5**, 210-215, doi:10.1038/nmat1595 (2006).

71 Seki, T., Mitani, S., Yakushiji, K. & Takanashi, K. Spin-polarized current-induced magnetization reversal in perpendicularly magnetized L1(0)-FePt layers. *Applied Physics Letters* **88**, doi:10.1063/1.2198819 (2006).

72 Mangin, S., Henry, Y., Ravelosona, D., Katine, J. A. & Fullerton, E. E. Reducing the critical current for spin-transfer switching of perpendicularly magnetized nanomagnets. *Applied Physics Letters* **94**, doi:10.1063/1.3058680 (2009).

73 Sun, J. Z. Spin-current interaction with a monodomain magnetic body: A model study. *Physical Review B* **62**, 570-578, doi:10.1103/PhysRevB.62.570 (2000).

74 Ikeda, S. *et al.* A perpendicular-anisotropy CoFeB-MgO magnetic tunnel junction. *Nature Materials* **9**, 721-724, doi:10.1038/nmat2804 (2010).

75 Sato, H. *et al.* Properties of magnetic tunnel junctions with a MgO/CoFeB/Ta/CoFeB/MgO recording structure down to junction diameter of 11 nm. *Applied Physics Letters* **105**, doi:10.1063/1.4892924 (2014).

76 Weller, D. *et al.* High K-u materials approach to 100 Gbits/in(2). *Ieee Transactions on Magnetics* **36**, 10-15, doi:10.1109/20.824418 (2000).

77 He, P. *et al.* Quadratic Scaling of Intrinsic Gilbert Damping with Spin-Orbital Coupling in L1(0) FePdPt Films: Experiments and Ab Initio Calculations. *Physical Review Letters* **110**, doi:10.1103/PhysRevLett.110.077203 (2013).

78 Isogami, S. & Owada, T. Electronic Circuit using Magnetic Tunnel Junctions with Normal and Inverse Magnetoresistive Effects. *Ieej Transactions on Electrical and Electronic Engineering* **9**, S73-S75, doi:10.1002/tee.22040 (2014).

79 in *http://www.stoner.leeds.ac.uk/Research/TutSputtering*.

80 Naoe, M., Yamanaka, S. I. & Hoshi, Y. FACING TARGETS TYPE OF SPUTTERING METHOD FOR DEPOSITION OF MAGNETIC METAL-FILMS AT LOW-TEMPERATURE AND HIGH-RATE. *Ieee Transactions on Magnetics* **16**, 646-648, doi:10.1109/tmag.1980.1060683 (1980).

81 Niimura, Y. & Naoe, M. FACING TARGETS SPUTTERING SYSTEM FOR DEPOSITING CO-CR PERPENDICULAR MAGNETIC RECORDING MEDIA. *Journal of Vacuum Science & Technology a-Vacuum Surfaces and Films* **5**, 109-110, doi:10.1116/1.574143 (1987).

82 Arnell, R. D. & Kelly, P. J. Recent advances in magnetron sputtering. *Surface & Coatings Technology* **112**, 170-176, doi:10.1016/s0257-8972(98)00749-x (1999).

83 S., L. S., H., M. R. & G., M. D. Temperature Rise during Film Deposition by rf and dc Sputtering. *Journal of Vacuum Science and Technology* **9**, 1196-1202 (1972).

84 Kools, J. C. S., Kula, W., Mauri, D. & Lin, T. Effect of finite magnetic film thickness on Neel coupling in spin valves. *Journal of Applied Physics* **85**, 4466-4468, doi:10.1063/1.370376 (1999).

85 Woods, G. T. *et al.* Analysis of point-contact Andreev reflection spectra in spin polarization measurements. *Physical Review B* **70**, doi:10.1103/PhysRevB.70.054416 (2004).

86 Blonder, G. E., Tinkham, M. & Klapwijk, T. M. TRANSITION FROM METALLIC TO TUNNELING REGIMES IN SUPERCONDUCTING MICRO-CONSTRICTIONS - EXCESS CURRENT, CHARGE IMBALANCE, AND SUPER-CURRENT CONVERSION. *Physical Review B* **25**, 4515-4532, doi:10.1103/PhysRevB.25.4515 (1982).

87 Kim, G., Sakuraba, Y., Oogane, M., Ando, Y. & Miyazaki, T. Tunneling magnetoresistance of magnetic tunnel junctions using perpendicular magnetization L1(0)-CoPt electrodes. *Applied Physics Letters* **92**, doi:10.1063/1.2913163 (2008).

88 Garcia, F., Fettar, F., Auffret, S., Rodmacq, B. & Dieny, B. Exchange-biased spin valves with perpendicular magnetic anisotropy based on (Co/Pt) multilayers. *Journal of Applied Physics* **93**, 8397-8399, doi:10.1063/1.1558096 (2003).

89 Yakushiji, K. *et al.* Ultrathin Co/Pt and Co/Pd superlattice films for MgO-based perpendicular magnetic tunnel junctions. *Applied Physics Letters* **97**, doi:10.1063/1.3524230 (2010).

90 Mizunuma, K. *et al.* MgO barrier-perpendicular magnetic tunnel junctions with CoFe/Pd multilayers and ferromagnetic insertion layers. *Applied Physics Letters* **95**, doi:10.1063/1.3265740 (2009).

91 Mizukami, S. *et al.* Gilbert damping in perpendicularly magnetized Pt/Co/Pt films investigated by all-optical pump-probe technique. *Applied Physics Letters* **96**, doi:10.1063/1.3396983 (2010).

92 Kim, J. W. *et al.* Ultrafast magnetization relaxation of L1(0)-ordered Fe50Pt50 alloy thin film. *Applied Physics Letters* **98**, doi:10.1063/1.3559845 (2011).

93 Worledge, D. C. *et al.* Spin torque switching of perpendicular Ta vertical bar CoFeB vertical bar MgO-based magnetic tunnel junctions. *Applied Physics Letters* **98**, doi:10.1063/1.3536482 (2011).

94 Aharoni, A. Demagnetizing factors for rectangular ferromagnetic prisms. *Journal of Applied Physics* **83**, 3432-3434, doi:10.1063/1.367113 (1998).

95 Hicken, R. J. *et al.* Magnetic anistropy in ultrathin epitaxial Fe/Ag(100) films with overlayers. *Physical Review B* **55**, 5898-5907, doi:10.1103/PhysRevB.55.5898 (1997).

96 Nakajima, H., Ohashi, Y. & Shiiki, K. Effect of N atom and lattice constant on electronic structures and magnetic properties of Fe16N2 calculated by band structure calculation based on local-density approximation. *Journal of Magnetism and Magnetic Materials* **167**, 259-263, doi:10.1016/s0304-8853(96)00638-5 (1997).

97 Shick, A. B. & Mryasov, O. N. Coulomb correlations and magnetic anisotropy in ordered L1(0) CoPt and FePt alloys. *Physical Review B* **67**, doi:10.1103/PhysRevB.67.172407 (2003).

98 Gajek, M. *et al.* Spin torque switching of 20 nm magnetic tunnel junctions with perpendicular anisotropy. *Applied Physics Letters* **100**, doi:10.1063/1.3694270 (2012).

99 Macia, F. *et al.* Perpendicular magnetic anisotropy in ultrathin Co vertical bar Ni multilayer films studied with ferromagnetic resonance and magnetic x-ray microspectroscopy. *Journal of Magnetism and Magnetic Materials* **324**, 3629-3632, doi:10.1016/j.jmmm.2012.03.063 (2012).

100 Kalarickal, S. S. *et al.* Ferromagnetic resonance linewidth in metallic thin films: Comparison of measurement methods. *Journal of Applied Physics* **99**, doi:10.1063/1.2197087 (2006).

101 Dou, J., Pechan, M. J., Shipton, E., Eibagi, N. & Fullerton, E. E. Tunable resonant properties of perpendicular anisotropy Co/Pd /Fe/ Co/Pd multilayers. *Journal of Applied Physics* **113**, doi:10.1063/1.4801641 (2013).

102 Heinrich, B., Cochran, J. F. & Hasegawa, R. FMR LINEBROADENING IN METALS DUE TO 2-MAGNON SCATTERING. *Journal of Applied Physics* **57**, 3690-3692, doi:10.1063/1.334991 (1985).

103 Farle, M., MirwaldSchulz, B., Anisimov, A. N., Platow, W. & Baberschke, K. Higher-order magnetic anisotropies and the nature of the spin-reorientation transition in face-centered-tetragonal Ni(001)/Cu(001). *Physical Review B* **55**, 3708-3715, doi:10.1103/PhysRevB.55.3708 (1997).

104 Chen, Y. S., Cheng, C. W., Chern, G., Wu, W. F. & Lin, J. G. Ferromagnetic resonance probed annealing effects on magnetic anisotropy of perpendicular CoFeB/MgO bilayer. *Journal of Applied Physics* **111**, doi:10.1063/1.3670042 (2012).

105 Zhang, X. W., Yang, M. Y., Jiang, Y. F., Allard, L. F. & Wang, J. P. Thermal stability of partially ordered Fe16N2 film on non-magnetic Ag under layer. *Journal of Applied Physics* **115**, doi:10.1063/1.4869065 (2014).

106 Wang, H. Y. & Jiang, E. Y. Enhancement of the thermal stability of Fe16N2 by Ti addition. *Journal of Physics-Condensed Matter* **9**, 2739-2743, doi:10.1088/0953-8984/9/13/011 (1997).

107 Xiang, H., Shi, F. Y., Rzchowski, M. S., Voyles, P. M. & Chang, Y. A. Epitaxial growth and thermal stability of Fe4N film on TiN buffered Si(001) substrate. *Journal of Applied Physics* **109**, doi:10.1063/1.3556919 (2011).

108 Mi, W. B., Guo, Z. B., Feng, X. P. & Bai, H. L. Reactively sputtered epitaxial gamma '-Fe4N films: Surface morphology, microstructure, magnetic and electrical transport properties. *Acta Materialia* **61**, 6387-6395, doi:10.1016/j.actamat.2013.07.016 (2013).

109 Farrow, R. F. C. *et al.* MnxPt1-x: A new exchange bias material for Permalloy. *Journal of Applied Physics* **81**, 4986-4988, doi:10.1063/1.364961 (1997).

110 Na, Y. Y., Wang, C., Xiang, J. Z., Ji, N. A. & Wang, J. P. Investigation of gamma '-Fe4N thin films deposited on Si(100) and GaAs (100) substrates by facing target magnetron sputtering. *Journal of Crystal Growth* **426**, 117-122, doi:10.1016/j.jcrysgro.2015.05.028 (2015).

111 Isogami, S., Tsunoda, M., Oogane, M., Sakuma, A. & Takahasi, M. Enhancement of Spin Pumping Efficiency in Fe4N/Pt Bilayer Films. *Applied Physics Express* **6**, doi:10.7567/apex.6.063004 (2013).

112 Isogami, S., Tsunoda, M., Oogane, M., Sakuma, A. & Takahashi, M. The Enhancement of Magnetic Damping in Fe4N Films with Increasing Thickness. *Japanese Journal of Applied Physics* **52**, doi:10.7567/jjap.52.073001 (2013).

113 Barati, E., Cinal, M., Edwards, D. M. & Umerski, A. Gilbert damping in magnetic layered systems. *Physical Review B* **90**, doi:10.1103/PhysRevB.90.014420 (2014).

114 Jamali, M., Klemm, A. & Wang, J. P. Precessional magnetization induced spin current from CoFeB into Ta. *Applied Physics Letters* **103**, doi:10.1063/1.4853195 (2013).

Publication List

1. **Xuan Li**, Meiyin Yang, Mahdi Jamali, Fengyuan Shi, Shishou Kang, Yanfeng Jiang, Xiaowei Zhang, P. M. Voyles, S. Okatov, S. Faleev, Guanghua Yu, O. N. Mryasov, and Jian-Ping Wang, "Heavy-metal free, Low damping and Non-interface Perpendicular magnetoresistance device for future spintronic applications", Under review by Physical Review Applied.

2. **Xuan Li**, M. S. Osofsky, Kevin L. Jensen, Hongshi Li, and Jian-Ping Wang, "Deposition and spin polarization study of Fe_4N thin films with (111) orientation", AIP Advances **7**, 095001 (2017); (Editor's pick; Highlighted on AIP Scilight, Aug. 28th, 2017)

3. **Xuan Li**, Hongshi Li, Mahdi Jamali, and Jian-Ping Wang, "Damping constant measurement and inverse giant magnetoresistance in spintronic devices with Fe_4N", AIP Advances 7, 125303 (2017); (Featured; Highlighted on AIP Scilight, Dec. 4th, 2017).

4. Hongshi Li, **Xuan Li**, Dongrin Kim, Gejian Zhao, Delin Zhang, Zhitao Diao, Tingyong Chen, and Jian-Ping Wang, "81.3% Spin Polarization Ratio in Fe_4N Thin Film Determined by Point-Contact Andreev Reflection", Under review by Applied Physics Letters.

5. Nian Ji, M. S. Osofsky, Valeria Lauter, Lawrence F. Allard, **Xuan Li**, Kevin L. Jensen, Hailemariam Ambaye, Edgar Lara-Curzio, and Jian-Ping Wang, "Perpendicular magnetic anisotropy and high spin-polarization ratio in epitaxial Fe-N thin films", Phys. Rev. B **84**, 245310 (2011)

Conference Presentations

1. **Xuan Li**, Meiyin Yang, Mahdi Jamali and Jian-Ping Wang, "Magnetoresistance Device with Heavy-Metal Free, Low Damping and Non-Interface Perpendicular Magnetic Anisotropy", No. 28.4, SRC Techcon 2014.

2. **Xuan Li**, Hongshi Li, Mahdi Jamali and Jian-Ping Wang, "Deposition and damping constant measurement of Fe4N (001) thin film on Ag underlayer", EP-14, the 59th MMM Conference 2014.

3. **Xuan Li**, M. S. Osofsky, Kevin L. Jensen, and Jian-Ping Wang, "Spin polarization ratio and exchange bias properties of (111) Fe4N thin films", BW-10, the 56th MMM Conference 2011.